

1 Targeting tumour-intrinsic neural vulnerabilities of 2 glioblastoma

3 Sohyon Lee^{1*}, Tobias Weiss^{2*}, Marcel Bühler², Julien Mena¹, Zuzanna Lottenbach¹, Rebekka
4 Wegmann¹, Michel Bihl³, Bartłomiej Augustynek⁴, Sven Baumann⁴, Sandra Goetze⁵⁻⁷, Audrey van
5 Drogen⁵⁻⁷, Flavio Vasella⁸, Elisabeth J. Rushing⁹, Bernd Wollscheid⁵⁻⁷, Matthias A. Hediger⁴, Michael
6 Weller², Berend Snijder^{1,✉}

7 ¹ Institute of Molecular Systems Biology, Department of Biology, ETH Zurich, Zurich, Switzerland.

8 ² Department of Neurology, Clinical Neuroscience Center, University Hospital Zurich and University of Zurich, Zurich,
9 Switzerland.

10 ³ Institute of Pathology, University Hospital Zurich, Zurich, Switzerland

11 ⁴ Membrane Transport Discovery Lab, Department of Nephrology and Hypertension and Department of Biomedical
12 Research, Inselspital, University of Bern, Bern, Switzerland.

13 ⁵ Institute of Translational Medicine (ITM), Department of Health Sciences and Technology, ETH Zurich, Zurich, Switzerland.

14 ⁶ Swiss Institute of Bioinformatics, Lausanne, Switzerland.

15 ⁷ ETH PHRT Swiss Multi-Omics Center (SMOC), Switzerland.

16 ⁸ Department of Neurosurgery, Clinical Neuroscience Center, University Hospital and University of Zurich, Zurich,
17 Switzerland

18 ⁹ Department of Neuropathology, University Hospital Zurich and University of Zurich, Zurich, Switzerland.

19 * Shared-first authorship.

20 ✉ Correspondence to bsnijder@ethz.ch

21 Abstract

22 Glioblastoma is the most common yet deadliest primary brain cancer¹. The neural behavior of
23 glioblastoma, including the formation of synaptic circuitry and tumor microtubes, is increasingly
24 understood to be pivotal for disease manifestation²⁻⁸. Nonetheless, the few approved treatments for
25 glioblastoma target its oncological nature, while its neural vulnerabilities remain incompletely mapped
26 and clinically unexploited. Here, we systematically survey the neural molecular dependencies and
27 cellular heterogeneity across glioblastoma patients and diverse model systems. In 27 patient tumour
28 samples taken directly after surgery, we identify a spectrum of cancer cell morphologies indicative of
29 poor prognosis and discover a set of repurposable neuroactive drugs with consistent anti-glioblastoma
30 efficacy. Glioblastoma cells exhibit functional dependencies on highly expressed neuroactive drug
31 targets, while interpretable molecular machine learning (COSTAR) reveals their downstream
32 convergence on AP-1-driven tumour suppression. This drug-target connectivity signature is confirmed
33 by highly accurate *in silico* drug screening on >1 million compounds using COSTAR, as well as by multi-
34 omic profiling of drug-treated glioblastoma cells. Thus, Ca²⁺-driven AP-1 pathway induction represents
35 a tumour-intrinsic vulnerability at the intersection of oncogenesis and neural activity-dependent
36 signaling. Opportunities for clinical translation of this neural vulnerability are epitomized by the
37 antidepressant Vortioxetine synergizing with current standard of care treatments *in vivo*. Together,
38 the results presented here provide a mechanistic foundation and conceptual framework for the
39 treatment of glioblastoma based on its neural origins.

40 Introduction

41 Glioblastoma is a deadly brain cancer with limited treatment options, shaped by heterogeneous
42 developmental programs, genetic drivers, and tumor microenvironments^{9–13}. Despite an increasing
43 understanding of this heterogeneity, the alkylating agent Temozolomide (TMZ), which prolongs
44 median survival from 12 to 15 months, remains the only first-line drug approved for glioblastoma^{14–}
45¹⁶. Targeted therapies have been largely unsuccessful, in part due to the blood-brain barrier (BBB)
46 limiting tumor accessibility, the presence of treatment-resistant glioblastoma stem cells (GSCs), and
47 the lack of clinically predictive models^{17–22}. Systemically addressing these therapeutic roadblocks is an
48 urgent clinical need.

49 An emerging paradigm is to consider glioblastoma in the context of the nervous system. Single-cell
50 RNA sequencing (scRNA-Seq) and lineage tracing studies of glioblastoma have identified stemness
51 signatures resembling neural development^{7,11,12,23–28}. At the brain-tumor interface, synaptic
52 integration of cancer cells into neural circuits regulates tumor growth^{5,6}. Within the tumor, the
53 extension of microtubules akin to neuronal protrusions promotes the formation of treatment-resistant
54 invasive networks^{2,4,8}. Furthermore, modulating specific neurotransmitter or other secretory
55 pathways in the tumor microenvironment impairs glioblastoma metabolism and survival^{3,29–31}. Such
56 neural aspects of glioblastoma offer new clinically-targetable vulnerabilities that could be exploited by
57 repurposing approved “neuroactive” drugs (NADs). Neuroactive drugs can cross the BBB and are
58 routinely prescribed for indications such as psychiatric or neurodegenerative diseases. Yet, as
59 neuroactive drugs are originally developed to modulate the nervous system, their anti-cancer activity
60 in glioblastoma patients is largely unknown.

61 Several key questions arise. First, how does neural intratumor heterogeneity across glioblastoma
62 patients relate to disease course and response to therapy? Second, are there tumor-intrinsic neural
63 vulnerabilities that are therapeutically targetable? Third, if so, which molecular dependencies and
64 associated pathways are involved?

65 Here, we find morphological and neural stemness features across glioblastomas that relate to disease
66 prognosis and drug response. Using pharmacoscopy (PCY), an *ex vivo* imaging platform^{32–34} that
67 captures patient and tumor complexity, we screen repurposable neuroactive drugs and identify a set
68 with potent anti-glioblastoma activity. Top neuroactive drugs work consistently across patients and
69 particularly target GSCs with neural morphologies associated with invasion and poor prognosis. These
70 top drugs are validated across multiple glioblastoma model systems including patient-derived cultures
71 and orthotopic xenograft mouse models. Integration of anti-glioblastoma response with multiplexed
72 RNA-Seq, reverse genetic screening, and machine learning of drug-target networks reveals
73 convergence of neuroactive drugs with anti-glioblastoma activity on AP-1 transcription factor and BTG
74 tumor suppressor gene families. Using this drug-target connectivity signature, we predict and validate
75 new candidate drugs across >1 million compounds *in silico*. The antidepressant Vortioxetine is the top
76 PCY-hit and inducer of the AP-1/BTG signature, synergizing with both first- and second-line
77 glioblastoma therapies *in vivo*. Our study identifies clinically-actionable neuroactive drugs for the
78 treatment of glioblastoma converging on a gene regulatory network involved in cell proliferation and
79 neural activity.

Results

Glioblastoma stem cell morphologies prognostic of poor outcome

Glioblastoma cells adopt unique cellular morphologies and stemness properties to integrate and survive in the brain^{2,4,8,12,35}. To comprehensively profile morphological and molecular heterogeneity within and between glioblastoma patients, we performed high-content confocal imaging of freshly dissociated surgical samples across 27 patients (prospective cohort; Fig. 1a,b and Extended Data Fig. 1a). In parallel, for all patients, somatic genetic alterations were determined by targeted next-generation sequencing (NGS) and scRNA-Seq was performed for a subset of patients (n=4 patients, Fig. 1a, Extended Data Fig. 1a-f and Supplementary Table 1,2). Glioblastoma cells were identified and placed along a neural stemness gradient by scRNA-Seq and immunofluorescence against the neural progenitor marker Nestin and the mature astrocytic marker S100B (Fig. 1c,d and Extended Data Fig. 1c-e). Immune cells present in the tumor microenvironment (TME) were identified by the pan-immune marker CD45 and T cell marker CD3. Marker negative cells included additional TME cell types observed by scRNA-Seq or tumor cells with low protein levels of Nestin and S100B (Fig. 1c,d and Extended Data Fig. 1e,f). Patient samples were highly heterogeneous in composition, with Nestin⁺ or S100B⁺ glioblastoma cells ranging from 4-39%, CD45⁺ immune cells from 1-82%, and all marker negative cells 13-84% (Fig. 1d).

Nestin⁺ cells are a proliferative GSC subpopulation at the apex of the neural stemness gradient shown to sustain long-term tumor growth^{17,19,36-38}. Upon visual inspection of Nestin⁺ GSCs, we observed cellular “morphotypes” distinguishable by the presence of tumor microtubules (TMs) and other morphological features such as cell size and shape (Fig. 1b,e-g). Using deep learning on 51,028 manually curated single-cell image crops across all patient samples, we trained a convolutional neural network (CNN) to classify Nestin⁺ cells into four main morphotypes (M1-M4) with 84.3% accuracy (Fig. 1d,f and Extended Data Fig.2a,b). Single-cell feature maps extracted from the CNN and nuclei segmentation revealed a continuum of M1-M3 morphotypes and a distinct cluster of small M4 cells (Fig. 1f,g). M1 (PTM; polygonal TM-containing) and M2 (ETM; elongated TM-containing) GSC morphotypes had varying distributions of TMs per cell (Fig. 1e), while TM-absent M3 (RB; round big) and M4 (RS; round small) morphotypes were characterized by their roundness yet differed in cell size (Fig. 1f,g and Extended Data Fig. 2c). Nestin expression was higher in the more complex M1-M3 morphotypes (Fig. 1g).

GSC morphotype composition varied dramatically across patients (M1: 1.3-31.4%; M2: 0.5-43.4%; M3: 1.9-38.6%; M4: 14-95.1%, Fig. 1d). Abundance of morphotypes was associated with cell proliferation, where the fraction of complex morphologies (M1-M3) was correlated with Ki67 levels measured by pathology in patient-matched tissue sections (Fig. 1h, top left). Furthermore, patient stratification based on morphotype composition was significantly associated with progression-free survival (PFS): lower baseline abundance of complex morphologies (M1, M3) and higher abundance of the small M4 morphotype was associated with better clinical outcome (n=17 patients with annotated PFS, Fig. 1h and Extended Data Fig. 2d). We did not observe a survival difference based solely on Ki67 levels, sex, or the abundance of marker-defined populations (Extended Data Fig. 2e); implying a unique prognostic contribution of the aggressive GSC morphologies. While *MGMT* promoter methylation status, a prognostic factor associated with response to alkylating agents, stratified patient survival, complex morphotype (M1-M3) abundance was independent of *MGMT* status (Fisher’s test, $P=0.19$, Extended

122 Data Fig. 2e). Thus, while tumor microtubules have been associated with glioblastoma grade ², we now
123 show that GSCs adopt a spectrum of complex morphologies prognostic of poor clinical response also
124 among glioblastomas.

125 **Clinical concordance of *ex vivo* single-cell drug profiling**

126 The DNA-alkylating chemotherapy TMZ remains the only approved first-line drug for glioblastoma. To
127 determine if the chemosensitivity of highly heterogeneous patient samples relates to clinical response,
128 we tested first- and second-line glioblastoma chemotherapies (n=3 drugs) in two independent
129 glioblastoma cohorts: our main prospective cohort (n=27 patients) and a bio-banked retrospective
130 cohort (n=18 patients, Fig.1a,i-l, Extended Data Fig. 3a, and Supplementary Table 1). We utilized
131 pharmacoscopy (PCY), a clinically predictive *ex vivo* image-based screening platform developed in-
132 house ^{32–34,39–42}. Pharmacoscopy measures the drug-induced relative reduction of any marker- or
133 morphology-defined cell population in heterogeneous patient samples. Here, a positive PCY score
134 indicates a reduction of Nestin+ or S100B+ glioblastoma cells relative to non-malignant TME cells, while
135 a negative score indicates higher toxicity in the TME (Fig. 1i). Glioblastoma patients exhibited a wide
136 spectrum of *ex vivo* responses to the first-line therapy Temozolomide (50–500 μ M; 2 days of incubation;
137 Fig. 1j). We performed survival analysis on 16 of the 27 prospectively tested patients, limited to those
138 patients with primary tumors and having received first-line TMZ treatment with evaluable PFS (n=16
139 patients, with n=3 ongoing responses). Prospectively stratifying patients by their *ex vivo* TMZ sensitivity
140 suggested improved PFS for *ex vivo* responders, reaching significance at 100 μ M TMZ (p = 0.041; Fig. 1k
141 and Extended Data Fig. 3b). We repeated this PCY-based response stratification analysis in a
142 retrospective validation cohort with documented PFS and OS (n=18 patients). Here, *ex vivo* TMZ
143 responders also had significantly longer PFS and OS, evidenced across all four tested TMZ
144 concentrations (Fig. 1l). In contrast, TMZ sensitivity of CD45+ immune cells or of GSC morphotypes was
145 not associated with clinical response. *Ex vivo* TMZ response further related to *MGMT* status, as we
146 observed higher sensitivities to low dose TMZ (50 μ M) in patient tumors with methylated *MGMT*
147 promoter (Extended Data Fig. 3c). Taken together, this suggests that *ex vivo* TMZ response of
148 glioblastoma cells, as well as the baseline abundance of GSC morphotypes at diagnosis, are both novel
149 prognostic factors for first-line response. The concurrence of pharmacoscopy with clinical response
150 establishes the utility of image-based drug screening in patient material for the discovery of new
151 glioblastoma therapies.

152 **Therapeutically targeting neural tumor heterogeneity**

153 The question arises whether it is possible to pharmacologically target the heterogeneous spectrum of
154 malignant cells, both in terms of their molecular composition and morphological nature. To find
155 repurposable drug candidates that target glioblastoma cells and aggressive GSC morphologies, we
156 tested both neuroactive and oncology drug libraries across the prospective glioblastoma cohort (Fig.
157 2a-c, Extended Data Fig. 3d,e, and Supplementary Table 3). The neuroactive drug (NAD) library
158 consisted of drugs approved for neurological diseases such as depression, epilepsy, and Alzheimer's
159 disease (n=67 drugs; 20 μ M). The oncology drug (ONCD) library included therapies approved for solid
160 tumor indications such as cyclin-dependent kinase (CDK) and receptor tyrosine kinase (RTK) inhibitors
161 (n=65 drugs; 1 and 10 μ M). We screened the NAD library across the whole prospective cohort (n=27
162 patients) and additionally tested the ONCD library in a subset of patients when enough surgical
163 material was available (n=12 patients). As primary PCY-readouts, we measured on-target reduction of

164 Nestin+ or S100B+ cells and GSC morphotype composition changes across patients (Fig. 2b,c and
165 Extended Data Fig. 3d). Drug responses for other TME populations including immune cells and marker
166 negative cells were also measured (Extended Data Fig. 3e).

167 Despite limited success of targeted cancer therapies for glioblastoma, opportunities for molecularly-
168 guided precision oncology and drug repurposing remain. Among ONCDs, the top mean ranking PCY-hit
169 across patients was Elesclomol, a BBB-penetrant mitochondrial oxidative stress-inducer (Fig. 2c and
170 Extended Data Fig. 3d)^{43,44}. Elesclomol represents a compelling therapeutic candidate amidst growing
171 evidence highlighting the importance of mitochondrial dynamics in brain tumorigenesis⁴⁵⁻⁴⁷. Among
172 all tested drugs, Elesclomol response showed the strongest positive correlation with age, suggesting a
173 potential link with mitochondrial aging and benefit for elderly patients (Fig. 2d). Ranked 2nd and 6th
174 among the ONCDs were the two structurally-related multi-tyrosine kinase inhibitors, Sorafenib and
175 Regorafenib. Regorafenib has recently been proposed to mediate a survival benefit over Lomustine in
176 a randomized phase II clinical trial for patients with recurrent glioblastoma (Fig. 2c and Extended Data
177 Fig. 3d)⁴⁸. Across our cohort, Regorafenib showed one of the strongest positive correlations to Ki67
178 levels, which could be leveraged to inform future clinical trials (Fig. 2e). Conversely, both of the tested
179 mTOR inhibitors Temozolomide and Everolimus showed no *ex vivo* efficacy, in line with negative results
180 from randomized clinical trials (Extended Data Fig. 3d)⁴⁹⁻⁵¹. As a tumor's mutational profile often
181 influences drug response, we examined associations between ONCD responses and genetic alterations
182 measured by targeted NGS across the cohort. The strongest pharmacogenetic association for ONCDs
183 was the markedly increased *ex vivo* sensitivity of patients carrying p53 mutations to the CDK4/6
184 inhibitor Abemaciclib (Fig. 2f and Extended Data Fig. 3f-g). Our exploratory analysis of oncological
185 drugs approved for other indications thereby identifies unevaluated treatment opportunities in
186 glioblastoma.

187 Neuroactive drugs, in contrast, are developed to cross the blood-brain barrier and act upon the
188 nervous system. Among NADs, we identified 15 of 67 drugs (22%) with consistent anti-glioblastoma
189 activity across patients (top NADs; PCY-hits; mean PCY score > 0.03). Top NADs effectively reduced
190 fractions of aggressive GSC morphologies in patient samples (M1-M3), and showed activity across
191 patient-derived cultures (PDCs, n=3 lines) and established glioblastoma cell lines (n=4 lines, Fig. 2a,b).
192 Dose-response relationships were further confirmed in glioblastoma cell lines for selected top NADs
193 (n=9 drugs, Extended Data Fig. 4a-d). The top mean ranking PCY-hit was Vortioxetine, a safe and novel
194 class of antidepressant with previously unknown anti-glioblastoma activity (Fig. 2b,c). Strikingly,
195 Vortioxetine was more potent in patient samples with higher baseline abundance of aggressive GSC
196 morphologies (Fig. 2g). Vortioxetine was also the most consistently effective drug across all tested
197 glioblastoma model systems, with *ex vivo* efficacy surpassing Regorafenib (Fig. 2c). Other clinically
198 attractive NADs included Paroxetine and Fluoxetine, both antidepressants of the selective serotonin
199 reuptake inhibitor (SSRI) class, and Brexpiprazole, an atypical antipsychotic used for the treatment of
200 schizophrenia. Brexpiprazole *ex vivo* response was related to sex, where men responded better than
201 women (Fig. 2h and Extended Data Fig. 3g). Not all top NADs were clinically suitable considering the
202 historically reported side-effects of the cannabinoid receptor blocker Rimonabant and the
203 antipsychotic Zolpidem, yet these could still inform future drug design studies.

204 Notable exceptions to the pan-patient and model consistency of top NADs were Apomorphine,
205 Olanzapine, and Sertindole (Fig. 2b). Apomorphine showed high TME toxicity in a subset of patient
206 samples and diminished efficacy in PDCs and glioblastoma-initiating spheroid cell lines (ZH-161, ZH-
207 562); Olanzapine showed diminished activity against aggressive GSC morphologies, PDCs, and cell lines;

208 and Sertindole response was highly variable among patients, despite its potency in glioblastoma
209 models. Patient variability in *ex vivo* Sertindole response was related to the loss of FGFR2 (copy number
210 variation; CNV loss), representing the most significant pharmacogenetic NAD association (Fig. 2i and
211 Extended Data Fig. 3f).

212 Here, by comprehensively screening across heterogeneous patients and model systems, we identify a
213 set of repurposable neuroactive drugs that effectively target the neural heterogeneity of glioblastoma
214 cells. The consistency of the anti-glioblastoma efficacy of these neuroactive drugs in diverse model
215 systems even in the absence of the TME suggests that they are targeting tumor-intrinsic vulnerabilities.

216 **Divergent functional dependencies on neuroactive drug targets**

217 The multitude of neuroactive drugs with anti-glioblastoma activity was unexpected, prompting the
218 question as to whether there could be shared underlying mechanisms. Top NADs represented diverse
219 drug classes without significant enrichment, indicating that canonical mode-of-action did not explain
220 drug efficacy (Fig. 3a). This is in line with a previous screen of neurochemical compounds in patient-
221 derived stem cell lines, which found various neurochemical classes represented among their hits²⁹.
222 Among our tested serotonin and dopamine pathway modulators, for example, only 4 out of 11
223 antidepressants (36%) and 6 out of 16 antipsychotics (38%) exhibited anti-glioblastoma activity in
224 primary patient samples on average (Extended Data Fig. 4e). Such drug classifications, however,
225 simplify the polypharmacological drug-target profiles of neuroactive drugs. The majority of NADs act
226 on multiple primary target genes (PTGs). These include ion channels, GPCRs, and enzymes that
227 modulate neurotransmission in the central nervous system, whose expression remains a largely
228 unexplored dimension of glioblastoma heterogeneity. Dependency on neuroactive PTGs with high
229 lineage specificity and consistent expression across patients could explain the activity of top NADs.

230 We first set out to determine the expression of NAD PTGs by scRNA-Seq. We integrated scRNA-Seq
231 data from our glioblastoma patient cohort (n=4 patients) with two published data sets (*Nefitel et al.*, n=9
232 patients; *Yu et al.*, n=9 patients, Fig. 3b,c and Extended Data Fig. 5a,b)^{12,28}. Collectively, we profiled 22
233 glioblastoma patient single-cell transcriptomes across 25,510 cells for their expression of PTGs with
234 biochemical NAD-interactions reported in the Drug Targets Commons database (DTC)⁵². Among these
235 PTGs, certain classes of ion channels and GPCRs were enriched in neural lineage cells (e.g. potassium,
236 glutamate, and cannabinoid), while other classes showed broader expression patterns (e.g. calcium,
237 adrenaline, Extended Data Fig. 5a). To quantify PTG expression across cell types and patients, we
238 defined neural- and patient-specificity scores (NS and PS; Fig. 3b, Extended Data Fig. 5b and Methods).
239 For detected genes, a higher NS indicates relative enrichment in glioblastoma cells (range -1 to 1) and
240 a higher PS (range 0 to 1) indicates more patient-specific expression, while both scores will be close to
241 zero for low-abundance genes. We first benchmarked the neural- and patient-specificity scores against
242 the whole transcriptome for each dataset, including key glioblastoma (Nestin, S100B, CD133, SOX2)
243 and immune marker genes (CD45, CD3, CD14) that were on expected opposites of the NS spectrum
244 (Extended Data Fig. 5b and Supplementary Table 4). Among PTGs, ion channels and receptors with high
245 neural-specificity included the calcium signaling modulator SIGMAR1, glutamatergic AMPA receptor
246 subunit GRIA2, and cannabinoid receptor CNR1 (Fig. 3c). Patient-specificity for neurological receptors
247 SIGMAR1 and CNR1 were on average 1.7 to 3-fold lower than for oncogenic RTKs EGFR and PDGFRA,
248 despite similar detection levels. Thus, we find abundant and consistent pan-patient expression of
249 neuroactive drug targets on glioblastoma cells, confirmed across independent cohorts.

250 We next tested genetic dependencies on these NAD PTGs by performing an siRNA screen in LN-229
251 glioblastoma cells (n=59 genes, Fig. 3d and Extended Data Fig. 5c,d). LN-229 cells were confirmed to
252 have patient-comparable PTG expression as well as neuroactive drug responses (Fig. 2b, Fig. 3d and
253 Extended Data Fig. 5d). A significant decrease in cell viability was observed upon knockdown of 9 PTGs,
254 including ADRA2B, SIGMAR1, DRD1, HTR3A, and MC3R (Fig. 3d and Extended Data Fig. 5c,d). Of these,
255 ADRA2B and MC3R expression levels stratified glioblastoma patient survival in The Cancer Genome
256 Atlas (TCGA) cohort (Extended Data Fig. 5e). However, these primary drug targets representing genetic
257 dependencies were all annotated in DTC to predominantly interact with drugs that showed no activity
258 by pharmacoscopy. Inversely, top neuroactive drugs had many annotated targets not representing
259 genetic dependencies. For example, based on DTC, only 6 of the 17 NADs interacting with ADRA2B
260 were PCY-hits, and only 1 out of 11 NADs interacting with HTR3A was a PCY-hit (Fig. 3e). Therefore,
261 while presenting novel neural vulnerabilities, no PTG dependency uniquely explained the majority of
262 our top neuroactive drugs.

263 **Anti-glioblastoma activity explained by drug-target convergence**

264 Despite their chemical and primary target diversity, our top NADs may still converge upon common
265 downstream signaling pathways. To test this, we developed an interpretable machine learning
266 approach called COSTAR: *convergence of secondary drug targets analyzed by regularized regression*.
267 COSTAR is designed to identify the minimal drug-target connectivity signature predictive of efficacy.

268 We expanded the drug-target search space to include PTGs with any bioactivity annotated by DTC,
269 termed extended PTGs (ePTGs). Secondary target genes (STGs) downstream of ePTGs were
270 subsequently mapped by high-confidence protein-protein interactions annotated in the STRING
271 database (Fig. 3f). This resulted in a drug-target connectivity map, or “COSTAR constellation”, of all
272 DTC-annotated drugs in our NAD and ONCD libraries (n=127 of 132 tested drugs) with 975 extended
273 primary targets, 10,573 secondary targets, and 114,517 network edges (Fig. 3f). Using logistic LASSO
274 regression, we trained a multi-linear model that identifies the minimal set of STGs that maximally
275 discriminates PCY-hit drugs (n=30; top-15 drugs from both NADs and ONCDs) from PCY-negative drugs
276 (n=97; all other tested drugs) in a cross-validation setting (Fig. 3f,g Extended Data Fig. 6a, and
277 Methods). Thereby, COSTAR converged upon the most simplistic connectivity signature that was
278 predictive of anti-glioblastoma drug efficacy (Fig. 3h and Extended Data Fig. 6a,b). Encouragingly,
279 COSTAR identified a signature that classified the 127 drugs in our training data with 92.1% accuracy,
280 correctly predicting 20/30 PCY-hits and 96/97 negative drugs (Fig. 3g).

281 The COSTAR connectivity signature predominantly linked PCY-hit NADs to the secondary target BTG2
282 through JUN/TP53 ePTGs (Fig. 3h and Extended Data Fig. 6b). BTG2 and TP53 are both tumor
283 suppressors that control cell cycle and differentiation, while JUN is a member of the AP-1 transcription
284 factor (TF) family that regulates gene expression in response to stimuli such as neural activity^{53,54}.
285 Conversely, the majority of PCY-hit ONCDs were connected to the secondary target AP1S2, a protein
286 involved in clathrin assembly, through the cyclin G-associated kinase GAK (Fig. 3h and Extended Data
287 Fig. 6b). A subset of PCY-hit ONCDs were also linked to BTG2 through cyclins CCND1 and CCNH, while
288 a subset of PCY-hit NADs were linked to AP1S2 through RAB9A, a member of the RAS oncogene family
289 (Fig. 3h). Taken together, this reveals pathway convergence on AP-1 transcription factors and cell cycle
290 regulation as a unique signature predictive of anti-glioblastoma activity of neuroactive drugs.

291 COSTAR can be utilized as a powerful *in silico* drug screening tool. It can match the drug-target profile
292 of any annotated compound with the identified connectivity signature to predict its hit probability
293 (COSTAR score). To experimentally validate the COSTAR signature and find additional neuroactive drug
294 candidates with anti-glioblastoma activity, we computationally screened across 1,120,823 DTC-
295 annotated compounds and selected 48 previously untested repurposable and BBB-permeable drugs
296 among the top and bottom scoring compounds (COSTAR-hits and COSTAR-negs resp.; Fig. 3i-k). All
297 predicted COSTAR-hits (n=23 drugs) were linked to the secondary target BTG2. Conversely, none of
298 the COSTAR-negs (n=25 drugs) had annotated connections to BTG2 (Extended Data Fig. 6c). To validate
299 these COSTAR predictions, we tested all 48 drugs across four GBM patient samples *ex vivo* (P030, P032,
300 P034, P042), and observed excellent agreement between COSTAR predictions and experimental results
301 (mean AUC=0.94, Fig. 3j,k). The new COSTAR-hits again represented diverse drug classes, including the
302 antipsychotic Trifluoperazine, antiparkinsonian Ethopropazine, antidepressant Sertraline, and
303 bronchodilator Salmeterol (Fig. 3j). These results validate our interpretable molecular machine
304 learning approach for *in silico* drug discovery, and confirm AP-1 and cell cycle pathway convergence as
305 a predictive signature of neuroactive drugs with *ex vivo* anti-glioblastoma activity.

306 **From neural activity-dependent signaling to tumor suppression**

307 Convergent drug targets of top NADs represent transcription factors and tumor suppressors,
308 suggesting common gene regulatory networks (GRNs) underlying the anti-glioblastoma activity of
309 NADs. To determine transcriptional changes upon drug perturbation, we profiled 20 drug responses
310 across two time-points (6 and 22 hours) in LN-229 cells by DRUG-Seq^{55,56}. These 20 drugs were selected
311 to include PCY-hit NADs spanning diverse drug classes (n=11), PCY-hit ONCDs (n=7), PCY-negative NADs
312 (n=2), and a DMSO control (Fig. 4a-d, Extended Data Fig. 7a,b, and Supplementary Table 3). Differential
313 gene expression analysis upon PCY-hit NAD treatment compared to the PCY-negative NADs and DMSO
314 control revealed a strong transcriptional drug response, with upregulated genes enriched in 'MAPK
315 signaling' and 'transcriptional misregulation of cancer' pathways at both time-points (Fig. 4b and
316 Extended Data Fig. 7c,d).

317 In remarkable alignment with COSTAR, AP-1 and BTG family member genes were strongly upregulated
318 in response to the PCY-hit NADs (Fig. 4b,d and Extended Data Fig. 7e). This upregulation was observed
319 even for Vortioxetine and Brexpiprazole, both lacking DTC-annotations at the time of analysis and thus
320 not contributing to the COSTAR training (Fig. 4d). We saw rapid and sustained upregulation of AP-1 TFs
321 JUN and FOS, as well as BTG1, a close homologue of BTG2 identified by COSTAR^{57,58} (Fig. 4b,d). JUN
322 and FOS are context-dependent oncogenic factors as well as canonical 'immediate-early genes' (IEGs)
323 that are rapidly induced upon neural activity^{53,54,59}. The presence of other upregulated IEGs, including
324 NR4A1, EGR1 and ARC, strengthened this surprising involvement of neural-activity dependent signaling
325 in glioblastoma (Fig. 4b).

326 To find key upstream regulators mediating the transcriptional response to PCY-hit NADs, we performed
327 transcription factor binding-site (TFBS) enrichment analysis of the upregulated genes (Fig. 4c and
328 Extended Data Fig. 7f). The most significantly enriched TF motifs at 6 hours were AP-1, ATF (a member
329 of the AP-1 superfamily), and CREB (a calcium-activated regulator of AP-1 transcription)^{53,60,61} (Fig. 4c).
330 Not only were AP-1 TFs the most enriched binding domain, but their own expression was also directly
331 induced upon PCY-hit NAD treatment (Fig. 4b,d and Extended Data Fig. 7e). ATF3 was the most
332 significantly upregulated gene across both time-points, while ATF4, JUN, JUNB, FOS, and FOSB were
333 among top differentially expressed genes (Fig. 4b,d and Extended Data Fig. 7c). Induction of AP-1

334 factors was primarily NAD-specific, where ONCD treatment did not elicit a similar global transcriptional
335 response (Fig. 4d and Extended Data Fig. 7c). Though NAD-induced AP-1 expression was sustained
336 across both time-points, TFBS enrichment analysis of upregulated genes at the 22 hour time-point
337 identified forkhead TF family members (e.g. FOXO1, FOXO3, FOXD3, HFH1) as a gene regulatory
338 module succeeding AP-1 Extended Data Fig. 7f). AP-1 and forkhead TFs have well-established roles in
339 mediating immediate-early response to neural activity and regulating long-term cell differentiation,
340 respectively^{53,54,62-64}.

341 Upstream of AP-1, a rapid Ca²⁺ influx and calcium-dependent signaling typically precede IEG expression
342 and AP-1 activation^{53,61,65,66}. We therefore measured both NAD-mediated endoplasmic reticulum (ER)
343 calcium store release as well as extracellular calcium influx in LN-229 cells by high-throughput FLIPR
344 calcium assays (n=17-18 drugs; Supplementary Table 3). While none of the tested drugs triggered ER
345 Ca²⁺ store release, we observed an immediate and strong extracellular Ca²⁺ influx in response to 5 out
346 of 8 of our PCY-hit NADs (Fig. 4e,f and Extended Data Fig. 8a,b). The strongest Ca²⁺ influx was observed
347 upon Vortioxetine treatment, while two additional antidepressant hits, Paroxetine and Fluoxetine, also
348 elicited strong responses (Fig. 4e,f). In contrast, the PCY-neg NADs (n=6) including two other
349 antidepressants, and ONCD-hits (n=2; Elesclomol, TMZ) did not trigger calcium influx (Fig. 4e,f). These
350 results demonstrate that, for the majority of our top NADs, a rapid drug-induced Ca²⁺ influx precedes
351 IEG upregulation and subsequent anti-glioblastoma activity.

352 Downstream of AP-1, we evaluated whether BTG tumor suppressors could be direct effectors of the
353 AP-1 gene regulatory network. BTG1 was one of the top 20 most significantly induced genes by the
354 PCY-hit NADs (Fig. 4b,d and Extended Data Fig. 7c). BTG2 was strongly induced in specific conditions,
355 including Vortioxetine and Paroxetine treatment (Fig. 4d). To delineate regulators of BTG family genes,
356 we leveraged genome-wide mapping of transcriptional regulatory networks by PathwayNet, a tissue-
357 aware data integration approach that utilizes 690 ChIP-Seq datasets from the ENCODE project⁶⁷. The
358 most enriched transcriptional regulators of BTG1/2 were members of the AP-1 TF network (e.g. JUN,
359 ATF3, FOS), implying BTG tumor suppressor gene expression is directly mediated by AP-1 factors (Fig.
360 4g).

361 Congruence between NAD-induced AP-1 activation and its anti-glioblastoma activity would strengthen
362 a causal role for this gene regulatory network. Remarkably, drug-induced expression of AP-1 TFs and
363 BTG genes (the 'COSTAR signature') was highly correlated with a drug's *ex vivo* anti-glioblastoma
364 efficacy in patient samples (R=0.72, P=1.4e-05; Fig. 4h). We additionally performed BTG1/2 and JUN
365 loss-of-function experiments by siRNA-mediated knockdown in LN-229 cells. Quantitative RT-PCR after
366 72 hours of gene silencing confirmed reduced expression of BTG1/2 and JUN and revealed
367 interdependent regulatory interactions governing their expression (Extended Data Fig. 8c). BTG1 but
368 not BTG2 inhibition accelerated cell growth measured by live-cell imaging across 7 days (Fig. 4i).
369 Increased cell proliferation upon BTG1 inhibition was also validated by endpoint pharmacoscopy after
370 3 days (Fig. 4j). By DRUG-Seq analysis, BTG1 induction represented a pan-NAD signature, while BTG2
371 was induced only in specific drug conditions such as Vortioxetine treatment (Fig. 4d). Vortioxetine also
372 triggered the strongest calcium increase and represented the most effective NAD overall by
373 pharmacoscopy. We therefore next evaluated the functional dependencies of Vortioxetine anti-
374 glioblastoma efficacy on BTG1/2 and JUN. After two days of siRNA-mediated gene silencing and one
375 subsequent day of drug treatment, BTG1 inhibition rescued Vortioxetine-mediated cell death (Fig. 4j).

376 Together, these results propose a model in which a subset of neuroactive drugs mediate anti-
377 glioblastoma activity by triggering a rapid calcium influx, IEG and AP-1 transcription factor activation,

378 followed by engagement of an antiproliferative program that includes BTG-driven tumor suppression
379 (Fig. 4k).

380 **Potent and rapid AP-1 induction by Vortioxetine**

381 To closer examine the temporal dynamics of the most effective neuroactive drug, Vortioxetine, we
382 performed in-depth transcriptomic and proteomic profiling at 3-6 time-points in LN-229 cells (Fig. 5a
383 and Extended Data Fig. 8d-h). Gene expression change over time was the strongest driver of variance
384 in Vortioxetine-treated RNA samples analyzed by principal component analysis (Extended Data Fig.
385 8d). Among the top 100 gene loadings for PC1 (38.9% explained variance), we observed induction of
386 AP-1 TFs FOS, JUNB, ATF4, and the AP-1 effector gene ARC already at 3 hours (Fig. 5a and Extended
387 Data Fig. 8e). At the RNA level, 10 AP-1 TFs were significantly upregulated at all time-points, with
388 temporal dynamics depending on individual TFs (Fig. 5a and Extended Data Fig. 8e). At the protein
389 level, gene set enrichment analysis (GSEA) at 3 hours revealed DNA-binding transcription activator
390 activity as the most over-represented gene ontology (GO) term (Extended Data Fig. 8f-h). Rapid and
391 sustained protein expression of AP-1 TFs was observed between 3 and 9 hours, coinciding with
392 upregulation of BTG1/2 and other negative regulators of cell cycle such as CDKN1B and PPM1B (Fig. 5a
393 and Extended Data Fig. 8f,h). Significant activation of MAPK, ER stress response, and DNA damage
394 pathways were also observed (Fig. 5a). Conversely, cytoskeletal components and oncogenic RTKs
395 associated with the malignant phenotype of glioblastoma, including EGFR, NTRK2, and PDGFRA, were
396 downregulated upon Vortioxetine treatment (Fig. 5a).

397 AP-1 activity and function in tumorigenesis can be context- and cell type-dependent⁵⁹. Consequently,
398 we set out to confirm AP-1 induction upon NAD treatment in compositionally heterogeneous
399 glioblastoma patient samples taken directly after surgery. We examined AP-1 expression both at the
400 single-cell gene and protein level.

401 We first performed scRNA-Seq on cells from patient P024 following 3 hours of *ex vivo* Vortioxetine
402 treatment (Fig. 5b,c and Extended Data Fig. 9a,b). Analysis of 1736 single-cell transcriptomes revealed
403 4 main clusters with intermixed Vortioxetine-treated and DMSO-control cells (Extended Data Fig. 9a).
404 Cluster 1 represented the most malignant cluster with highest expression levels of glioblastoma
405 stemness markers such as Nestin, Ki67, CCND2, and VEGFA. Cluster 2 and 3 also expressed
406 glioblastoma stemness markers, at lower levels than cluster 1. Cluster 4 represented an immune
407 cluster, with the highest expression of the pan-immune marker CD45 (Fig. 5b and Extended Data Fig.
408 9b). Per-cluster comparison of Vortioxetine-treated versus DMSO-control cells revealed glioblastoma-
409 specific induction of AP-1 factors upon Vortioxetine treatment (Fig. 5c). For example, JUNB, JUND, and
410 AP-1 effector gene ARC were upregulated in cluster 1, while ATF4 and MAF were induced in all three
411 glioblastoma clusters (cluster 1-3), with a more pronounced induction of ATF4 in clusters 2 and 3 (Fig.
412 5c).

413 Next, we performed immunofluorescence against JUND, ATF4, FOS and the AP-1 effector gene
414 HOMER1 in three additional glioblastoma patient samples (P039, P040, P042) after Vortioxetine
415 treatment (Fig. 5d,e). AP-1 factor induction in Nestin+ glioblastoma cells was observed in a patient-,
416 time-point, and concentration-dependent manner. The strongest induction of all tested AP-1 factors
417 was seen in patient sample P040 that had high abundance of complex morphotypes (M1-M3), which
418 were reduced upon Vortioxetine treatment (Fig. 5d,e). HOMER1 and ATF4 were induced in all three
419 patient samples, while FOS and JUND exhibited more patient variability (Fig. 5d). Together, this

420 detailed analysis of Vortioxetine response highlights the added layer of complexity relating to
421 heterogeneous cellular states across cell types and patients, and supports our transcriptomic and
422 functional data elucidating AP-1 induction to be a key neural vulnerability hijacked by PCY-hit NADs.

423 Preclinical translation of neuroactive drugs

424 Vortioxetine elicits a strong Ca²⁺ influx and subsequent AP-1 response, reduces aggressive GSC
425 morphologies, and potently induces cell death of glioblastoma cells *ex vivo*. To determine if
426 Vortioxetine affects other tumor properties that contribute to recurrence such as invasiveness and
427 long-term growth, we performed a series of experiments to test the effect of Vortioxetine on cell
428 invasion, clonogenic survival, and spheroid formation using established human long-term glioma cell
429 lines (LN-229, LN-308) and glioma-initiating cells (ZH-161, ZH-562) (Extended Data Fig. 9c-f). In a
430 collagen-based spheroid invasion assay, Vortioxetine decreased the average migration distance and
431 reduced the number of invading cells in 3 out of 4 lines (Extended Data Fig. 9c,d). In a resazurin-based
432 clonogenic survival assay, Vortioxetine strongly impaired long-term cell viability in a concentration-
433 dependent manner across all cell lines (4 out of 4 lines, Extended Data Fig. 9e). In a complementary 3D
434 spheroid-formation assay, Vortioxetine potently inhibited tumor growth over time (Extended Data Fig.
435 9f). These results demonstrate the multifaceted anti-tumor effects of Vortioxetine upon glioblastoma
436 invasion, survival, and proliferation.

437 Finally, we tested the top *ex vivo* NAD hits including Vortioxetine (PCY-hit NADs; n=4 or 5 drugs across
438 different drug classes) in orthotopic human-xenograft glioblastoma mouse models (Fig. 5f and
439 Extended Data Fig. 10a-c). To account for the variability observed in different orthotopic models, we
440 tested two different models (LN-229, ZH-161) across three independent trials (Trials I-III) of drug-
441 testing *in vivo* (Fig. 5f and Extended Data Fig. 10a). We included Temozolomide (TMZ) as a positive
442 control, and as negative controls we tested one PCY-neg NAD Paliperidone and a vehicle control. Since
443 all tested NADs have confirmed BBB-penetrance and are approved for other neurological disorders, *in*
444 *vivo* concentrations were determined *a priori* based on literature and clinical evidence⁶⁸⁻⁷³.
445 Vortioxetine was consistently the most effective drug (in 3/3 trials) and showed significant survival
446 benefit comparable to TMZ despite being tested at considerably lower dosage (Fig. 5f). Brexpiprazole
447 was the 2nd-best PCY-hit NAD *in vivo* (2/3 trials), while other NADs showed a significant survival benefit
448 in 1 out of 3 trials (Extended Data Fig. 10a). Consistent with PCY, the negative control Paliperidone did
449 not show a significant survival benefit (2/2 trials) (Fig. 5f). In the most aggressive orthotopic model
450 with the shortest median survival of the vehicle control, Vortioxetine and TMZ were the only effective
451 drugs (Trial II: ZH-161; Fig. 5f, right), whereas for the least aggressive model, all tested PCY-hit NADs
452 (5/5 NADs) significantly prolonged survival (Trial III: ZH-161; Extended Data Fig. 10a). MRI images of
453 ZH-161 transplanted mice (Trial II) after 15 days of Vortioxetine, Apomorphine, and Temozolomide
454 treatment showed marked reduction of tumor size (Extended Data Fig. 10b,c). The striking consistency
455 of our patient *ex vivo* and mouse *in vivo* results demonstrate strong translatability of PCY-based NAD
456 discovery and confirm Vortioxetine as the most promising clinical candidate.

457 Given the different mechanisms of neuroactive drugs and approved chemotherapies, their successful
458 combination could facilitate the rapid adoption of NADs into clinical routine. Therefore, we tested the
459 combination of Vortioxetine with either first- or second-line standard of care drugs for glioblastoma,
460 TMZ and Lomustine (CCNU) *in vivo* (Trial IV: ZH-161; Fig. 5g). All three single agents significantly
461 prolonged survival, with Vortioxetine results now confirmed in 4 out of 4 *in vivo* trials (Fig. 5f,g).
462 Remarkably, compared to TMZ or CCNU single agents, the combination of Vortioxetine with either

463 drug provided even further survival benefit, with a median survival increase of 20-30% compared to
464 the single agents (Fig. 5g). Given the dire need for effective treatment options in glioblastoma, this
465 strong preclinical evidence of the safe antidepressant Vortioxetine urges for clinical investigation in
466 patients.

467 Discussion

468 Here we present the first therapeutic single-cell map across glioblastoma patient samples that reveals
469 the morphological and neural molecular heterogeneity of glioblastoma. Glioblastoma stem cells adopt
470 distinct cell morphological states that encode clinical prognostic value. While the presence of tumor
471 microtubules has been associated with tumor grade², we show that even within glioblastoma, complex
472 GSC morphologies are prognostic of shorter progression-free survival. Image-based drug screening in
473 the context of heterogeneous patient samples predicted clinical response to chemotherapy and
474 enabled the discovery of repurposable neuroactive drugs that target the spectrum of glioblastoma
475 cells across 27 patients and various model systems, greatly expanding upon prior literature^{74–76}.

476 A number of new personalized therapeutic opportunities emerge from our exploratory drug response
477 analysis across a genetically and clinically heterogeneous patient cohort. These include Elesclomol
478 sensitivity increasing with age, Abemaciclib response associating with p53 mutant status, and higher
479 Brexpiprazole response in men. Response to the antidepressant Vortioxetine, the most promising
480 preclinical candidate, was particularly aligned with aggressive GSC morphotypes present in patients
481 with poor prognosis. These efforts contribute to the nascent community of glioblastoma research
482 focusing on the investigation of patient-derived tumor explants that facilitate translational
483 investigation of complex tumor behavior, including the development of genetically characterized
484 patient cultures, organoid biobanks, and regionally annotated samples^{29,77–82}.

485 Our systematic analysis of the neuroactive drug mechanisms, drug target expression, and functional
486 genetic dependencies indicated a diverse set of possible neural vulnerabilities of glioblastoma. Given
487 this diversity, it is surprising that our interpretable machine learning approach COSTAR identified a
488 simple drug-target connectivity signature predictive of anti-glioblastoma efficacy. COSTAR effectively
489 applies Occam's razor to the collective biochemical drug-protein-protein interaction networks, offering
490 a novel conceptual framework applicable to all fields of drug discovery. Through COSTAR, we
491 uncovered a convergence of AP-1 transcription factor activity and cell cycle regulation on BTG-
492 mediated tumor suppression. AP-1 and BTG upregulation was a defining feature of the response to
493 neuroactive drugs with anti-glioblastoma activity, where a growth-suppressing role for BTG1 was
494 confirmed by functional genetics. While the defining pharmacological properties remain to be
495 identified, our results indicate a plurality of drug mechanisms converging on this novel tumor-
496 suppressing pathway.

497 Previous studies have demonstrated the role of neuronal activity in regulating glioblastoma growth at
498 the brain-tumor interface, highlighting the influence of the tumor microenvironment in mediating the
499 neural behavior of the tumor. Here we reveal that cell-*intrinsic* neural activity in glioblastoma mimics
500 those of neural lineage cells, offering a therapeutic vulnerability that enables direct targeting of the
501 tumor. In neurons, immediate early gene expression including AP-1 is typically a hallmark of neural
502 activity or insult, but in cancer cells, AP-1 factors were originally described as context-dependent
503 oncogenes. We now find that neuroactive drugs can hijack this activity-dependent neural signaling,
504 triggering a strong transcriptional response that, in the context of glioblastoma cells, leads to rapid cell

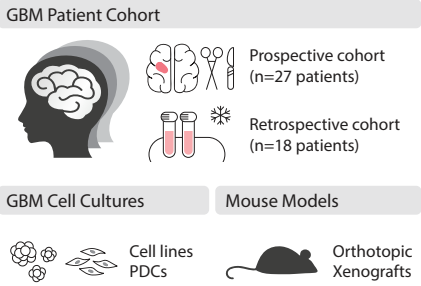
505 death. Treating glioblastoma tailored to the cellular history and lineage of the cancer rather than its
506 unstably transformed state may represent new hope for this devastating disease.

507 **Acknowledgements**

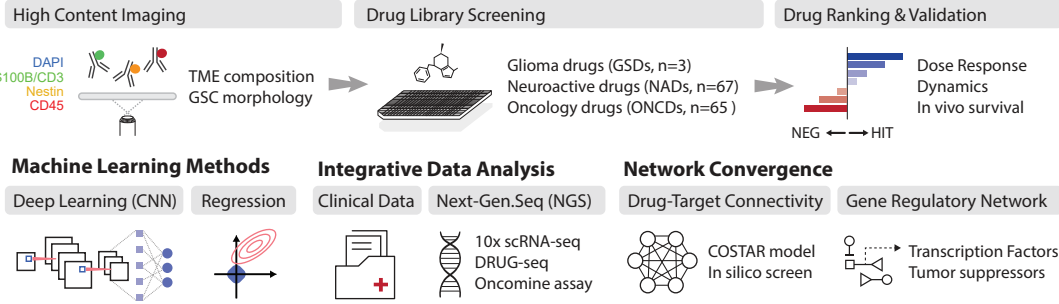
508 We thank the patients and their families for making this study possible. We thank core facilities at ETH
509 Zurich and University of Zurich, including the Functional Genomics Center Zurich (FGCZ), the Flow
510 Cytometry Core Facility (EPIC, FCCF), and central informatics services (ID). This project has received
511 funding from the European Research Council (ERC) under the European Union's Horizon 2020 research
512 and innovation programme (Grant agreement No. 803063-SCIPER; BS), and from the Personalized
513 Health and Related Technologies (PHRT) Strategic Focus Area of the ETH Domain (Project #2021-566;
514 BS). We further acknowledge funding from the European Union/European Commission (MSCA
515 Individual Fellowship; SL), the European Molecular Biology Organization (EMBO Long-term Post-
516 doctoral Fellowship; SL), the Swiss National Science Foundation (grant no. 310030_204972; MAH), and
517 financial support from the Department of Biology as well as the Institute of Molecular Systems Biology
518 of the ETH Zurich. We thank the research and administrative staff who helped us throughout the study,
519 including Yasmin Festl and Silas Krämer, and members of the Snijder lab for discussions.

Figure 1

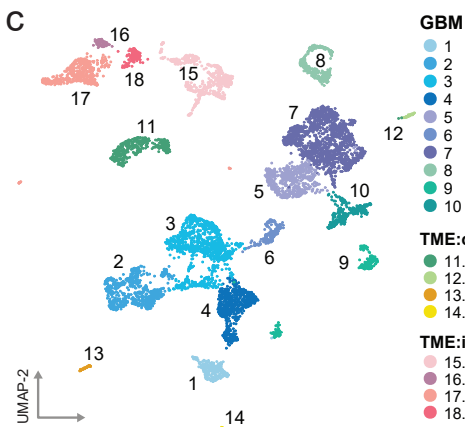
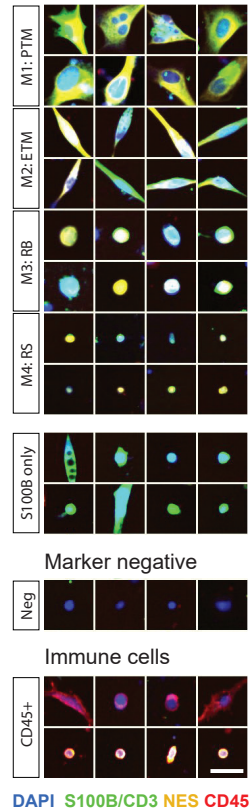
a Glioblastoma (GBM) Disease Models



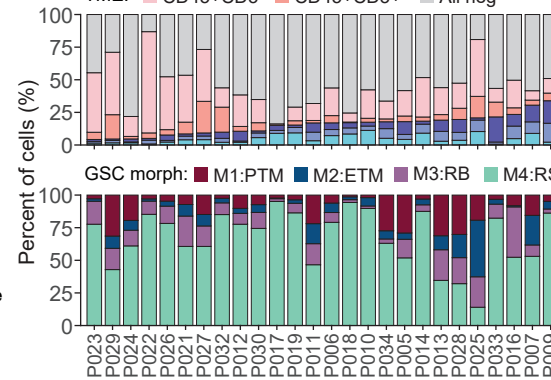
Pharmacoscopy (PCY)



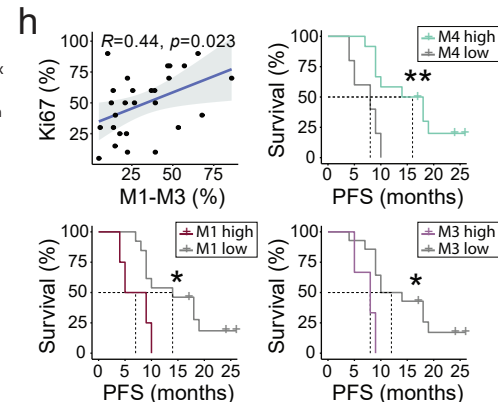
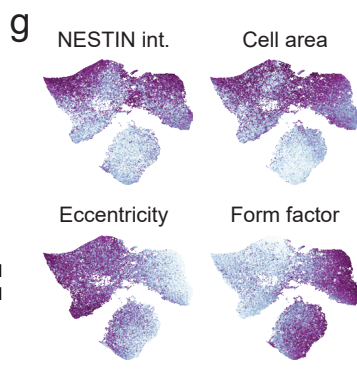
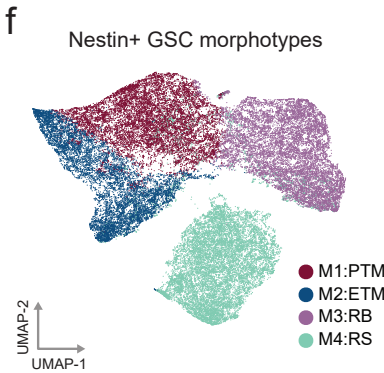
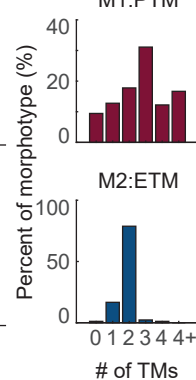
b Glioblastoma cells



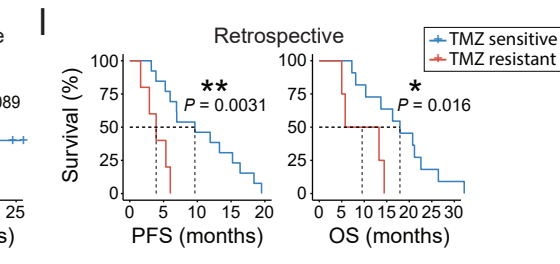
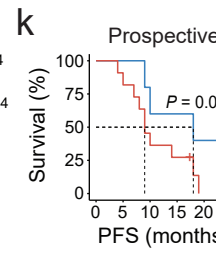
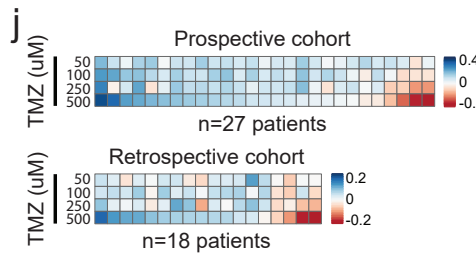
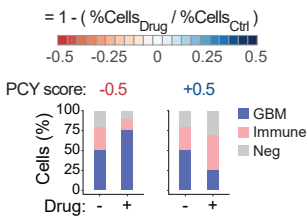
d GBM: NES+ only, NES+S100B+, S100B+ only



e M1:PTM, M2:ETM



i Pharmacoscopy (PCY) score



520 Figure Legends

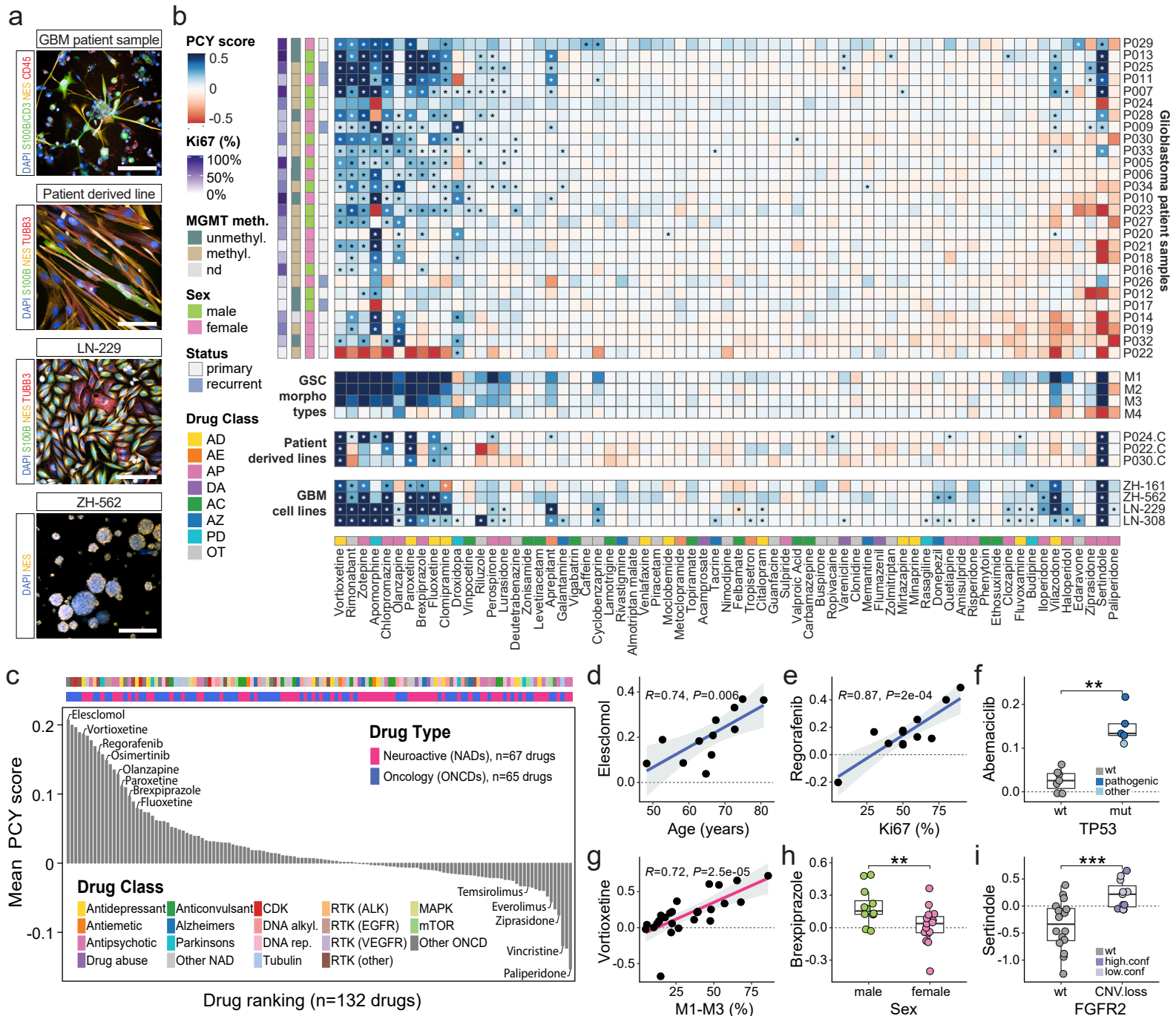
521 Fig. 1: Neural intratumor heterogeneity across glioblastoma patients relates to 522 disease prognosis and response to first-line therapy

523 **a**, Comprehensive workflow integrating glioblastoma disease models with image-based *ex vivo* drug
524 screening (pharmacoscopy; PCY), machine learning methods, clinical data, and next-generation
525 sequencing (NGS) to discover therapeutic neural vulnerabilities underlying glioblastoma. Glioblastoma
526 disease models include surgery material from glioblastoma patient samples (prospective cohort; n=27
527 patients, retrospective cohort; n=18 patients), patient-derived lines (PDCs, n=3 lines), glioblastoma cell
528 lines (n=4 lines), and mouse models (n=2 human xenograft models). Different cell types present in the
529 tumor microenvironment (TME) of glioblastoma patient samples are identified by both
530 immunofluorescence (S100B, Nestin, CD3, CD45, DAPI) and single-cell RNA-Seq (10x). Glioblastoma
531 stem cell (GSC; Nestin+ cells) morphologies are classified into four morphotypes by deep learning
532 (convolutional neural network; CNN). Pharmacoscopy measures the relative changes in TME
533 composition and GSC morphotypes across drug treatments to identify drugs with anti-glioblastoma
534 efficacy (PCY-hit). Drug-target connectivity mapping of PCY-hit drugs by a novel machine learning
535 method (convergence of secondary drug-targets by analyzed by regularized regression; COSTAR)
536 together with multiplexed RNA-Seq (DRUG-Seq) enables the discovery of convergent gene regulatory
537 networks involved in glioblastoma suppression. **b**, Compositional and morphological diversity of
538 glioblastoma patient samples are captured with single-cell resolution by high-content imaging.
539 Glioblastoma cells (Nestin+ or S100B+) include S100B only cells (S100B+Nestin-CD45-) and four
540 Nestin+CD45- GSC morphotypes: M1 polygonal multi-tumor microtubule cells (M1:PTM), M2 elongated
541 uni/bi-tumor microtubule cells (M2:ETM), M3 round big cells (M3:RB), and M4 round small cells (M4:RS).
542 Other cell types include immune cells (CD45+ only, CD45+CD3+) and marker-negative cells. Scale bar,
543 30µm. **c**, UMAP projection of 7684 single-cell transcriptomes from four glioblastoma patient samples
544 (P007, P011, P012, P013) colored by cluster-id (see legend). Clusters are based on Leiden community
545 detection and cell types assigned by marker expression (*Extended Data Figure 1f*). Glioblastoma (GBM)
546 clusters (1-10) are numbered in descending order based on cluster-averaged expression of the Gene
547 Ontology term “stem cell differentiation” (GO:0048863). OPC; oligodendrocyte precursor cells. EC;
548 endothelial cell. TAM; tumor-associated macrophage. NK; natural killer cell. TME; tumor
549 microenvironment. **d**, Cellular (top) and morphological (bottom) composition across the prospective
550 glioblastoma cohort (n=27 patients; columns). Cellular composition is based on glioblastoma and TME
551 populations defined by marker expression and morphological composition is based on Nestin+ GSCs
552 classified by deep learning into four morphotypes (M1-M4). **e**, Frequency of tumor microtubules (TMs)
553 per cell in TM-containing morphotypes M1 (n=180 cells) and M2 (n=264 cells). **f-g**, UMAP projection of
554 the morphological CNN feature space of 84,180 single-cells (up to n=1000 cells per morphotype and
555 patient, n=27 patients). CNN feature space consists of ten-dimensional activations taken from the 2nd-
556 last fully connected layer of the network. **f**, Cells are colored by their assigned morphotype (M1-M4).
557 **g**, Cells are colored by the local median of selected single-cell features (see also *Extended Data Figure*
558 *2c*). Eccentricity and form factor are shape indices related to the irregularity and circularity of a cell.
559 Nestin Int.; Nestin expression measured by immunofluorescence. **h**, (Top left) Correlation of
560 histopathological Ki67 labeling index with abundance of M1-M3 morphotypes per patient. Linear
561 regression line (dark blue) with a 95% confidence interval (light grey). Pearson correlation coefficient
562 $R=0.44$, P -value 0.023. (Top right and bottom panels) Morphotype abundance-based stratification of

563 progression-free survival (PFS) in primary glioblastoma patients (n=17 patients) plotted as Kaplan-
564 Meier survival curves. (Top right) M4-high; n=12, M4-low; n=5 patients; $P=0.0047$. (Bottom left) M1-
565 high; n=4, M1-low; n=13 patients; $P=0.021$. (Bottom right) M3-high; n=3, M3-low; n=14 patients;
566 $P=0.018$. **i**, Schematic illustrating pharmacoscopy (PCY) score calculation. The PCY score quantifies
567 drug-induced on-target killing by measuring the change in fraction of a defined target population (blue;
568 relative reduction, red; relative increase) compared to vehicle control (-). Bar plot example of two
569 opposing cases scoring a relative 50% decrease (score=0.5) or relative 50% increase (score -0.5) of
570 glioblastoma cells in response to a drug. **j**, Temozolomide (TMZ) *ex vivo* drug response across four TMZ
571 concentrations 50, 100, 250, and 500 μ M (rows) per patient (columns) for two patient cohorts (top:
572 prospective cohort, n=27 patients; bottom: retrospective cohort, n=18 patients). Heatmap color scale
573 indicates the PCY score of glioblastoma cells (Nestin+ or S100B+). Outliers beyond color scale limits
574 were correspondingly set to minimum and maximum values. **k-l**, Temozolomide (TMZ) *ex vivo*
575 sensitivity-based stratification of primary glioblastoma patient survival plotted as Kaplan-Meier curves.
576 All patients received TMZ as 1st-line treatment in the clinic with censored patients in the prospective
577 cohort indicating ongoing responses (tick marks). *Ex vivo* TMZ sensitivity is calculated as the mean PCY
578 score across four TMZ concentrations 50, 100, 250, and 500 μ M. **k**, Progression-free survival (PFS) of
579 the prospective glioblastoma cohort (n=16 patients; $P=0.089$). **l**, Progression-free survival (PFS;
580 $P=0.0031$; left) and overall survival (OS; $P=0.016$; right) of the retrospective validation cohort (n=18
581 patients). **h,k-l**, Survival curves are compared using the log-rank (Mantel-Cox) test and the optimal cut-
582 point (high, low) for continuous parameters to stratify patients was determined by maximally selected
583 rank statistics. P -values: not significant (ns), $P > 0.05$, * $P < 0.05$, ** $P < 0.01$, *** $P < 0.001$,
584 **** $P < 0.0001$.

Figure 2

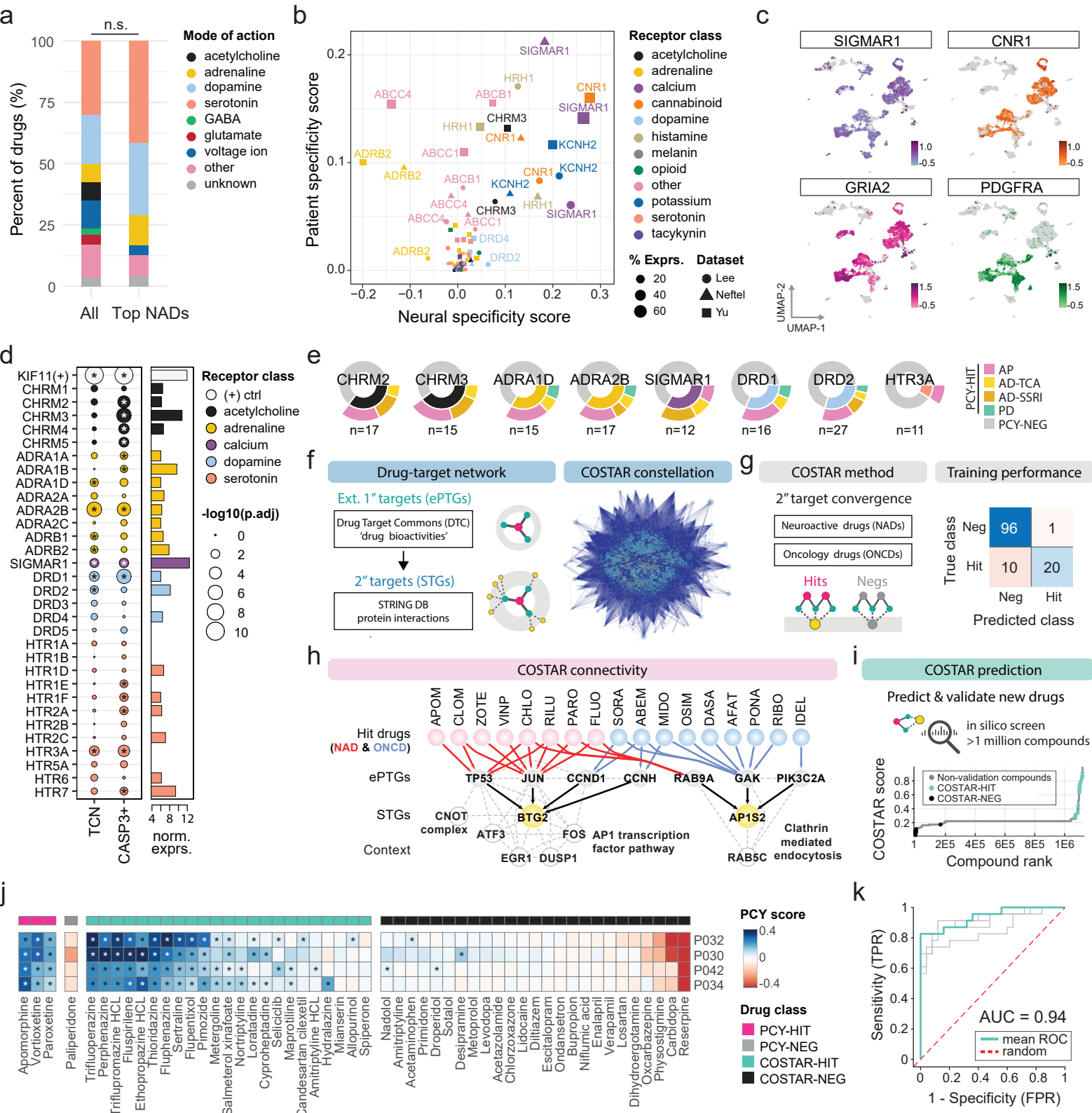
bioRxiv preprint doi: <https://doi.org/10.1101/2022.10.07.511321>; this version posted October 7, 2022. The copyright holder for this preprint (which was not certified by peer review) is the author/funder, who has granted bioRxiv a license to display the preprint in perpetuity. It is made available under aCC-BY-NC-ND 4.0 International license.



585 **Fig. 2: Image-based single-cell drug profiling across a heterogeneous patient cohort**
586 **and model systems identifies repurposable drugs for glioblastoma treatment**

587 **a**, Representative immunofluorescence images of a glioblastoma patient sample (P040; scale bar,
588 100 μ M), a patient-derived cell line (P040.PDC; 100 μ M), an adherent glioblastoma cell line (LN-229;
589 scale bar, 150 μ m), and a glioblastoma-initiating cell line (ZH-562, scale bar, 250 μ m). Cells are labeled
590 with the nuclear stain DAPI (blue), mature astrocyte marker S100B (green), and neural progenitor
591 marker Nestin (yellow). Other markers are indicated in their respective colors. **b**, Drug response matrix
592 of neuroactive drugs (NADs, n=67 drugs) across glioblastoma patient samples (n=27 patients), GSC
593 morphotypes (n=4 classes), patient-derived lines (PDCs; n=3 lines, denoted by ".C" following patient
594 id), and glioblastoma cell lines (n=4 lines). Heatmap color scale indicates the PCY score of glioblastoma
595 cells (defined as Nestin+ or S100B+ cells in patient samples; Nestin+ cells in PDCs; total cell number in
596 LN-229/308 lines; spheroid area in ZH-161/562 lines) or the average PCY score of GSC morphotypes
597 (M1-M4) across patients. Outliers beyond color scale limits were correspondingly set to minimum and
598 maximum values. Annotations per patient sample (rows; left of heatmap) indicate the clinical
599 parameters Ki67 labeling index, MGMT promoter methylation status (unmethyl; unmethylated,
600 methyl; methylated, nd; not determined), Sex, and recurrent tumor status (Status). *See also Extended*
601 *Data Figure 1a and Supplementary Table 2 for tumor mutational status*. Annotation per drug (columns;
602 underneath heatmap) indicates neuroactive drug class. Asterisks (*) denote FDR-adjusted $P < 0.05$. **c**,
603 Drug ranking (n=132 repurposable drugs) according to their mean Nestin+ or S100B+ PCY scores across
604 glioblastoma patients (NADs; n=27 patients, ONCDs; n=12 patients). Annotations per drug indicate
605 drug type (NADs; n=67 drugs, ONCDs; n=65 drugs) and drug class. RTK; receptor tyrosine kinase, alkyl;
606 alkylation, rep; replication. **d-i** Genetic and clinical associations with *ex vivo* drug response across
607 patients. Glioblastoma PCY scores (y-axis) are plotted per patient against selected parameters (x-axis).
608 **d**, Correlation of patient age at diagnosis with *ex vivo* Elesclomol response ($R=0.74$; $P = 0.006$). **e**,
609 Correlation of histopathological Ki67 labeling index with *ex vivo* Regorafenib response ($R=0.87$; $P =$
610 0.0002). **f**, Association of *TP53* mutational status with *ex vivo* Abemaciclib response ($P = 0.0025$). **g**,
611 Correlation of complex GSC morphotype abundance (M1-M3) at baseline with *ex vivo* Vortioxetine
612 efficacy. **h**, Association of sex with *ex vivo* Brexpiprazole response ($P = 0.0063$). **i**, Association of *FGFR2*
613 copy number loss with *ex vivo* Sertindole response ($P = 0.0008$). CNV; copy number variation.
614 High.conf; high confidence. Low.conf; low confidence. *See Extended Data Figure 3f,g for full*
615 *pharmacogenetic analysis results*. **d,e,g**, Linear regression line with a 95% confidence interval. Pearson
616 correlation coefficients with P -values annotated. **f,h,i**, P -values calculated from a two-sided Wilcoxon
617 rank sum test. P -values: not significant (ns), $P > 0.05$, * $P < 0.05$, ** $P < 0.01$, *** $P < 0.001$,
618 **** $P < 0.0001$. Boxplots show 25th–75th percentiles with a line at the median; whiskers extend to
619 1.5 times the interquartile range.

Figure 3



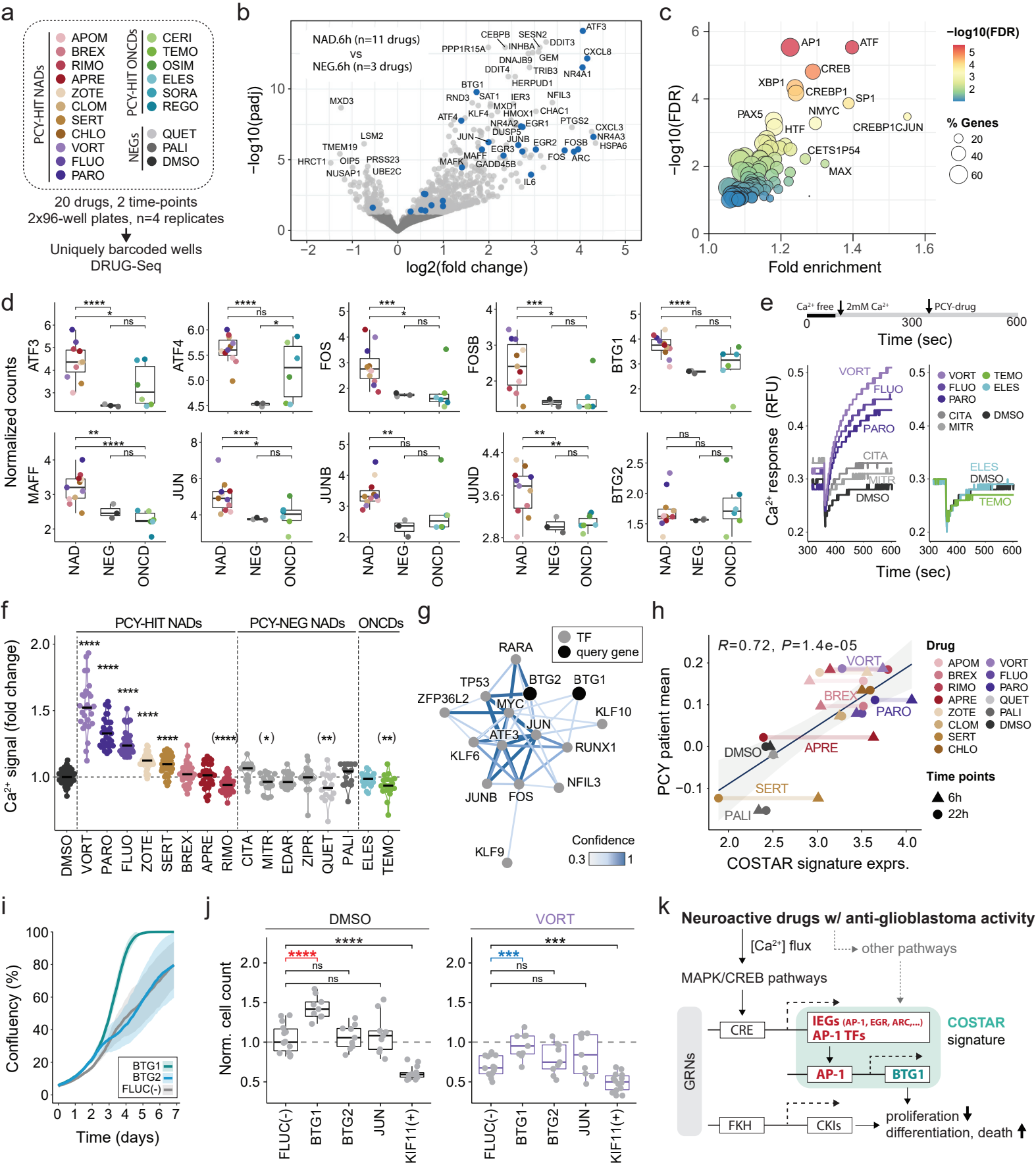
620 **Fig. 3: Neuroactive drugs with anti-glioblastoma efficacy converge upon a predictive**
621 **AP-1 and cell cycle connectivity signature through divergent primary targets**

622 **a**, Drug mode-of-action for all neuroactive drugs (n=67 drugs; left) and top neuroactive drug hits (n=15
623 drugs with a mean patient PCY score > 0.03; right) represented as stacked bar plots. Hypergeometric
624 test shows no enrichment in mode-of-action: n.s., not significant. **b**, Primary target gene (PTG)
625 expression of neuroactive drugs in 22 glioblastoma patient samples across three independent scRNA-
626 Seq datasets (Lee *et al.*, this study; n=4 patients, n=7684 cells; Neftel *et al.*, n=9 patients, n=13519 cells;
627 Yu *et al.*, n=9 patients, n=4307 cells) plotted as the neural specificity score (x-axis) versus patient
628 specificity score (y-axis) for each PTG. See also Extended Data Figure 5b & Methods. Each dot
629 represents a gene, shape corresponds to the dataset, and size scales with percent of expressed cells.
630 Color represents the receptor class of each PTG. **c**, scRNA-Seq log₁₀(expression) of selected
631 neuroactive PTGs (*SIGMAR1*, *CNR1*, *GRIA2*) and oncogenic RTK (*PDGFRA*) visualized on a UMAP
632 projection of 7684 single-cell transcriptomes (Lee *et al.*, this study, n=4 glioblastoma patients). **d**,
633 siRNA-mediated gene silencing of PTGs in LN-229 cells. Total cell number reduction (TCN) and cleaved
634 CASP3+ fraction increase (CASP3+) depicted as a circle per gene. Circle sizes scale with the -log₁₀ (FDR-
635 adjusted P-value) and color represents the receptor class of each PTG. See also Extended Data Figure
636 5c,d for additional receptor classes and PCY scores. Adjacent horizontal bar plot represents baseline
637 expression (DESeq2 vsd-normalized RNA-Seq counts) of each PTG in LN-229 cells. Asterisks (*) denote
638 FDR-adjusted P < 0.05. **e**, Fraction of PCY-HIT vs PCY-NEG drugs associated with PTGs based on the
639 Drug Target Commons (DTC)⁵², where the number of drugs (n) denotes drugs with annotations for a
640 given gene. Representative PTGs with the strongest glioblastoma gene dependencies of each receptor
641 class visualized. Inner circle color corresponds to receptor class in Figure 3d for PCY-HIT drugs, while
642 PCY-NEG drugs are in grey. PCY-HIT drugs are subdivided and colored according to their drug class. AP;
643 antipsychotic, AD-TCA; antidepressant -tricyclic, AD-SSRI; antidepressant-selective serotonin reuptake
644 inhibitor, PD; Parkinson's disease. **f**, Convergence of secondary drug targets analyzed by regularized
645 regression (COSTAR). For all tested drugs, the extended primary targets (ePTG; 1'') were retrieved
646 from DTC, and expanded to include secondary targets (STG; 2'') based on protein-protein interactions
647 annotated by STRING-DB⁸³ (left). The resulting network, or 'COSTAR constellation' (right), contains 127
648 drugs, 975 ePTGs, 10573 STGs, and 114517 edges. **g**, Logistic LASSO regression is performed on the
649 COSTAR constellation to learn a linear model that discriminates pharmacoscopy hits (n=30, equally
650 split across NADs and ONCDs) from negative drugs (n=97) based on their secondary drug-target
651 connectivity (left). COSTAR training model performance is represented as a confusion matrix, where
652 the 'true' class denotes PCY-based experimental ground truth, and the 'predicted' class denotes the
653 COSTAR-prediction (right). **h**, COSTAR connectivity (solid lines) reveals convergence of NAD (red) and
654 ONCD (blue) hits to key ePTGs (grey) and STGs (yellow). See Extended Data Figure 6b for the full model.
655 Representative proteins/protein families with high confidence STRING-DB interactions to STGs are
656 shown as context (dashed lines). **i**, *In silico* COSTAR predictions based on drug-target connectivity
657 across 1,120,823 drugs annotated in DTC. Drugs are ranked (x-axis) by their predicted PCY-hit
658 probability (COSTAR score; y-axis). Predicted drug hits (COSTAR-HIT; mint green) and predicted non-
659 hits (COSTAR-NEG; black) selected for experimental validation are indicated. **j**, Experimental validation
660 of COSTAR-HIT (n=23; mint green) and COSTAR-NEG (n=25; black) drugs (columns) across four
661 glioblastoma patient samples (rows). Heatmap color scale indicates the PCY score of glioblastoma cells.
662 Additionally, positive (PCY-HITs; pink; n=3) and negative (PCY-NEG; dark grey; n=1) control drug
663 responses are shown. Outliers beyond color scale limits were correspondingly set to minimum and
664 maximum values. Asterisks (*) denote FDR-adjusted P < 0.05. **k**, Receiver Operating Characteristic

665 (ROC) curves describing the COSTAR validation accuracy in glioblastoma patient samples of the
666 COSTAR-predicted drugs (n=48 drugs). ROC curves per patient sample (grey, n=4 patients) and mean
667 across all patients (mint green) and corresponding Area Under the Curve (AUC) are shown. Dashed red
668 line denotes the ROC curve of a random classifier. Patient drug responses correspond to *Figure 3j*.

Figure 4

bioRxiv preprint doi: <https://doi.org/10.1101/2022.10.07.511321>; this version posted October 7, 2022. The copyright holder for this preprint (which was not certified by peer review) is the author/funder, who has granted bioRxiv a license to display the preprint in perpetuity. It is made available under aCC-BY-NC-ND 4.0 International license.

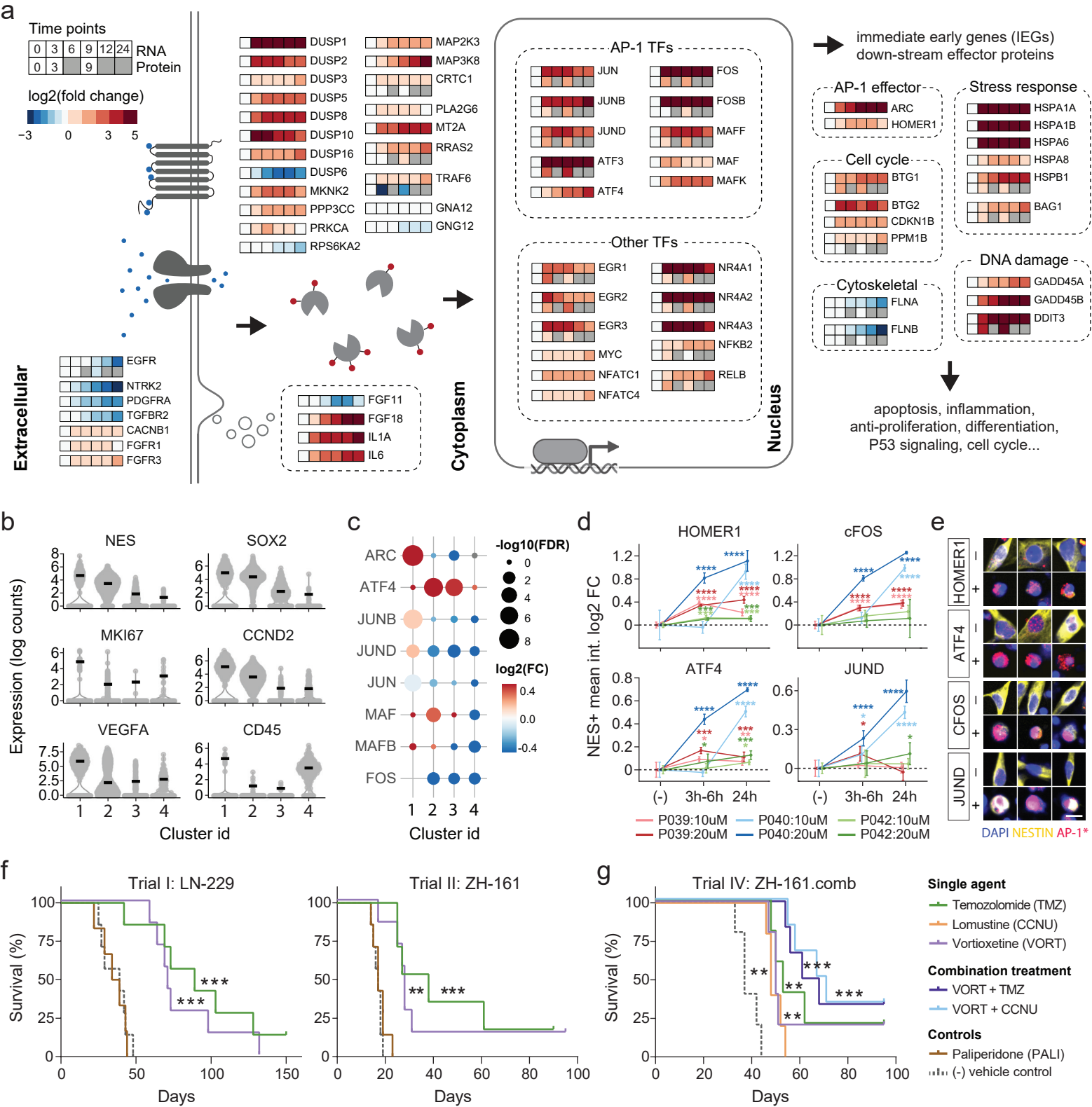


669 **Fig. 4: Glioblastoma suppression is driven by a tumor-intrinsic AP-1 gene regulatory**
670 **network upon neural activity**

671 **a**, Multiplexed RNA-Seq (DRUG-Seq) measures the transcriptional response to pharmacology-hit
672 neuroactive drugs (PCY-hit NADs, n=11 drugs), pharmacology-hit oncology drugs (PCY-hit ONCDs, n=6
673 drugs), and negative control drugs (NEGs, n=2 PCY-neg NADs and DMSO vehicle control). LN-229 cells
674 were treated with drugs across two different time-points (6, 22 hours) and uniquely barcoded for
675 sequencing (n=4 replicate wells per drug). **b**, Transcriptional response of PCY-hit NAD-treated cells
676 compared to NEG-treated cells (6h) shown as a volcano plot. X-axis: $\log_2(\text{fold change})$; y-axis: $-\log_{10}(\text{adjusted } P\text{-value})$. A positive $\log_2(\text{fold change})$ indicates upregulated genes upon PCY-hit NAD
677 treatment. Genes above a $-\log_{10}(0.05 \text{ adjusted } P\text{-value})$ threshold plotted as light grey dots, and non-
678 significant genes as dark grey dots. Highlighted genes (blue) include AP-1 transcription factor (TF)
679 network genes (Pathway Interaction Database; PID AP1 PATHWAY; ⁸⁴) and key COSTAR signature
680 genes. **c**, Transcription factor binding site enrichment analysis of significantly upregulated genes upon
681 PCY-hit NAD treatment (6 hours) in *Figure 4b*. Circles correspond to TF annotations, circle sizes scale
682 with the percent of genes present in the annotation, and colors indicate $-\log_{10}(\text{false discovery rate})$.
683 **d**, Expression of AP-1 TF and BTG family genes that are significantly upregulated upon PCY-hit NAD
684 treatment compared to negative controls (6 hours) plotted as DESeq2 vsd-normalized RNA-Seq counts
685 (y-axis). Box plot groups correspond to drug categories and dots represent the average expression per
686 drug. Drug categories 'PCY-hit NAD' and 'PCY-hit ONCD' abbreviated to NAD and ONCD, respectively.
687 Two-sided t-test. Significant *P*-values in order of appearance per gene: *ATF3*, $P=1.1e-05$, $P=0.039$; *ATF4*,
688 $P=7.8e-08$, $P=0.036$; *FOS*, $P=0.0005$, $P=0.035$; *FOSB*, $P=0.0006$, $P=0.01$; *BTG1*, $P=9.3e-06$; *MAFF*,
689 $P=0.0053$, $P=8.3e-05$; *JUN*, $P=0.0006$, $P=0.023$; *JUNB*, $P=0.0025$; *JUND*, $P=0.0023$, $P=0.0013$. **e**, Calcium
690 response over baseline of LN-229 cells upon drug treatment measured by high-throughput FLIPR assay.
691 (Top) Timeline depicts assay setup, where cells were treated with their respective PCY-drug after
692 equilibration in 2mM calcium-containing buffer. (Bottom) Among 17 tested conditions, representative
693 traces following drug treatment from 8 conditions including 5 antidepressants on the left panel (PCY-
694 hit NADs: VORT/FLUO/PARO; PCY-neg NADs: CITA/MITR), and 2 ONCDs on the right panel (PCY-hit
695 ONCDs, ELES/TEMO). DMSO vehicle control traces shown in both. RFU; relative fluorescence units. **f**,
696 Fold change in extracellular calcium influx upon drug treatment relative to DMSO vehicle control
697 measured by FLIPR assays in LN-229 cells (n=8 assay plates; n=17 conditions; n=18-30 wells/drug;
698 DMSO, n=47 wells). Normalized calcium levels for each drug were calculated by averaging calcium
699 levels after drug treatment (400-600 seconds interval) divided by the basal level of calcium prior to
700 drug administration (200-300 seconds interval) where experimental time corresponds to *Figure 4e*.
701 Different drug categories including PCY-hit NADs, n=8 drugs; PCY-neg NADs, n=6 drugs; PCY-hit ONCDs,
702 n=2 drugs were compared. Two-sided t-test against DMSO vehicle control. *P*-values adjusted for
703 multiple comparisons by Holm correction. *P*-values: VORT, n=27, $P=2.4e-26$; PARO, n=29, $P=9.1e-27$;
704 FLUO, n=30, $P=3.2e-23$; ZOTE, n=30, $P=2.9e-12$; SERT, n=30, $P=6.5e-07$; RIMO, n=30, $P=8.3e-05$; MITR,
705 n=18, $P=3.2e-02$; QUET, n=18, $P=2.2e-03$; TEMO, n=18, $P=2.5e-03$. Asterisks in parentheses denote
706 drug treatment conditions where the median $[\text{Ca}^{2+} \text{ fold change}] < 0$. Black line indicates the median
707 value. **g**, Transcriptional regulation of BTG1/2 based on PathwayNet ⁶⁷. Query genes (*BTG1/2*, black
708 nodes) and the top-13 inferred transcription factor interactions (grey nodes) are shown. Color of
709 network edges indicates relationship confidence (see colorbar). **h**, Correlation of COSTAR signature
710 expression (x-axis) with *ex vivo* patient neuroactive drug response (y-axis) plotted per drug (color) and
711 time-point (shape). Mean glioblastoma PCY score across patients (n=27 patients, prospective cohort)
712 of neuroactive drugs (n=11 PCY-H NADs, n=3 NEGs) plotted against their corresponding geometric
713

714 mean expression of AP-1 TFs and *BTG1/2* genes measured by DRUG-seq as shown in *Figure 4d*. Linear
715 regression line (black) with a 95% confidence interval (light grey). Pearson correlation coefficient
716 $R=0.72$, P -value $1.4e-05$. **i**, Confluency of LN-229 cells measured by IncuCyte live-cell imaging (y-axis)
717 across seven days (x-axis) in two siRNA knockdown conditions (*BTG1*, *BTG2*) and a negative firefly
718 luciferase control (*FLUC*). Mean of $n=4$ replicate wells shown with \pm one standard deviation. **j**, Effect
719 of target gene siRNA knockdown (columns) on LN-229 viability (y-axis) at baseline (DMSO; left panel)
720 and upon Vortioxetine treatment (VORT; $10\mu\text{M}$; right panel). Knockdown of kinesin-like motor protein
721 *KIF11* used as a positive (+) control. Cell count normalized (norm. cell count) to the *FLUC* negative (-)
722 control siRNA within each experiment ($n=9-14$ replicate wells/condition, $n=2$ experiments). Two-sided
723 t-test. P -values adjusted for multiple comparisons by Holm correction. P -values: DMSO; *BTG1* vs *FLUC*,
724 $P=6.99e-05$; *KIF11* vs *FLUC*, $P=3.33e-08$. VORT; *BTG1* vs *FLUC*, $P=0.0008$; *KIF11* vs *FLUC*, $P=0.0006$. **k**,
725 Pathway diagram summarizing mechanistic pathways by which neuroactive drugs target glioblastoma.
726 GRN; gene regulatory network. IEG; immediate early gene. CKI; cyclin-dependent kinase inhibitor. CRE;
727 cAMP response element. FKH; forkhead binding motif. **a,d-f,h**, Colors correspond to drugs and drug
728 name abbreviations annotated in *Supplementary Table 3*. P -values: not significant (ns), $P > 0.05$,
729 $*P < 0.05$, $**P < 0.01$, $***P < 0.001$, $****P < 0.0001$. Boxplots show 25th–75th percentiles with a line
730 at the median; whiskers extend to 1.5 times the interquartile range.

Figure 5



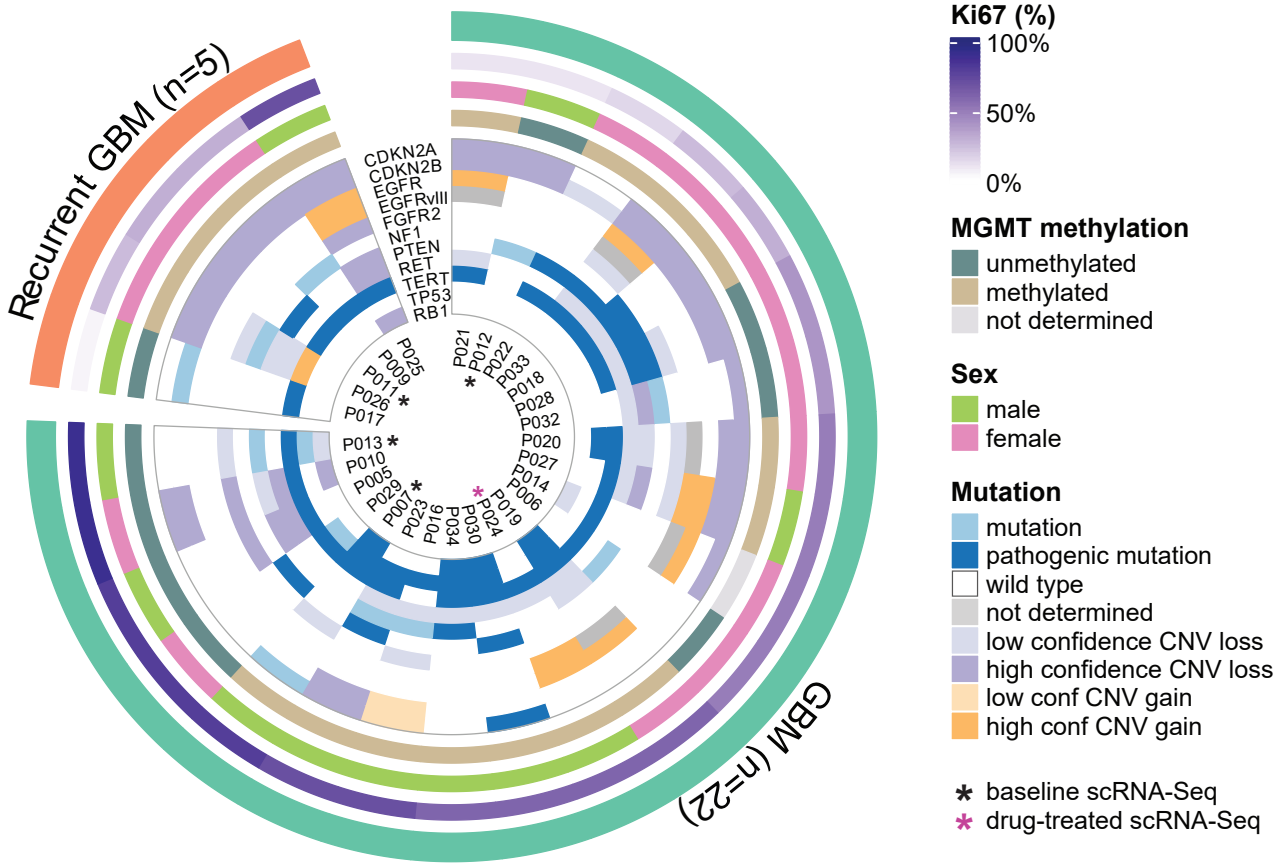
731 **Fig. 5: The antidepressant Vortioxetine induces a potent AP-1 response that**
732 **synergizes *in vivo* with current standard of care drugs for glioblastoma**

733 **a**, Time-course visualization of AP-1 (PID) and MAPK (KEGG) pathway induction following Vortioxetine
734 treatment (20 μ M) in LN-229 cells. Six time-points were measured by RNA-Seq and three time-points
735 by proteomics (n=3 replicates/time-point). Genes selected for visualization are significantly
736 differentially expressed by RNA-Seq at all time-points compared to the first time-point (0h). Heatmap
737 color scale represents log₂(fold change) compared to the 0h time-point. **b**, scRNA-Seq expression
738 log₂(UMI) of selected glioblastoma and top cluster marker genes from glioblastoma patient sample
739 P024. Cluster ids are based upon UMAP clustering of both DMSO and Vortioxetine (VORT, 20 μ M)
740 treated cells (3h) shown in *Extended Data Figure 9a*. Black lines indicate the median value. **c**,
741 Differentially expressed AP-1 transcription factors and downstream effector gene ARC per scRNA-Seq
742 cluster upon VORT treatment compared to DMSO in P024. Circle sizes scale with the $-\log_{10}$ (adjusted
743 *P*-value) and heatmap color scale represents VORT-induced log₂(fold change) compared to DMSO
744 treated cells per cluster. **d**, Induction of AP-1 transcription factors and downstream effector gene
745 *HOMER1* in glioblastoma patient samples (n=3 additional patients; P039, P040, P042) upon
746 Vortioxetine treatment in Nestin+ cells. Immunofluorescence measurements across different time-
747 points (3-6 and 24 h) and different Vortioxetine concentrations (10, 20 μ M). **e**, Representative single-
748 cell image crops from glioblastoma patient P040 of Nestin+ cells stained with different AP-1
749 transcription factors and downstream effector gene *HOMER1* after Vortioxetine treatment (+; 20 μ M)
750 and DMSO vehicle control (-) at 24 hours. Cells are pseudo-colored with DAPI (blue), Nestin (yellow)
751 and AP-1 transcription factors/*HOMER1* (red). Two-sided t-test compared to negative control. Scale
752 bar, 15 μ m. **f**, Survival analysis of Trial I: LN-229 (left) or Trial II: ZH-161 (right) tumor-bearing mice (n=6-
753 7 mice per group). Mice were treated intraperitoneally (*i.p.*) between days 5-21 after tumor
754 implantation with a PCY-HIT NAD, Vortioxetine (VORT; 10mg/kg; Trial I, *P*=0.0001; Trial II, *P*=0.0016), a
755 positive control, Temozolomide (TMZ; 50mg/kg; Trial I, *P*=0.0009 ; Trial II, *P*=0.0002), a PCY-NEG NAD,
756 Paliperidone (PALI; 5mg/kg), and a negative vehicle control. See also *Extended Data Fig. 10a* for Trial
757 III: ZH-161 and full results of *in vivo* Trials I and II including other PCY-hit NADs tested. **g**, Trial IV: *in vivo*
758 treatment of Vortioxetine (VORT; 10mg/kg) in combination with 1st- and 2nd-line glioblastoma
759 chemotherapies; Temozolomide (TMZ; 50mg/kg) and Lomustine (CCNU; 20mg/kg) compared to single-
760 agent treatments and negative vehicle control in ZH-161 tumor-bearing mice (n=5-6 mice per group).
761 Combination treatments, TMZ+VORT/CCNU+VORT, both *P*=0.0007; Single-agents, TMZ/CCNU/VORT,
762 all *P*=0.0018. **f-g**, Survival plotted as Kaplan–Meier curves and *P* values calculated using log-rank
763 (Mantel-Cox) test. Censored mice denoted as tick marks. *P*-values: not significant (ns) *P* > 0.05,
764 **P* < 0.05, ***P* < 0.01, ****P* < 0.001, *****P* < 0.0001.

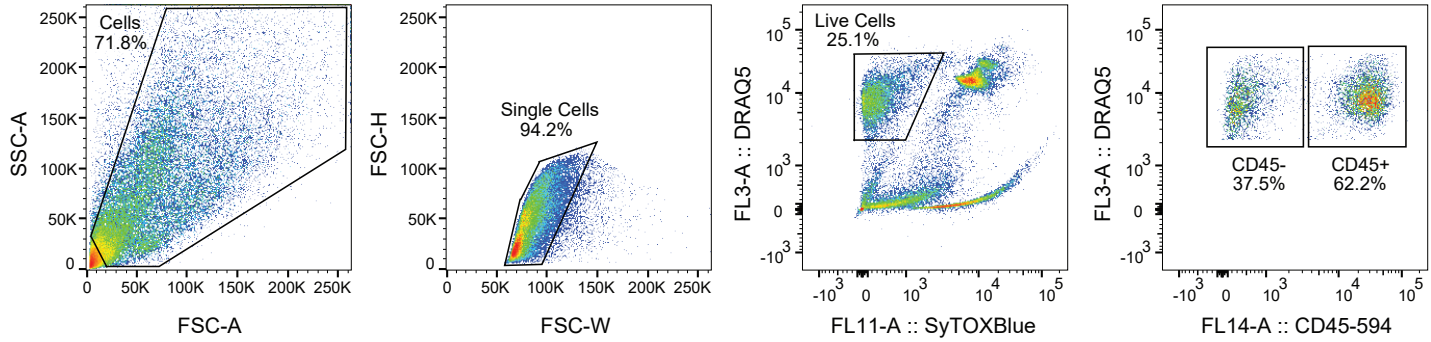
Extended Data Figure 1

a

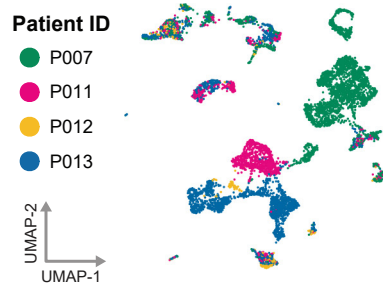
Prospective GBM cohort (n=27 patients)



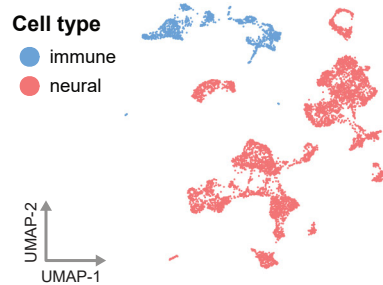
b



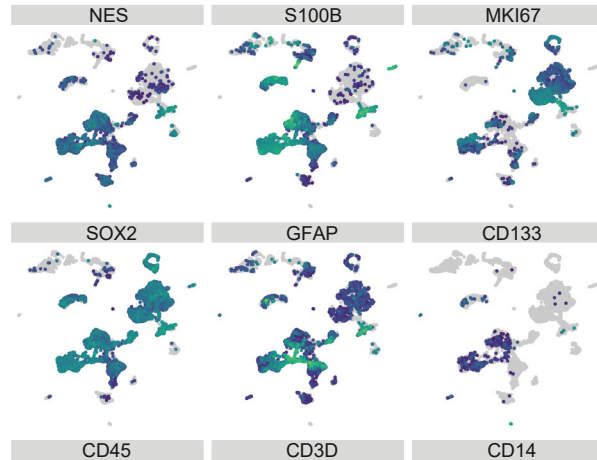
c



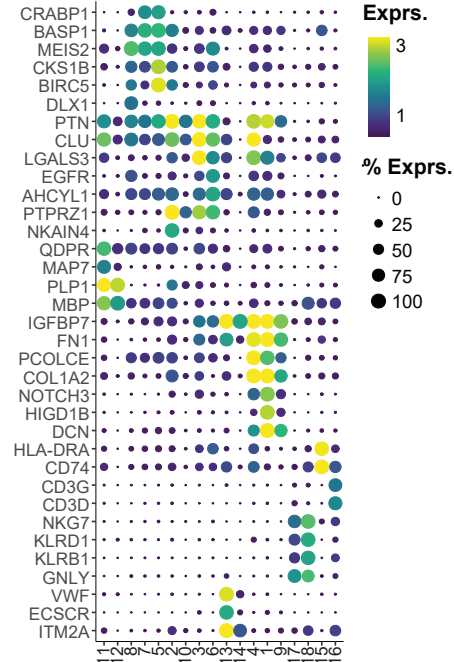
d



e



f



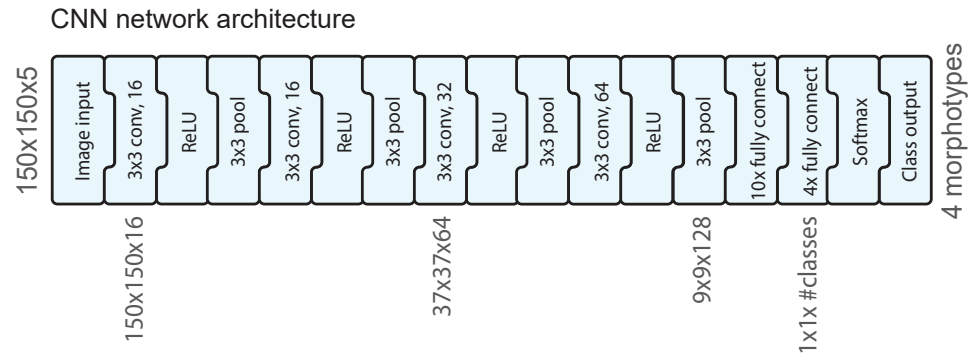
765 Extended Data Figure Legends

766 Extended Data Fig. 1: Glioblastoma prospective cohort overview and single-cell RNA- 767 sequencing of four patient samples

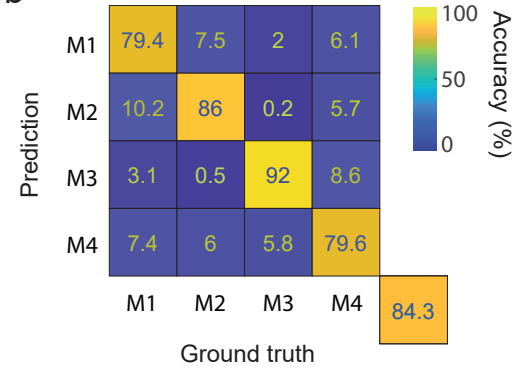
768 **a**, Overview of the glioblastoma prospective patient cohort (n=27 patients) visualized as a circos plot.
769 Concentric circles from outermost to innermost show primary versus recurrent tumor status, Ki67
770 labeling index, sex, *MGMT* promoter methylation status, and the most frequent genetic alterations
771 (n=11) determined by targeted next-generation sequencing (NGS). Asterisks (*) denote patient
772 samples for which scRNA-Seq was also performed (black, n=4 patients at baseline; pink, n=1 patient
773 after drug treatment). CNV; copy number variation. *See Supplementary Table 1,2 for full cohort*
774 *information*. **b**, Representative FACS gates of patient sample P011 to enrich for glioblastoma cells prior
775 to scRNA-Seq (50,000 cells shown). Live viable cells were enriched by first gating DRAQ5+DAPI- cells,
776 then sorting CD45+ and CD45- populations separately. **c**, UMAP projection of 7684 single-cell
777 transcriptomes from four glioblastoma patient samples colored by patient (P007; 3475 cells, P011;
778 1490 cells, P012; 330 cells, P013; 2389 cells). **d**, UMAP projection of 7684 single-cell transcriptomes as
779 in *Figure 1c* colored by cell type lineage. **e**, scRNA-Seq log₁₀(expression) of key glioblastoma and
780 immune marker genes. **f**, Top marker genes per scRNA-Seq cluster in *Figure 1c* that are expressed in
781 more than 10 percent of cells in the respective cluster. Columns correspond to cluster ids and circle
782 sizes scale with the percent of cells within each cluster expressing each gene. Color scale represents
783 log₁₀(mean+0.1) expression.

Extended Data Figure 2

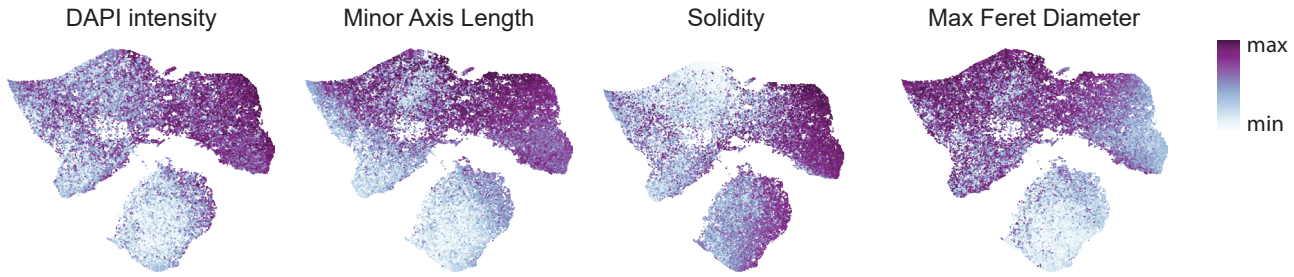
a



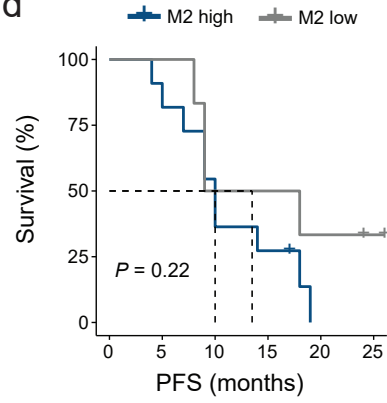
b



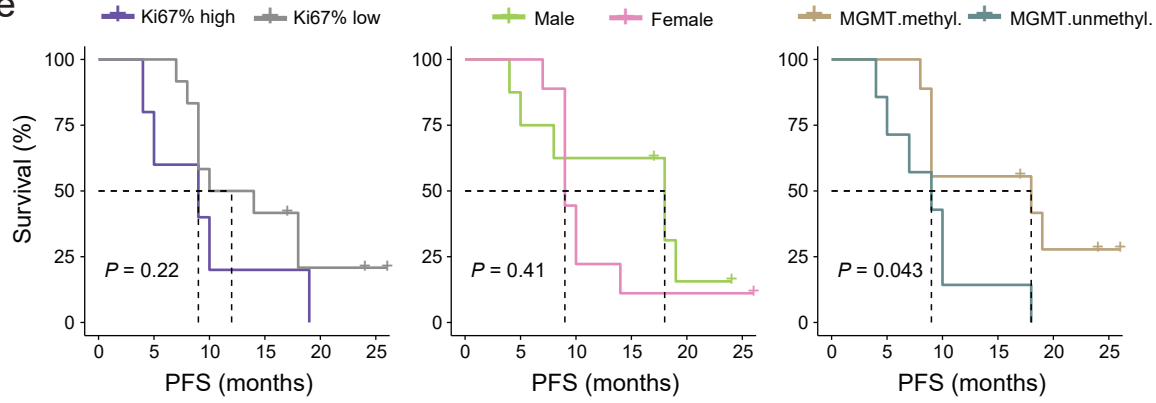
c



d



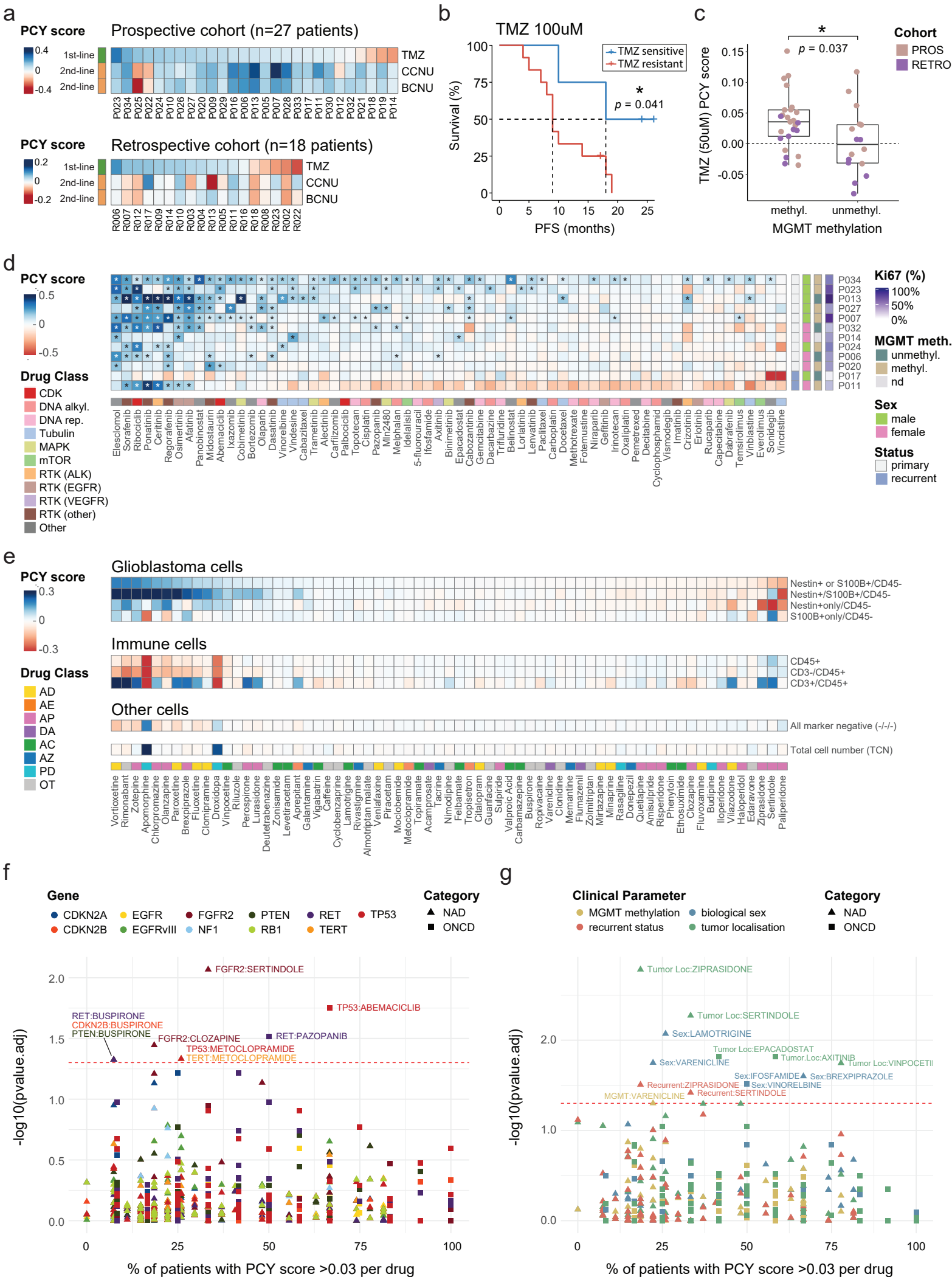
e



784 **Extended Data Fig. 2: Deep learning of glioblastoma stem cell morphologies and**
785 **clinical parameter-based stratification of patient survival**

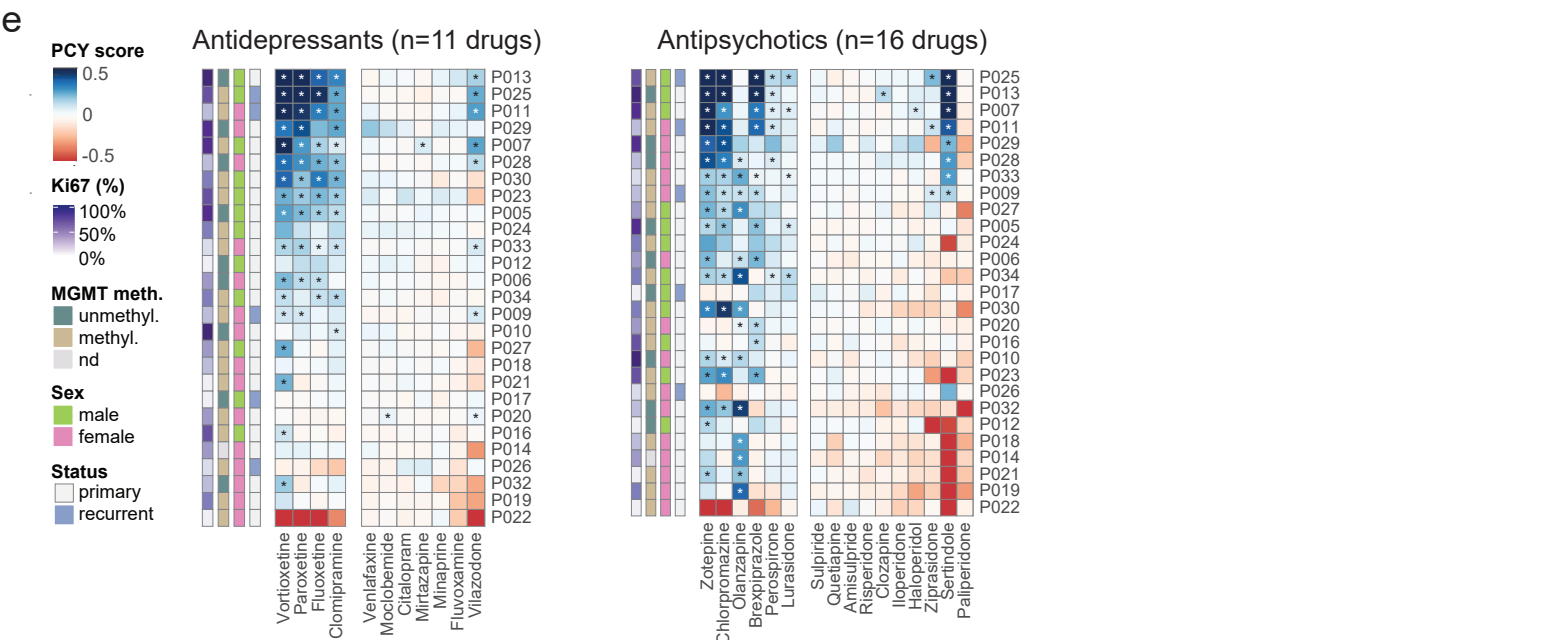
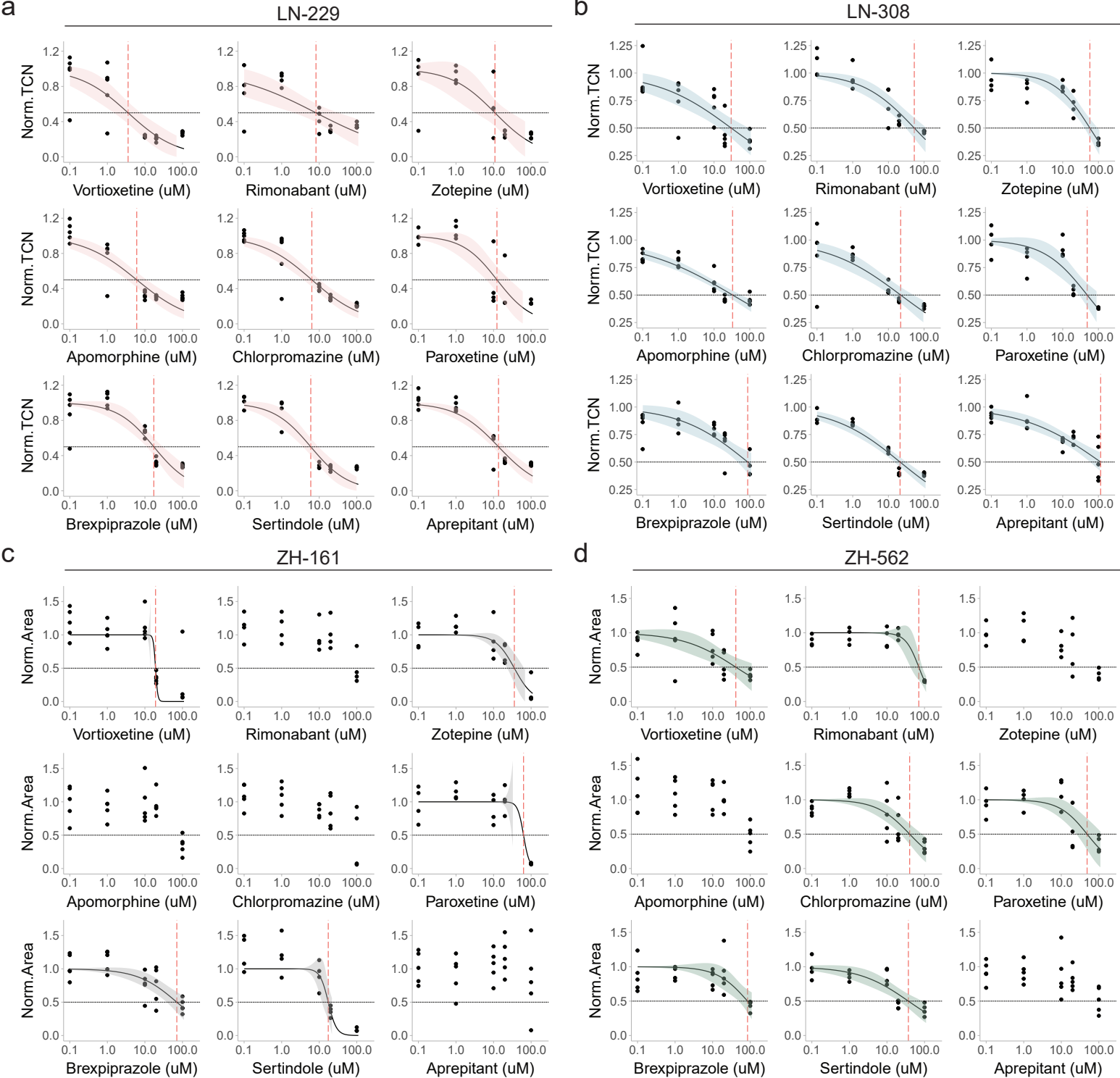
786 **a**, Architecture of the convolutional neural network (CNN) used to train the glioblastoma stem cell
787 (GSC) morphologies, derived from a modified AlexNet⁸⁵. **b**, Performance of the trained GSC
788 morphology CNN in classifying the manually curated test image dataset consisting of Nestin+ single-
789 cell crops (n=10,204 images) into the corresponding four GSC morphotypes (M1-M4). Accuracy of cell
790 classification shown as a confusion matrix. **c**, UMAP projection of the morphological CNN feature space
791 of 84,180 single cells (up to n=1000 cells per morphotype and patient, n=27 patients). CNN feature
792 space consists of ten dimensional activations taken from the 2nd-last fully connected layer of the
793 network. Cells are colored by the local median of selected single-cell features as in *Figure 1g*. **d**,
794 Morphotype (M2) abundance-based stratification of progression-free survival (PFS) in primary
795 glioblastoma patients (n=17 patients) plotted as Kaplan-Meier survival curves. M2-high; n=11, M2-low;
796 n=6 patients; $P=0.22$ (ns). **e**, Clinical parameter-based stratification of progression-free survival (PFS)
797 in primary glioblastoma patients (n=17 patients) plotted as Kaplan-Meier survival curves. From left to
798 right, histopathological Ki67% labeling index, sex, and *MGMT* promoter methylation status (n=1
799 patient with undertermined *MGMT* status omitted). **d-e**, For continuous parameters such as M2
800 morphotype abundance and Ki67%, the optimal cut-point for patient stratification (high, low) is
801 determined by maximally selected rank statistics. Survival curves are compared using the log-rank
802 (Mantel-Cox) test. Censored patients in the prospective cohort indicating ongoing responses (tick
803 marks).

Extended Data Figure 3



804 **Extended Data Fig. 3: Patient *ex vivo* drug response relates to clinical parameters,**
805 **tumor composition, and mutational profiles**

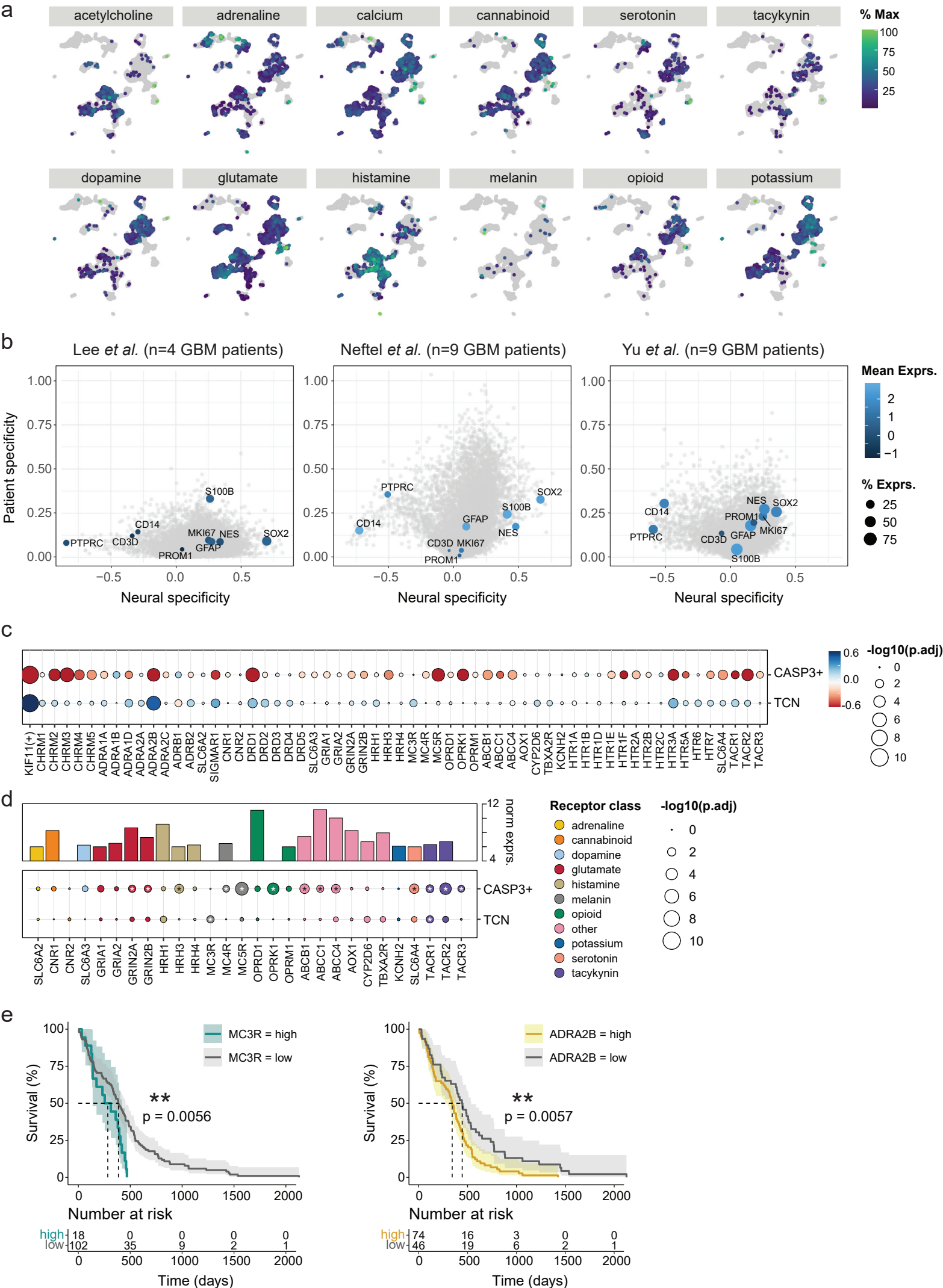
806 **a**, Glioblastoma drug (GSDs; rows; n=3 drugs) response across glioblastoma patient samples (columns;
807 prospective cohort, n=27 patients; retrospective cohort, n=18 patients). Glioblastoma drug response
808 is averaged across four concentrations for Temozolomide (TMZ; 1st-line chemotherapy; 50, 100, 250,
809 500 μ M; annotated green) and Lomustine/Carmustine (Lomustine, CCNU; Carmustine, BCNU; 2nd-line
810 chemotherapies; 10, 50, 100, 250 μ M; annotated orange). Heatmap color scale indicates the PCY score
811 of Nestin+ or S100B+ cells. **b**, Temozolomide (100 μ M) *ex vivo* sensitivity-based stratification of
812 progression-free survival (PFS) in the prospective glioblastoma cohort (n=16 patients; $P=0.041$) plotted
813 as Kaplan-Meier curves. All patients received TMZ as 1st-line treatment in the clinic with censored
814 patients in the prospective cohort indicating ongoing responses (tick marks). Survival curves are
815 compared using the log-rank (Mantel-Cox) test and optimal cut-point for patient stratification
816 determined by maximally selected rank statistics. **c**, Temozolomide (50 μ M) *ex vivo* response of
817 glioblastoma patients (n=41 patients across both cohorts; y-axis) stratified by *MGMT* promoter
818 methylation status. Only patients with an annotated *MGMT* status were included for this analysis.
819 Unmethyl; unmethylated, Methyl; methylated. Wilcoxon rank sum test, $P=0.037$. Boxplots show 25th–
820 75th percentiles with a line at the median; whiskers extend to 1.5 times the interquartile range. Dots
821 indicate individual patient values colored by cohort. **d**, Drug response matrix of oncology drugs
822 (ONCDs; columns; n=65 drugs) across glioblastoma patient samples (rows; n=12 patients). Heatmap
823 color scale indicates the PCY score of glioblastoma cells (Nestin+ or S100B+). Annotations per patient
824 sample (rows; right of heatmap) indicate the clinical parameters Ki67 labeling index, *MGMT* promoter
825 methylation status (unmethyl; unmethylated, methyl; methylated, nd; not determined), Sex, and
826 recurrent tumor status (Status). Annotation per drug (columns; underneath heatmap) indicates
827 oncology drug class as in *Figure 2c*. Asterisks (*) denote FDR-adjusted $P < 0.05$. **e**, Drug response matrix
828 of neuroactive drugs (NADs, n=67 drugs) averaged across glioblastoma patient samples (n=27 patients)
829 for each cell population defined by immunofluorescence markers (Nestin, S100B, CD3, and CD45) and
830 total cell number (TCN). Heatmap color scale indicates the mean PCY score of each respective
831 population and drug classes are annotated as in *Figure 2c*. **f**, Pharmacogenomic analysis of the most
832 common genetic alterations (n=11) in glioblastoma patients and *ex vivo* drug response. Each datapoint
833 represents a [gene:drug] association, where x-axis denotes the percent of patients for which the
834 respective drug's PCY score >0.03 and the y-axis denotes FDR-adjusted P -values for the association. **g**,
835 As in **f**, but for associations between clinical parameters in glioblastoma patients and *ex vivo* drug
836 response. Each datapoint represents a [clinical parameter:drug] association, where x-axis denotes the
837 percent of patients for which the respective drug's PCY score >0.03 and the y-axis denotes FDR-
838 adjusted P -values. **f,g** Colored by gene and shape denote drug category. Red dashed line indicates the
839 significance threshold. Significant associations are annotated. P -values were calculated using the
840 Wilcoxon rank sum test for two groups, and for three or more groups, the Kruskal-Wallis test was used.
841 For ONCD associations, the following genetic mutations or clinical parameters had less than 3 patients
842 in any category and were thus not analyzed: Genetic, *EGFRvIII*, *NF1*, *TERT*, *RB1*; Clinical, Recurrent
843 status. **a,d,e**, Outliers beyond color scale limits were correspondingly set to minimum and maximum
844 values. P -values: * $P < 0.05$.



845 **Extended Data Fig. 4: Dose-response to top neuroactive drugs across glioblastoma**
846 **cell lines and patient *ex vivo* drug response to antidepressants and antipsychotics**

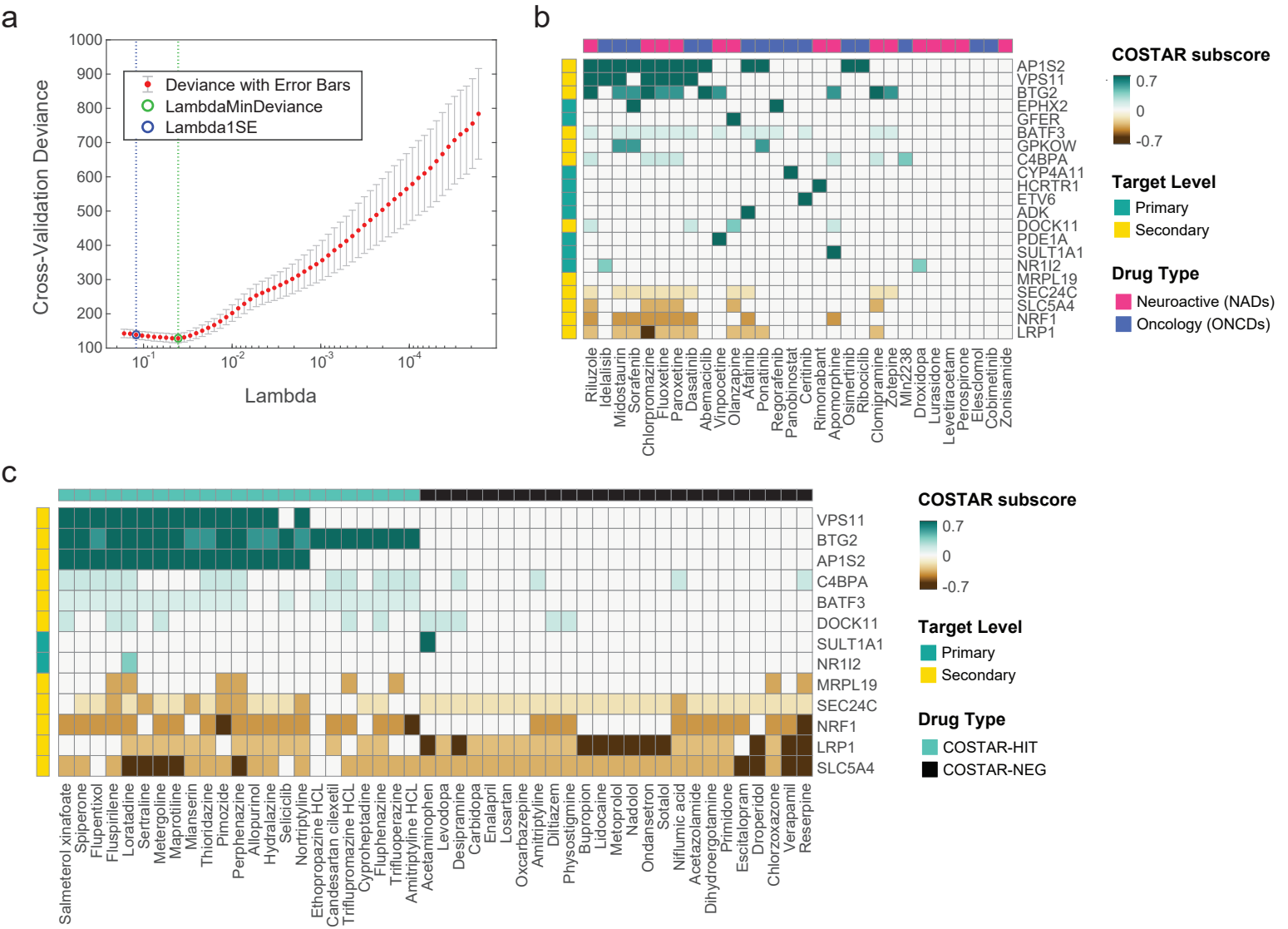
847 **a-d**, Dose-response curves of glioblastoma cell lines (**a**, LN-229; **b**, LN-308; **c**, ZH-161; **d**, ZH-562) of a
848 subset of top neuroactive drugs (n=9 drugs) across five different concentrations. X-axis represents
849 logarithmically spaced drug concentrations while y-axis denotes for **a-b**, Relative cell count normalized
850 to DMSO control and for **c-d**, Relative area of 2D-projected spheroids normalized to DMSO control.
851 Individual well replicates are plotted as black dots (n=3-5 replicate wells/drug, n=15 DMSO wells).
852 Dose-response curves (solid lines) are fitted when possible with a two-parameter log-logistic
853 distribution with 95% confidence intervals (colored per cell line) and ED50 (red vertical dashed lines).
854 **e**, Drug response matrix of antidepressants (left, n=11 drugs) and antipsychotics (right, n=16 drugs)
855 across glioblastoma patient samples (n=27 patients) subsetted from the original matrix shown in *Figure*
856 *2b*. Color scale depicts the PCY score of glioblastoma cells (Nestin+ or S100B+). Outliers beyond color
857 scale limits were correspondingly set to minimum and maximum values. Annotations per patient
858 sample (rows; left of heatmap) indicate the clinical parameters Ki67 labeling index, MGMT promoter
859 methylation status (unmethyl; unmethylated, methyl; methylated, nd; not determined), Sex, and
860 recurrent tumor status (Status). Asterisks (*) denote FDR-adjusted $P < 0.05$.

Extended Data Figure 5



861 **Extended Data Fig. 5: Single-cell heterogeneity and functional dependencies of**
862 **primary neuroactive drug targets**

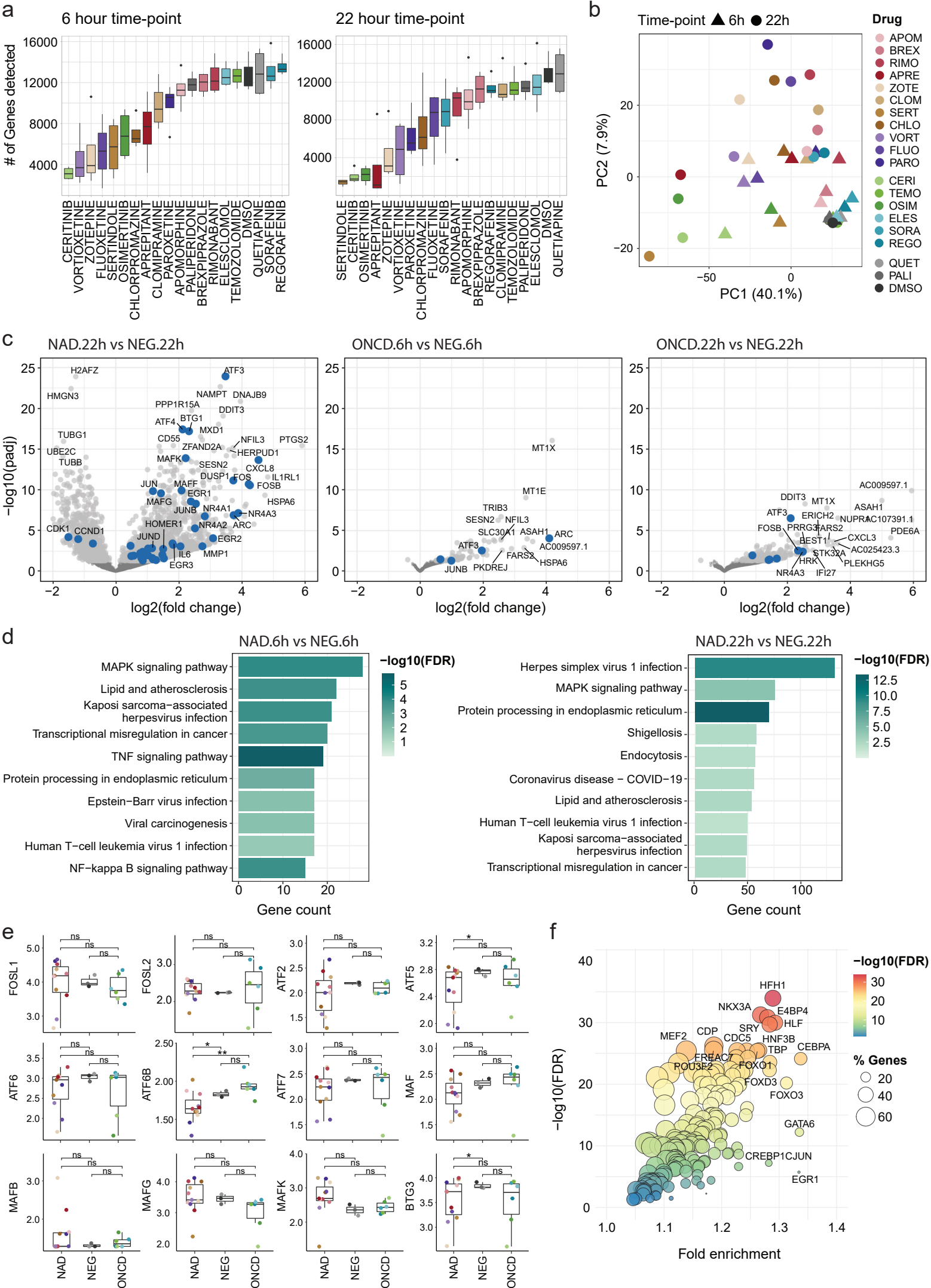
863 **a**, UMAP projection of 7684 single-cell transcriptomes from four glioblastoma patient samples (P007,
864 P011, P012, P013) as in *Figure 1c*, colored by aggregate scRNA-Seq expression across primary target
865 genes (PTG) per receptor class in *Figure 3b*. Color scaled to percent of maximum expression per
866 receptor class. **b**, Neural specificity score (*x*-axis) versus patient specificity score (*y*-axis) for three
867 independent glioblastoma scRNA-Seq datasets. Each dot represents a gene, with key marker genes
868 from *Extended Data Figure 1e* annotated with labels. Key marker gene color represents mean
869 expression across cells in which the gene was detected and dot size scales with percent of expressed
870 cells. All other genes detected in the respective datasets are colored in grey. (Lee *et al.*, *this study*; n=4
871 patients, n=7684 cells, n=15668 genes; Neftel *et al.*, n=9 patients, n=13519 cells, n=22160 genes; Yu *et*
872 *al.*, n=9 patients, n=4307 cells, n=19098 genes; see *Methods* for further detail). **c-d**, siRNA-mediated
873 gene silencing of PTGs in LN-229 cells. Total cell number reduction (TCN) and cleaved CASP3+ fraction
874 increase (CASP3+) depicted as a circle per gene (columns). Circle sizes scale with the $-\log_{10}$ (FDR-
875 adjusted *P* value). **c**, Color represents the PCY score calculated using the FLUC siRNA condition as a
876 negative (-) control reference including all tested PTGs corresponding to *Supplementary Table 5* (n=59
877 siRNA conditions). **d**, Color represents the receptor class of each PTG including PTGs not visualized in
878 *Figure 3d* shown. Asterisks (*) denote FDR-adjusted $P < 0.05$. Adjacent bar plot represents baseline
879 expression (DESeq2 vsd-normalized RNA-Seq counts) of each PTG in LN-229 cells. **e**, Survival analysis
880 and associated risk tables of the TCGA primary glioblastoma cohort (n=120 patients) based on MC3R
881 (left) and ADRA2B (right) expression measured by RNA-Seq. Optimal cut-point for patient stratification
882 (high, low) is determined by maximally selected rank statistics. Survival curves are compared using the
883 log-rank (Mantel-Cox) test. 95% confidence intervals are indicated in shaded curves.



884 **Extended Data Fig. 6: Convergence of secondary drug targets analyzed by regularized**
885 **regression (COSTAR) identifies a drug-target connectivity signature predictive of anti-**
886 **glioblastoma efficacy**

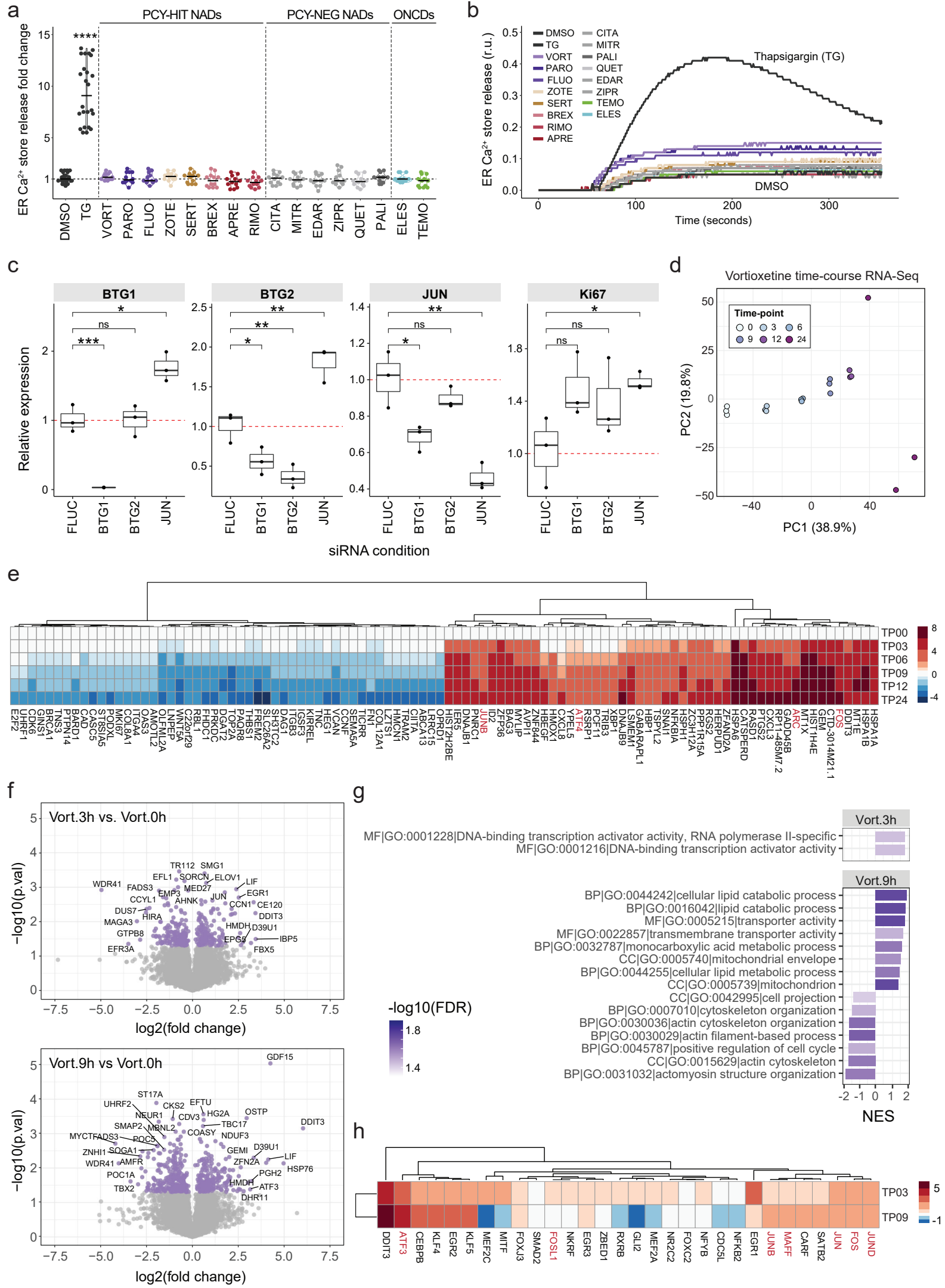
887 **a**, Visualization of the local optimum in the cross-validated predictive power of COSTAR LASSO
888 regression when fitting a binomial model to predict drug activity by PCY (hit vs neg) based on a drugs
889 connectivity pattern (COSTAR constellation). X-axis denotes the Lambda regularization parameter and
890 the y-axis denotes the goodness-of-fit indicating the cross-validated error of the model (deviance). Red
891 dots and light grey error bars indicate the average and standard deviation in deviance across 20
892 bootstrapped runs. Vertical dashed lines and colored circles indicate either the Lambda value with the
893 minimal mean squared error (green, MSE) or the more conservative Lambda value with minimal MSE
894 plus one standard deviation (blue, MSE+1STD). **b**, Heatmap visualizing the COSTAR subscores of PCY-
895 hit drugs that were part of the COSTAR training data (columns; n=30 drugs) to primary and secondary
896 drug targets (rows). Drug type (NAD, ONCD) is annotated above. **c**, COSTAR subscores of COSTAR-
897 predicted drugs that were chosen for experimental validation in glioblastoma patient samples
898 (columns; n=23 COSTAR-HIT drugs; n=25 COSTAR-NEG drugs) to primary and secondary drug targets
899 (rows). Drug type (COSTAR-HIT, COSTAR-NEG) is annotated above. **b-c**, Heatmap color scale indicates
900 the COSTAR subscore which is the LASSO model coefficient multiplied by the integrated connectivity
901 of drug to target mapping. Target genes with COSTAR LASSO coefficients >0.1 are displayed. Target
902 level (primary or secondary target) is annotated per gene on the left.

Extended Data Figure 7



903 **Extended Data Fig. 7: DRUG-Seq reveals a consistent transcriptional response to**
904 **neuroactive drugs with anti-glioblastoma efficacy**

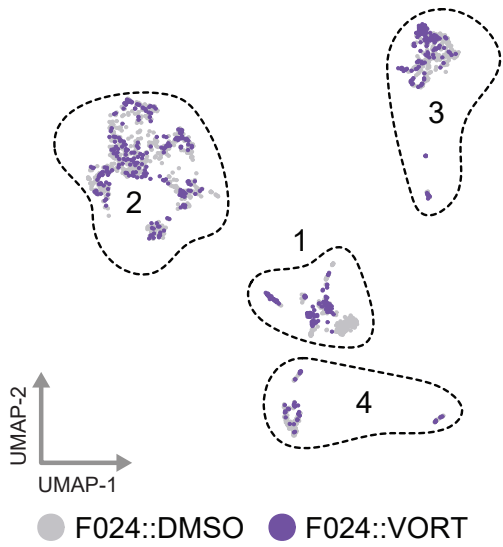
905 **a**, Number of genes detected (y-axis) per drug condition (columns) and by time-point (left and right
906 panel) in the DRUG-Seq data (n=20 drugs, n=2 time-points, n=4 replicates per drug/time-point). **b**,
907 Principal component analysis (PCA) of averaged DESeq2 vsd-normalized RNA-Seq counts per drug.
908 Points are colored by drug and shape indicates time-point. **c**, Comparisons of drug induced
909 transcriptional profiles by DRUG-Seq shown as Volcano plots ($\log_2(\text{fold change})$ versus $-\log_{10}(\text{adjusted}$
910 $P\text{-value})$) for NADs vs NEGs (22h, left), ONCDs vs CTRLs (6h, middle), and ONCDs vs CTRLs (22h, right).
911 Genes above a $-\log_{10}(0.05 \text{ adjusted } P\text{-value})$ threshold plotted as light grey dots, and non-significant
912 genes as dark grey dots. Highlighted genes (blue) include AP-1 transcription factor (TF) network genes
913 (Pathway Interaction Database; PID AP1 PATHWAY; ⁸⁴) and key COSTAR signature genes. **d**, Top
914 enriched KEGG terms for differentially expressed genes based on DESeq2 comparisons of NADs vs
915 NEGs (6h, left) and NADs vs NEGs (22h, right). Bars represent the number of differentially expressed
916 genes present in the annotation, and colors indicate $-\log_{10}(\text{false discovery rate})$. **e**, Expression of AP-
917 1 transcription factor family and BTG genes additional to *Figure 4d*. Visualization and statistical tests
918 as in *Figure 4d*. P -values: not significant (ns) $P > 0.05$, $*P < 0.05$, $**P < 0.01$ **f**, Transcription factor
919 binding site enrichment analysis of genes that were upregulated in NAD treated cells in *Extended Data*
920 *Figure 7c* (22h, left). Circles correspond to transcription factor annotations, circle sizes scale with the
921 fraction of genes present in the annotation, and colors indicate $-\log_{10}(\text{false discovery rate})$. **a,e**
922 Boxplots show 25th–75th percentiles with a line at the median; whiskers extend to 1.5 times the
923 interquartile range.



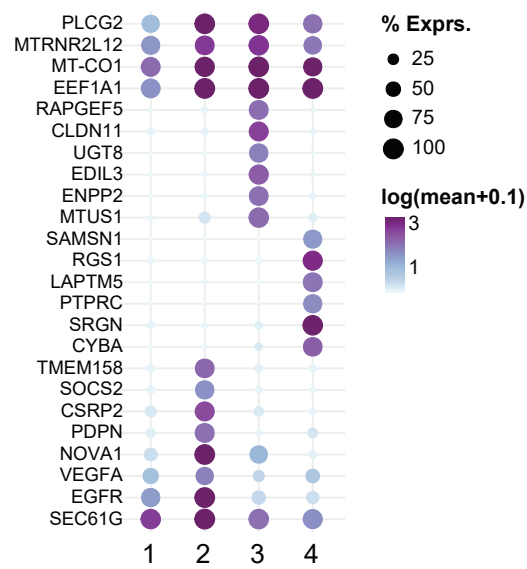
924 **Extended Data Fig. 8: Measuring ER calcium store release, siRNA-mediated silencing**
925 **of COSTAR signature genes, and Vortioxetine-induced transcriptomic and proteomic**
926 **response**

927 **a**, ER calcium store release upon drug treatment relative to DMSO vehicle control (fold change)
928 measured by FLIPR assays in LN-229 cells (n=4 assay plates; n=18 conditions; n=12 wells/drug; DMSO
929 and Thapsigargin, n=24 wells each). Thapsigargin (TG) was used as a positive control that induces ER
930 calcium store depletion. Calcium levels for each condition were calculated by averaging calcium levels
931 after drug treatment (190-430 seconds interval). Different drug categories including PCY-hit NADs, n=8
932 drugs; PCY-neg NADs, n=6 drugs; PCY-hit ONCDs, n=2 drugs; and TG were compared. Two-sided t-test
933 against DMSO vehicle control. *P*-values adjusted for multiple comparisons by Holm correction. *P*-
934 values: TG, 2.86e-16. *****P* < 0.0001. Line indicates the median value. **b**, Representative traces of ER
935 calcium store release following drug treatment corresponding to *Extended Data Figure 8a*. RFU;
936 relative fluorescence units. **c**, Relative gene expression (*y*-axis) of BTG1, BTG2, JUN and Ki67 (panels)
937 upon siRNA knockdown of FLUC, BTG1, BTG2, and JUN (columns) normalized to the FLUC negative
938 control siRNA (n=3 biological replicates; black dots). Boxplots show 25th–75th percentiles with a line
939 at the median; whiskers extend to 1.5 times the interquartile range. **d**, Principal component analysis
940 (PCA) of averaged DESeq2 vsd-normalized RNA-Seq counts following Vortioxetine treatment (20μM)
941 in LN-229 cells (n=3 replicates/time-point). Points are colored by time-point. **e**, Heatmap of log₂(fold
942 change) in gene expression per time-point (rows; relative to 0h) for the top 100 genes (columns)
943 contributing to the first principal component (PC1) in *Extended Data Figure 8d*. TP; time-point. AP-1
944 transcription factors and AP-1 effector genes are labeled in red. **f**, Volcano plots of log₂(fold change)
945 versus $-\log_{10}(P\text{-value})$ corresponding to 3 hours versus 0 hours (top; Vort.3h vs. Vort.0h) and 9 hours
946 versus 0 hours (bottom; Vort.9h vs. Vort.0h) comparisons of proteomics measurements following
947 Vortioxetine treatment (Vort, 20μM; n=3 biological replicates/condition) in LN-229 cells. Plotted are
948 proteins above a $-\log_{10}(0.05 P\text{-value})$ threshold (purple), and non-significant proteins (grey). Select
949 gene names are shown. **g**, Gene Ontology (GO) gene set enrichment analysis of signed $-\log_{10}(P\text{-values})$
950 of both time-point comparisons from *Extended Data Figure 8f*. Bars represent the normalized
951 enrichment score (NES) and colors indicate $-\log_{10}(\text{false discovery rate})$. **h**, Heatmap depicting
952 log₂(fold change) in protein expression per time-point (rows; relative to 0h) for the proteins (columns)
953 contributing to enriched GO term “GO:0001216 DNA-binding transcription activator activity” in
954 *Extended Data Figure 8g*. TP; time-point. AP-1 transcription factors are labeled in red.

a

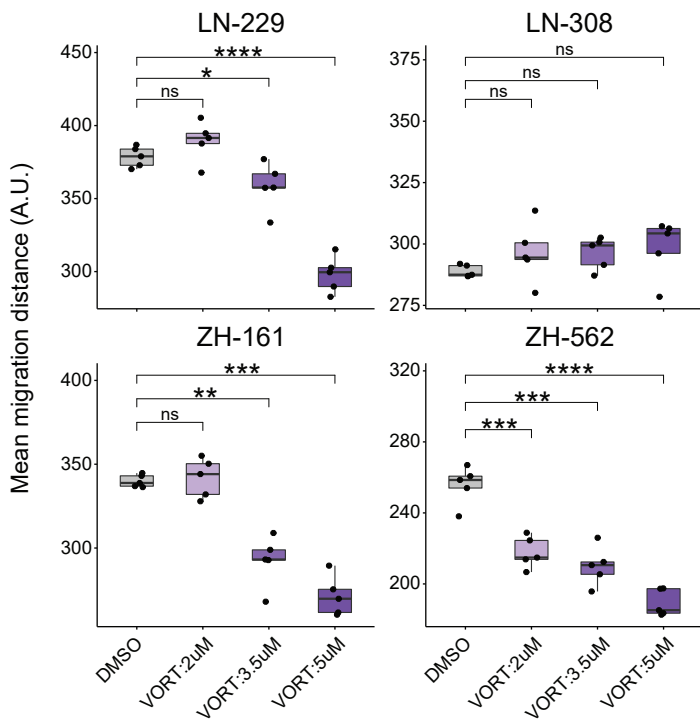


b



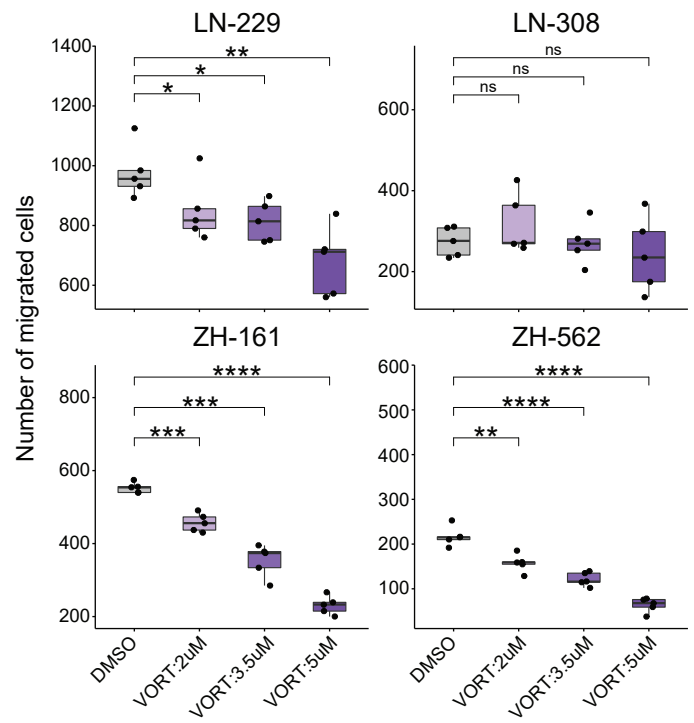
c

Collagen invasion assay (distance)



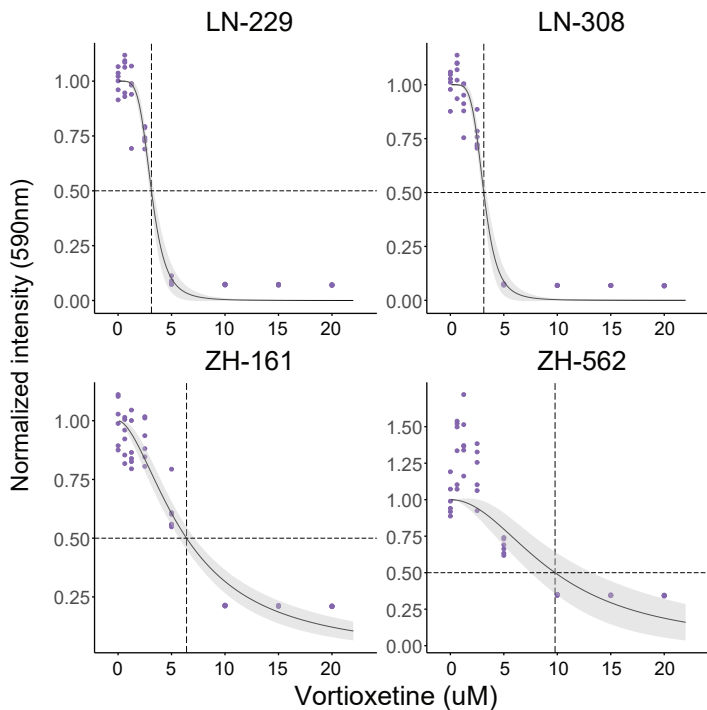
d

Collagen invasion assay (# of cells)



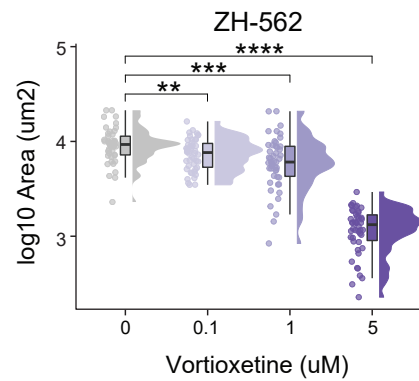
e

Clonogenic survival assay



f

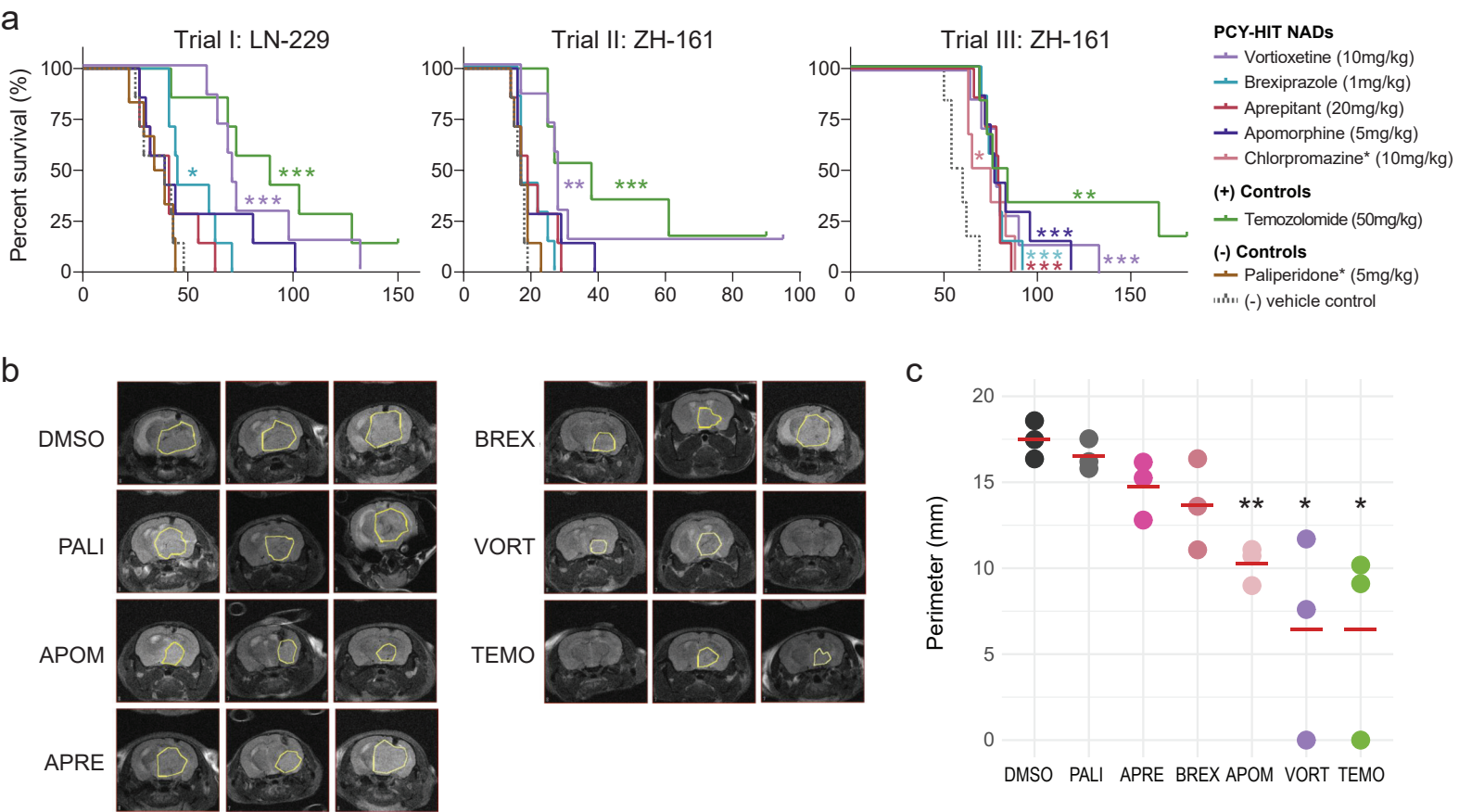
Spheroid formation assay



955 **Extended Data Fig. 9: Single-cell RNA-sequencing of Vortioxetine-treated patient**
956 **cells and the multi-faceted anti-glioblastoma effects of Vortioxetine**

957 **a**, UMAP projection of 1736 single cells from glioblastoma patient sample P024 upon 3 hours of
958 treatment with Vortioxetine (P024::VORT; n=577 cells; purple; 20 μ M) or DMSO vehicle control
959 (P024::DMSO; n=1159 cells; grey). **b**, Expression levels of the top six marker genes per scRNA-Seq
960 cluster in *Extended Data Figure 9a* that are expressed in more than 10% of cells in the respective
961 cluster. Columns correspond to cluster ids and circle sizes scale with the percent of cells within each
962 cluster expressing each gene. Color scale represents $\log_{10}(\text{mean}+0.1)$ expression. **c**, Mean cell
963 migration distance per condition (n=5 replicate wells) and **d**, number of migrated cells measured in a
964 collagen-based spheroid invasion assay after 36 hours of Vortioxetine treatment (2, 3.5, 5 μ M) across
965 four glioblastoma cell lines; LN-229 (n=560-1125 cells/well), LN-308 (n=137-426 cells/well), ZH-161
966 (n=200-574 cells/well), ZH-562 (n=38-253 cells/well). **e**, Clonogenic survival measured by a resazurin-
967 based cell viability assay after 11-13 days of Vortioxetine treatment (7 concentrations; 0.625-20 μ M)
968 across four glioblastoma cell lines; LN-229 LN-308, ZH-161, ZH-562. Cells were seeded in 96-well plates
969 (50-500 cells/well) and normalized intensity (λ Em = 590 nm) measured across six replicate
970 wells/concentration. Dose-response fitted with a two-parameter log-logistic distribution with 95%
971 confidence intervals (light grey) and ED50 (dashed lines). **g**, Spheroid formation analyzed by the 2D
972 area of the ZH-562 line measured after 12 days of Vortioxetine treatment (0.1-5 μ M). Approximately 5
973 cells/well initially seeded in low-attachment U-bottom 384-well plates. DMSO; 0 μ M, n=45 replicate
974 wells; 0.1 μ M, n=46, $P=0.005$; 1 μ M, n=47, $P=0.00027$; 5 μ M, n=46, $P<0.0001$. Data is shown per
975 concentration as boxplot, individual data points, and histogram.

Extended Data Figure 10



976 **Extended Data Fig. 10: Top neuroactive drugs confer a significant survival benefit in**
977 **orthotopic *in vivo* mouse models of glioblastoma**

978 **a**, Complete survival analysis across three independent *in vivo* trials: Trial I: LN-229, Trial II: ZH-161,
979 and Trial III: ZH-161, each with n=6-7 tumor-bearing mice per drug treatment group and n=7 drug
980 treatments per trial. Mice were treated with their respective drugs for each trial intraperitoneally (*i.p.*)
981 between days 5-21 after tumor implantation. PCY-HIT NADs: Vortioxetine (VORT; 10mg/kg; Trial I,
982 $P=0.0001$; Trial II, $P=0.0016$; Trial III, $P=0.0006$); Brexpiprazole (BREX; 1mg/kg; Trial I, $P=0.0249$; Trial II,
983 ns; Trial III, $P=0.0002$); Aprepitant (APRE; 20mg/kg; Trial I, ns; Trial II, ns; Trial III, $P=0.0006$);
984 Apomorphine (APOM; 5mg/kg; Trial I, ns; Trial II, ns; Trial III, $P=0.0005$); Chlorpromazine (CHLO;
985 10mg/kg; Trial III, $P=0.011$). Positive control (+): Temozolomide (TMZ; 50mg/kg; Trial I, $P=0.0009$; Trial
986 II, $P=0.0002$; Trial III, $P=0.0011$). PCY-NEG NAD: Paliperidone (PALI; 5mg/kg; Trial I, ns; Trial II, ns), and
987 a negative vehicle control. Drug names with asterisk (*) denote drugs used in a subset of the three *in*
988 *in vivo* trials. Survival plotted as Kaplan–Meier curves and P -values calculated using log-rank (Mantel-
989 Cox) test. Censored mice denoted as tick marks. **b**, Representative MRI images of three ZH-161
990 transplanted mice (columns) after 15 days per drug treatment (n=7 drugs). Tumor perimeters are
991 indicated in yellow. **c**, Quantification of tumor perimeters corresponding to *Extended Data Figure 10b*.
992 Dots represent the perimeter in mm (y-axis) for individual mice per drug (columns), red lines indicate
993 mean value. Two-sided t-test. P -values: Apomorphine (APOM; $P=0.0014$); Vortioxetine (VORT;
994 $P=0.034$); Temozolomide (TMZ; $P=0.0284$). P -values: not significant (ns) $P > 0.05$, * $P < 0.05$, ** $P < 0.01$,
995 *** $P < 0.001$, **** $P < 0.0001$.

996 **Methods**

997 **Patient sample processing and drug testing**

998 Surgically removed tumors were collected at the University Hospital of Zurich (Universitätsspital
999 Zürich, USZ) with approval by the Institutional Review Board, ethical approval number KEK-StV-
1000 Nr.19/08, BASEC number 2008-02002. Metadata of the prospective and retrospective glioblastoma
1001 patient cohorts including clinical parameters, experiment inclusion, and genetics summary can be
1002 found in *Supplementary Table 1*. The prospective cohort consists of patients where fresh tissue was
1003 taken directly after surgery (n=27 patients for drug screening, plus an additional n=3 patients for
1004 validation experiments). The retrospective cohort (n=18 patients) consists of patients for which snap-
1005 frozen bio-banked tissue was available covering a broad spectrum of progression-free survival.
1006 Retrospective samples were further selected based on quality control measures including cell viability,
1007 cell number, and the amount of debris present in the sample.

1008 Tissue samples were first washed with PBS and cut into small pieces using single-use sterile scalpels.
1009 Subsequent dissociation was performed in reduced serum media (DMEM media; #41966029 with 2%
1010 FBS; #10270106, 1% Pen-strep; #15140122, and 25mM HEPES; #15630056, all products from Gibco)
1011 supplemented with Collagenase IV (1mg/ml) and DNaseI (0.1mg/ml) using the gentle MACS Octo
1012 Dissociator (Miltenyi Biotec, 130-096-427). Homogenates were filtered through a 70um Corning cell
1013 strainer (Sigma-Aldrich, CLS431751) and washed once with PBS containing 2mM EDTA. Myelin and
1014 debris removal was performed by a gradient centrifugation of the cell suspension in a 7:3 mix of
1015 PBS:Percoll (Sigma-Aldrich, P4937) and washed again with PBS. Dissociated patient cells were seeded
1016 at $0.5-1.5 \times 10^4$ cells/well into clear-bottom, tissue-culture treated, CellCarrier-384 Ultra Microplates
1017 (Perkin Elmer, #6057300). Prior to cell seeding, tested drugs were re-suspended as 5mM stock
1018 solutions and dispensed into the 384 well plates using an Echo 550 liquid handler (Labcyte) at their
1019 respective concentrations in a randomized plate layout to control for plate effects. Information
1020 regarding drugs used in this study can be found in *Supplementary Table 3*. For drug library testing
1021 (glioblastoma drugs, GSDs; neuroactive drugs, NADs; oncology drugs, ONCDs) cells were incubated in
1022 reduced serum media at 37°C, 5% CO₂ for 48 hours with drugs.

1023 **Targeted Next Generation Sequencing (NGS, OncoPrint Comprehensive Assay v3)**

1024 Tissue blocks from patient-matched glioblastomas were used to determine genetic alterations
1025 including mutations, copy number variation and gene fusion. Formalin-fixed paraffin-embedded (FFPE)
1026 tissue blocks were collected from the Tissue Biobank at USZ archives. Tumor area was marked on the
1027 HE slide and relative tumor cell content was estimated by a trained pathologist. 1-3 cores cylinders
1028 (0.6 mm diameter) or 40 um from the tumor area of the FFPE blocks were used for DNA and RNA
1029 isolation. DNA was isolated with the Maxwell 16 FFPE Tissue LEV DNA Purification Kit (Promega,
1030 #AS1130) according to the manufacturer's recommendations. The double-strand DNA concentration
1031 (dsDNA) was determined using the fluorescence-based Qubit dsDNA HS Assay Kit. RNA was extracted
1032 with the Maxwell 16 FFPE Tissue LEV RNA Purification Kit (Promega, #AS1260) according to the
1033 manufacturer's recommendations. To avoid genomic DNA contamination, samples were pretreated
1034 with DNase1 for 15 min at room temperature (RT). Library preparation with 20 ng DNA or RNA input
1035 was conducted using the OncoPrint Comprehensive Assay v3 following the manufacturer's
1036 instructions. Adaptor/barcode ligation, purification and equilibration was automated with Tecan Liquid
1037 Handler (EVO-100). NGS libraries were templated using Ion Chef and sequenced on a S5 (Thermo Fisher

1038 Scientific), and data were analyzed using Ion Reporter Software 5.14 with Applied Filter Chain:
1039 Oncomine Variants (5.14) settings and Annotation Set :Oncomine Comprehensive Assay v3
1040 Annotations v1.4.

1041 For NGS data analysis, the Ion Reporter Software within Torrent Suite Software was used, enabling
1042 detection of small nucleic variants (SNVs), copy number variations (CNVs), gene fusions and indels from
1043 161 unique cancer driver genes. Detected sequence variants were evaluated for their pathogenicity
1044 based on previous literature and the 'ClinVar' database ⁸⁶. Gene alterations described as benign or
1045 likely benign were not included in our results. Non-pathogenic mutations harboring a Minor Allele
1046 Frequency higher than 0.01 were not selected. The Default Fusion View parameter was selected. For
1047 CNV confidence range, the default filter was used to detect gains and losses using the confidence
1048 interval values of 5% confidence interval for Minimum Ploidy Gain over the expected value and 95%
1049 confidence interval for Minimum Ploidy Loss under the expected value. CNV low confidence range was
1050 defined for gain by copy number from 4 to 6 (lowest value observed for CNV confidence interval
1051 5%:2.9) and loss from 0.5 to 1 (highest value observed for CNV confidence interval 95%:2.43). High
1052 confidence range was defined by gain up to 6 copy number (lowest value observed for CNV confidence
1053 interval 5%:4.54) and loss below 0.5 copy number (highest value observed for CNV confidence interval
1054 95%:1.37). 5% and 95% interval confidence of all selected loss and gain are available in *Supplementary*
1055 *Table 2*. The minimum number of tiles required was eight. Results are reported as detected copy
1056 number.

1057 **Cell culture**

1058 The adherent human glioblastoma cell lines LN-229 (ATCC, #CRL-2611) and LN-308 were cultured in
1059 Dulbecco's modified Eagle medium (DMEM, #41966, Gibco) supplemented with 10% fetal bovine
1060 serum (FBS, #10270106, Gibco). LN-229 and LN-308 cells were passaged using Trypsin-EDTA (0.25%,
1061 Gibco, #25200056). For DRUG-seq, RNA-Seq, siRNA knockdown, and proteomics measurements using
1062 LN-229 cells, low-passage cells below passage 15 were used. The spheroid human glioblastoma-
1063 initiating cell lines ZH-161 and ZH-562 was generated from freshly isolated tumor tissue and cultured
1064 in Neurobasal medium (NB, #21103049, Gibco) supplemented with B27 (Gibco, #17504044), 20 ng/mL
1065 b-FGF (Peprotech, #AF-100-18B), 20 ng/mL EGF (Peprotech, #AF-100-15), 2 mM L-glutamine (Gibco,
1066 #25030081). ZH-161 and ZH-562 cells were passaged using Accutase (Stemcell Technologies, #07920).
1067 Cell lines were authenticated at the Leibniz Institute DSMZ (Braunschweig, Germany) and regularly
1068 tested negative for mycoplasma.

1069 **Immunocytochemistry**

1070 Cells were fixed with 4% PFA (Sigma-Aldrich, #F8775) in PBS and blocked in 5% FBS and 0.1% Triton
1071 containing PBS. For characterization of cellular composition across glioblastoma patient samples, cells
1072 were stained overnight at 4°C in blocking solution with the following antibodies and dilutions: Alexa
1073 Fluor® 488 anti-S100 beta (1:1000, Abcam, #ab196442, clone EP1576Y), PE anti-Nestin (1:150,
1074 Biolegend, #656806, clone 10C2), Alexa Fluor® 488 anti-CD3 (1:300, Biolegend, #300415, clone
1075 UCHT1), Alexa Fluor® 647 anti-CD45 (1:300, Biolegend, #368538, clone 2D1) and DAPI (1:1000,
1076 Biolegend, #422801, stock solution 10mg/ml). Due to the manufacturer discontinuation of the Alexa
1077 Fluor® 488 anti-S100 beta antibody, from patient sample P30 and onwards in the prospective cohort,
1078 samples were either stained with a self-conjugated Alexa Fluor® 488 anti-S100 beta antibody, where
1079 Alexa Fluor™ 488 NHS Ester (Thermo Scientific, #A20000) was conjugated to the anti-S100 beta
1080 antibody (Abcam, #ab215989, clone EP1576Y) or the following antibody combinations where the 488

1081 and 555 channel markers were swapped: Alexa Fluor® 488 anti-Nestin (1:150, Biolegend, #656812,
1082 clone 10C2), Alexa Fluor® 555 anti-S100 beta (1:1000, Abcam, #ab274881, clone EP1576Y), PE anti-CD3
1083 (1:300, Biolegend, #300441, clone UCHT1), Alexa Fluor® 647 anti-CD45 (1:300, Biolegend, #368538,
1084 clone 2D1).

1085 Other antibodies used in this study include the following: Alexa Fluor® 647 anti-Tubulin Beta 3 (1:1000,
1086 Biolegend, #657406, clone AA10), Alexa Fluor® 555 anti-Cleaved Caspase-3 (1:500, Cell Signaling
1087 Technology, #9604S), Alexa Fluor® 546 anti-HOMER (1:300, Santa Cruz Biotechnology, #sc-17842
1088 AF546, clone D-3), PE anti-CFOS (1:300, Cell Signaling Technology, #14609S, clone 9F6), FITC anti-ATF4
1089 (1:300, Abcam, #ab225332), Alexa Fluor® 488 anti-JUND (1:300, Santa Cruz Biotechnology, #sc-271938
1090 AF488, clone D-9), Alexa Fluor® 594 anti-CD45 (1:300, Biolegend, #368520, clone 2D1).

1091 **Confocal microscopy and image analysis**

1092 Imaging of the 384 well plates was performed with an Opera Phenix automated spinning-disk confocal
1093 microscope at 20x magnification unless otherwise specified (Perkin Elmer, HH14000000). Single cells
1094 were segmented based on their nuclei (DAPI channel) using CellProfiler 2.2.0. Downstream image
1095 analysis was performed with MATLAB R2019a-R2020a. Fractions of marker positive cells for each
1096 condition were derived for each patient sample based on the histograms of the local background
1097 corrected intensity measurements. Marker positive fractions were averaged across each
1098 well/condition and compared to the negative DMSO control.

1099 **Deep learning of glioblastoma stem cell morphologies**

1100 To generate a training dataset, Nestin+CD45- cells identified by immunofluorescence across the whole
1101 prospective glioblastoma patient cohort were cropped as 150x150 pixel images. These single-cell
1102 image crops were then manually-curated and labeled as four morphological classes (M1-M4
1103 morphotypes) based on their shape, size, and presence of tumor microtubes. A convolution neural
1104 network (CNN) with a modified Alexnet architecture⁸⁵ as shown in *Extended Data Figure 2a* was then
1105 trained on this manually-curated training data with 12,757 images per class and 51,028 images in total.
1106 CNN training included usage of the Adam optimizer, with a mini-batch size of 150 and a maximum
1107 number of 30 epochs. The initial learning rate was set to 0.001 with a piecewise learning rate schedule
1108 and a drop factor of 0.01 every 6 epochs.

1109 Network performance is shown as a confusion matrix in *Extended Data Figure 2b*. All Nestin+ single-
1110 cell images were subsequently classified by this pre-trained CNN to determine morphotype
1111 abundances across patients and drug conditions. For visualization of the CNN-based GSC morphotypes,
1112 UMAP plots were generated based on the CNN feature space that consists of ten dimensional
1113 activations taken from the 2nd-last fully connected layer of the network. The CNN feature space of
1114 84,180 cells (maximally 1000 cells per class and patient, n=27 patients) was projected on the UMAP
1115 using the following parameters: distance metric, seucclidean; number of neighbors, 10; minimal
1116 distance, 0.06. Different morphological and marker-based features from the original cell segmentation
1117 determined by CellProfiler 2.2.0 such as cell area, eccentricity, and roundness, and mean marker
1118 intensity were selected for visualization.

1119 **siRNA knockdown and quantitative real-time PCR**

1120 All siRNAs used in the study were part of the MISSION® esiRNA (Sigma-Aldrich, Euphoria Biotech)
1121 library (*Supplementary Table 5*) and ordered as custom gene arrays (esiOPEN, esiFLEX). FLUC esiRNA

1122 (EHUFLUC) targeting firefly Luciferase was used as a negative control, and KIF11 esiRNA (EHU019931)
1123 was used as a positive control for transfection and viability. For all siRNA experiments, low-passage LN-
1124 229 cells were used. siRNAs were transfected at 10ng/well in 384 well plates and 40ng/well in 96 well
1125 plates using Lipofectamine RNAiMAX (Invitrogen, #13778075). Imaging and drug incubation
1126 experiments were conducted in 384 well plates, while Incucyte live cell imaging and cell lysis
1127 preparation for RNA extraction and quantitative real-time PCR was performed in 96 well plates. For
1128 384 well plates, both the siRNAs and Lipofectamine transfection reagent were dispensed using a
1129 Labcyte Echo liquid handler in a randomized plate layout to control for plate effects when possible. For
1130 data presented in *Figure 3d*, *Extended Data Figure 5c,d*, and *Extended Data Figure 8c*, cells were
1131 incubated at 37°C, 5% CO₂ for 48 hours following siRNA transfection before fixing,
1132 immunohistochemistry, and RNA extraction. For data presented in *Figure 4j*, following 48 hours of
1133 siRNA transfection, cells were incubated for an additional 24 hours with either DMSO vehicle control
1134 or Vortioxetine (10μM) before fixing and subsequent analysis.

1135 siRNA knockdown efficiency and relative abundance for the following target genes; BTG1, BTG2, JUN,
1136 and MKI67 was measured by TaqMan™ Array plates (Applied Biosystems, Standard, 96-well Plate;
1137 Format 16 with candidate endogenous controls) using the TaqMan™ Fast Advanced Master Mix
1138 (Thermo Scientific, #A44360) on a QuantStudio™ 3 Real-Time PCR System (Applied Biosystems,
1139 #A28567). Total RNA from LN-229 cells was extracted using the Direct-zol RNA MicroPrep Kit (Zymo
1140 Research, #R2062), RNA concentration was measured using the Qubit 4 Fluorometer (Thermo
1141 Scientific), and cDNA synthesized with the iScript™ cDNA Synthesis Kit (Bio-Rad, #1708890). For each
1142 TaqMan biological replicate assay (n=3 replicates) 25ng of cDNA per sample was used. To calculate the
1143 relative abundance of each target gene, the geometric mean Ct value of four endogenous control
1144 genes (18s rRNA, GAPDH, HPRT, GUSB) was subtracted from each [sample-target gene] Ct value to
1145 derive the deltaCt (dCt) value. Then, the mean deltaCt value from FLUC negative control samples was
1146 subtracted from each [sample-target gene] deltaCt value to derive the delta-deltaCt (ddCt) value.
1147 Finally, relative abundance (fold-difference) of each [sample-target gene] was calculated as the 2^{^(-}
1148 ddCt).

1149 **COSTAR: Convergence of secondary drug-targets analyzed by regularized regression**

1150 COSTAR is an interpretable molecular machine learning approach that utilizes logistic LASSO regression
1151 in a cross-validation setting to learn a multi-linear model that identifies the minimal set of drug-target
1152 connections that maximally discriminates PCY-hit drugs from PCY-negative drugs.

1153 Drug-target connections were retrieved from the Drug Target Commons (DTC) ⁵². DTC is a crowd-
1154 sourced platform that integrates drug-target bioactivities curated from both literature and public
1155 databases such as PubChem and ChEMBL. Drug-target annotations (DTC bioactivities) listed as of
1156 August 2020 were included, with the target organism limited to *Homo sapiens*. Among PCY-tested
1157 drugs in our NAD and ONCD libraries, 127 out of 132 drugs had DTC 'bioactivity' annotations. PTGs
1158 with biochemical associations to a given drug correspond to bioactivities with the inhibitory constant
1159 'KI' as the 'End Point Standard Type'. Extended PTGs (ePTGs) include all annotated drug bioactivities.
1160 Secondary target genes (STGs) down-stream of ePTGs were retrieved by high-confidence protein-
1161 protein interactions annotated in the STRING database (interaction score≥0.6). The final drug-target
1162 connectivity map that was used for COSTAR consisted of 127 PCY-tested drugs, 975 extended primary
1163 targets, 10,573 secondary targets, and 114,517 network edges. The 127 drugs were labeled either as
1164 PCY-hits (n=30, equally split across NADs and ONCDs) or PCY-negative drugs (n=97) based on the
1165 ranked mean PCY score across patients.

1166 A 20-fold cross-validated LASSO generalized linear model was trained in Matlab with the drug-target
1167 connectivity map as the predictor variable and PCY-hit status (hit vs. neg) as the binomially-distributed
1168 response variable to identify the optimal regularization coefficient (λ) across a geometric
1169 sequence of 60 possible values. Final model coefficients were fitted using the λ value
1170 corresponding to the minimum deviance in the cross-validation analysis shown in *Extended Data Figure*
1171 *6a*. COSTAR performance was first evaluated on the training dataset, represented as a confusion matrix
1172 in *Figure 3g*. Using this trained linear model, COSTAR was next utilized as an *in silico* drug screening
1173 tool to predict the PCY-hit probability (COSTAR score) based on the connectivity of 1,120,823
1174 compounds annotated in DTC (*Supplementary Table 6*). For interpretability, COSTAR subscores,
1175 defined as the individual connectivity to target genes multiplied by their respective coefficients (betas)
1176 in the linear model, can be investigated in *Extended Data Figure 6b,c*. COSTAR predictions from this *in*
1177 *silico* screen were further experimentally validated in glioblastoma patient samples on a set of new
1178 drugs predicted as either COSTAR-hits or COSTAR-negs (n=48 drugs total; n=23 COSTAR-hits; n=25
1179 COSTAR-negs).

1180 **Single-cell RNA-Seq and analysis of other published datasets**

1181 Cryopreserved single-cell suspensions of glioblastoma patient samples that were part of the
1182 prospective cohort were thawed in reduced serum media (DMEM containing 2% FBS) and used for
1183 single-cell RNA-Seq experiments. Viability markers SYTOX Blue (1 μ M, Thermo Fisher, #S11348) and
1184 DRAQ5 (1 μ M, Biolegend, #424101) were added to the cell suspension at least 15 minutes before
1185 sorting. FACS gates were set based on CD45 (Alexa Fluor[®] 594 anti-CD45, 1:20, Biolegend, #368520,
1186 clone 2D1), SYTOX Blue and DRAQ5 intensities to isolate live CD45+ and CD45- populations as shown
1187 in *Extended Data Figure 1b* using the BD FACSAria[™] Fusion Cell Sorter. Cells were sorted into DNA
1188 LoBind[®] Eppendorf tubes (VWR, #525-0130), then CD45- cells were mixed with CD45+ cells at 2:1 to
1189 10:1 ratios depending on cell availability to enrich for glioblastoma cells. For patient sample P024 that
1190 was used to measure the effect of Vortioxetine drug treatment, FAC-sorted cells were incubated for 3
1191 hours with or without 20 μ M Vortioxetine before proceeding to library preparation. Single-cell RNA-
1192 Seq library preparation was performed using the Chromium Next GEM Single Cell 3' v3.0 and v3.1 kits
1193 (10x Genomics) according to the manufacturer's protocol. Libraries were sequenced on the Novaseq
1194 6000 (Illumina). Read alignment to the GRCh38 human reference genome, generation of feature-
1195 barcode matrices, and aggregation of multiple samples were performed using the Cell Ranger analysis
1196 pipeline (10x genomics, versions 3.0.1 and 6.1.1). Four patient samples (P007, P011, P012, P013) were
1197 processed in November 2019 with the earlier version of 10x Genomics library prep kits and Cell Ranger
1198 analysis pipeline while the later sample (P024) was processed in September 2021. Quality control for
1199 this in-house dataset was performed by only analyzing high-quality cells with fewer than 10% of
1200 mitochondrial transcripts and genes that had at least a count of 2 in at least 3 cells.

1201 To analyze additional glioblastoma patient samples by single-cell RNA-Seq, we utilized two published
1202 datasets: (Neftel et al. 2019) and (Yu et al. 2020). For Neftel *et al.*, we removed cells with less than 2⁹
1203 detected genes and/or more than 15% of mitochondrial transcripts. For Yu *et al.* the data was already
1204 prefiltered, but patient samples (7-9, 14-15) that did not correspond to glioblastoma (grade IV
1205 astrocytomas) were not included. For both datasets only genes that had at a count of 2 in at least 2
1206 cells were included in the analysis.

1207 Neural patient specificity scores and patient specificity scores for each gene were defined as follows:
1208 using the in-house dataset, we identified putative cell types by unsupervised clustering using Monocle
1209 ⁸⁷ and annotated the clusters based on known marker genes as being either immune or neural cells.

1210 We then obtained a list of differentially expressed genes between immune and neural cells using
1211 DESingle⁸⁸, using a logFC cutoff of 0.5. This yielded a list of 11571 neural-specific and 1157 immune
1212 specific genes. Using these lists as cell-type specific gene sets, we calculated an immune- and a neural
1213 score for each cell using singscore, and classified every cell in the additional datasets as either neural
1214 or immune based on a linear combination of both scores. To assess how specifically a gene is expressed
1215 in neural cells, we defined a ‘neural specificity score’ as follows: [$neural\ specificity = fraction\ of\ neural\ cells\ expressing\ gene - fraction\ of\ immune\ cells\ expressing\ gene$] where we define expression of a gene
1216 in a cell as having any non-zero count. Thus, a positive score indicates that a gene is more often found
1217 in neural cells than in immune cells, and vice versa for negative scores. This score ranges from -1 (gene
1218 is expressed in all immune cells and no neural cells) to =1 (gene is expressed in all neural cells and no
1219 immune cells). Note that for low expressed genes, this score will be close to 0, reflecting the fact that
1220 we cannot make clear statements about cell type specificity for genes with expression values close to
1221 the detection limit of scRNA-Seq. To assess how much gene expression for a single gene varies across
1222 patients, we defined a ‘patient specificity score’ as follows: First, for every gene gi and every patient pj
1223 we calculated a cell type composition independent fraction of cells expressing gene gi as
1224 [$Fraction_expressing_ij = fraction_expressing_immune_ij + fraction_expressing_neural_ij$]. We then
1225 defined patient specificity as the median absolute deviation (MAD) of fraction_expressing across all
1226 patients, thus defining [$Patient_specificity_i = mad(Fraction_expressing_i,:)$].
1227

1228 DRUG-Seq

1229 High-throughput multiplexed RNA sequencing was performed with the Digital RNA with perturbation
1230 of Genes (DRUG-Seq) method as described in (Ye et al. 2018) with a few modifications. Modifications
1231 to the published method are the following: 1) extraction of RNA prior to cDNA reverse transcription
1232 with the Zymo Direct-zol-96 RNA isolation kit (Zymo, #R0256) 2) change of reverse transcription
1233 primers for compatibility with standard Illumina sequencing primers 3) cDNA clean-up prior to library
1234 amplification performed with the DNA Clean & Concentrator-5 kit (Zymo, #D4013) 3) tagmentation
1235 was performed with 2ng input and sequencing library generated using the Nextera XT library prep kit
1236 (Illumina, #FC-131-1024). In short, 1×10^4 LN-229 cells were plated in CellCarrier-96 Ultra Microplates
1237 (PerkinElmer, #6055302) and incubated overnight in reduced serum media at 37°C, 5% CO₂ prior to
1238 drug treatment. A total of 20 drugs (Supplementary Table 3) were profiled across two different time-
1239 points (6 hours and 22 hours; n=4 replicates per drug and time-point). These 20 drugs were selected
1240 to include PCY-hit NADs spanning diverse drug classes (n=11), PCY-hit ONCDs (n=7), PCY-negative NADs
1241 (n=2), and a DMSO control. Cells in drug-treated 96-wells were lysed with TRIzol™ Reagent
1242 (ThermoFisher, #15596018) and then subsequent cDNA and library prep was performed as described
1243 above. 100bp (80:20) paired-end reads were generated using Illumina’s NextSeq 2000 platform.

1244 Calcium assays on the FLIPR platform

1245 For calcium assays, 24 hours prior to the experiment, LN-229 cells were seeded at a density of 70,000
1246 cells/well on poly-D-Lysine-coated ViewPlate™-96 F TC 96-well black polystyrene clear bottom
1247 microplates (PerkinElmer, #6005182) in 100µl full medium. Calcium 6 dye stock solution was prepared
1248 by dissolving a vial from Calcium 6 assay kit (Molecular Devices, #5024048) in 10 ml sterile-filtered
1249 nominal Ca²⁺ free (NCF), modified Krebs buffer containing 117mM NaCl, 4.8mM KCl, 1mM MgCl₂, 5mM
1250 D-glucose, 10mM HEPES (pH 7.4) and 500µl aliquots were stored at -20°C. Before each experiment,
1251 the dye stock was freshly diluted 1:10 in NCF Krebs buffer and after removing the medium from the
1252 cells, 50µl of the diluted dye was applied per well. In order to allow the cells to absorb the dye into
1253 their cytosol, they were incubated at 37°C for 2 hours in the dark. The fluorescence Ca²⁺ measurements

1254 were carried out using FLIPR Tetra[®] (Molecular Devices) where cells were excited using a 470–495nm
1255 LED module and the emitted fluorescence signal was filtered with a 515–575nm emission filter
1256 according to the manufacturer’s guidelines.

1257 In the ER Ca²⁺ store release assay, the stable baselines were established for 50 seconds before 50µl of
1258 2µM (2X) Thapsigargin (Sigma-Aldrich, #T9033) or 40µM (2X) drug solutions freshly prepared in NCF
1259 Krebs buffer were robotically dispensed to the cells to determine whether the drugs impact the ER Ca²⁺
1260 stores. Next, the cells were incubated and fluorescence was monitored in the presence of Thapsigargin
1261 or drugs for another 5 min. In the extracellular Ca²⁺ uptake assay, after initial recording of the baseline,
1262 50µl of 4mM CaCl₂ (2X) prepared in NCF Krebs buffer was dispensed onto the cells to re-establish a
1263 physiological 2mM calcium concentration and the fluorescence was monitored for 5 min. Next, 60µM
1264 (3X) drug solutions freshly prepared in Krebs buffer containing 2mM CaCl₂ were robotically dispensed
1265 to the cells and the fluorescence was recorded for an additional 4 min. The raw data was extracted
1266 with the ScreenWorks software version 3.2.0.14. The values represent average fluorescence level of
1267 the Calcium 6 dye measured over arbitrary selected and fixed time frames.

1268 **Time-course RNA-Seq library preparation and sequencing**

1269 Low passage LN-229 cells (passage 5-6) were seeded at 2x10⁵ cells/well into in 6-well Nunc™ Cell-
1270 Culture Treated Multidishes (ThermoFisher, #140675) and incubated overnight in reduced serum
1271 media at 37°C, 5% CO₂ prior to drug treatment. The following day, Vortioxetine (Avachem Scientific,
1272 #3380) was manually added to each well at a final concentration of 20µM. At the start of the
1273 experiment, LN-229 cells that were not treated with Vortioxetine were collected as the 0 hour time-
1274 point. After 3, 6, 9, 12, and 24 hours following Vortioxetine treatment, drug-containing media was
1275 removed and cells were collected in TRIzol™ Reagent (ThermoFisher, #15596018). Total RNA was
1276 isolated using Direct-zol RNA MicroPrep Kit (Zymo Research, #R2062) according to the manufacturer’s
1277 protocol and RNA quality and quantity was determined with the Agilent 4200 TapeStation. Sample RIN
1278 scores ranged from 5.9-10 (mean: 9.33). RNA input was normalized to 300-400 ng and RNA libraries
1279 were prepared using the Illumina Truseq stranded mRNA library prep following manufacturer’s
1280 protocols. 100bp single-end reads were generated using Illumina’s Novaseq 6000 platform with an
1281 average sequencing depth of approximately 50 million reads per replicate. Reads were mapped and
1282 aligned to the reference human genome assembly (GRCh38.p13) using STAR/2.7.8a and counts were
1283 extracted using featureCounts. Subsequent read normalization (variance stabilizing transformation,
1284 vsd-normalized counts) and RNA-Seq analysis including differential expression (DE) analysis was
1285 performed with the R package ‘DESeq2’⁸⁹.

1286 **Time-course Proteomics**

1287 Cell preparation and Vortioxetine treatment was performed as in ‘Time-course RNA-Seq library
1288 preparation’ except cell numbers were scaled to be seeded in T-150 culture flasks and 3 time-points
1289 were measured (0, 3, 9 hours). Peptides for mass spectrometry measurements were prepared using
1290 the PreOmics iST kit (PreOmics) on the PreON (HSE AG). The robot was programmed to process 8
1291 samples in parallel. During the first step of processing, cell pellets were resuspended in 50ul of lysis
1292 buffer and denatured for 10 minutes at 70°C. According to the manufacturer’s protocol, this step was
1293 followed by 3 hours of digestion with trypsin and Lys-C. Peptides were dried in a speed-vac (Thermo
1294 Fisher Scientific) for 1 hour before being resuspended in LC- Load buffer at a concentration of 1 ug/ul
1295 with iRT peptides (Biognosys).

1296 Samples were analyzed on an Orbitrap Lumos mass spectrometer (Thermo Fisher Scientific) equipped
1297 with an Easy-nLC 1200 (Thermo Fisher Scientific). Peptides were separated on an in-house packed 30
1298 cm RP-HPLC column (Michrom BioResources, 75 μm i.d. x 30 cm; Magic C18 AQ 1.9 μm , 200 \AA). Mobile
1299 phase A consisted of HPLC-grade water with 0.1% formic acid, and mobile phase B consisted of HPLC-
1300 grade ACN (80%) with HPLC-grade water and 0.1% (v/v) formic acid. Peptides were eluted at a flow
1301 rate of 250 nl/min using a non-linear gradient from 4% to 47% mobile phase B in 228 min. For data-
1302 independent acquisition (DIA), DIA-overlapping windows were used and a mass range of m/z 396-1005
1303 was covered. The DIA isolation window size was set to 8 and 4 m/z, respectively, and a total of 75 or
1304 152 DIA scan windows were recorded at a resolution of 30,000 with an AGC target value set to 1200%.
1305 HCD fragmentation was set to 30% normalized collision. Full MS were recorded at a resolution of
1306 60,000 with an AGC target set to standard and the maximum injection time set to auto. DIA data were
1307 analyzed using Spectronaut v14 (Biognosys). MS1 values were used for the quantification process,
1308 peptide quantity was set to mean. Data were filtered using Qvalue sparse with a precursor and a
1309 protein Qvalue cut-off of 0.01 FDR. Interference correction and local cross-run normalization was
1310 performed. For PRM measurements, peptides were separated by reversed-phase chromatography on
1311 a 50 cm ES803 C18 column (Thermo Fisher Scientific) that was connected to a Easy-nLC 1200 (Thermo
1312 Fisher Scientific). Peptides were eluted at a constant flow rate of 200 nl/min with a 117 min non-linear
1313 gradient from 4–52% buffer B (80% ACN, 0.1% FA) and 25-50%B. Mass spectra were acquired in PRM
1314 mode on an Q Exactive HF-X Hybrid Quadrupole-Orbitrap MS system (Thermo Fisher Scientific). The
1315 MS1 mass range was 340–1,400 m/z at a resolution of 120,000. Spectra were acquired at 60,000
1316 resolution (automatic gain control target value 2.0×10^5); Normalized HCD collision energy was set to
1317 28%, maximum injection time to 118 ms. Monitored peptides were analyzed in Skyline v20 and results
1318 were uploaded to PanoramaWeb.

1319 **Incucyte live cell imaging**

1320 To measure cell proliferation in real-time, 2.5×10^3 LN-229 cells/well were plated in CellCarrier-96
1321 Ultra Microplates (PerkinElmer, #6055302) 24 hours prior to the experiment, and transfected with
1322 BTG1, BTG2, and FLUC (-) MISSION[®] esiRNAs (Sigma-Aldrich, Euphoria Biotech, 40ng/well) using
1323 Lipofectamine RNAiMAX (Invitrogen, #13778075). Further details regarding siRNAs can be found in
1324 *Supplementary Table 5* and *Methods* related to ‘siRNA knockdown and quantitative real-time
1325 PCR’. Real-time confluence of cell cultures (n=4 replicate wells/condition) was monitored by imaging
1326 every 2 hours for 7 days at 10x magnification with the ‘phase’ channel using the Incucyte live-cell
1327 analysis system S3 (Sartorius). Automatic image segmentation and analysis of the phase contrast
1328 images was performed by the Incucyte base analysis software (version 2020B).

1329 **Clonogenic survival assay**

1330 Adherent cells (LN-229: 50 cells; LN-308: 300 cells) were seeded in six replicates in 100 μL per well in
1331 96-well plates and incubated overnight. On the following day, medium was replaced by fresh medium
1332 containing indicated final concentrations of Vortioxetine or DMSO. Glioblastoma-initiating cells (500
1333 cells) were seeded in 75 μL medium and incubated overnight. Treatment was initiated by addition of
1334 75 μL medium containing 2x concentrated Vortioxetine or DMSO to reach indicated final
1335 concentrations. DMSO concentration was kept at 0.5% for all treatments and controls. Following
1336 treatment addition, cells were cultured for 11 (LN-229) to 13 days (other cell lines) and clonogenic
1337 survival was estimated from a resazurin-based assay⁹⁰ using a Tecan M200 PRO plate reader ($\lambda_{\text{Ex}} =$
1338 $560 \text{ nm} / \lambda_{\text{Em}} = 590 \text{ nm}$).

1339 **Collagen-based spheroid invasion assay**

1340 Spheroid invasion assay was performed as described in (Kumar et al. 2015). Briefly, 2000 cells were
1341 seeded in six replicates into cell-repellent 96 U-bottom well plates (Greiner, #650979) and incubated
1342 for 48 hours to allow spheroid formation. Subsequently, 70 μ L medium were removed, spheroids were
1343 overlaid with 70 μ L 2.5% Collagen IV (Advanced Biomatrix, #5005-B) in 1xDMEM containing sodium
1344 bicarbonate (Sigma-Aldrich #S8761) and collagen was solidified in the incubator for 2 hours. Collagen-
1345 embedded spheroids were then overlaid with 100 μ L chemoattractant (NIH-3T3-conditioned medium)
1346 containing 2x concentrated Vortioxetine/DMSO (0.5% final DMSO concentration across conditions)
1347 and incubated for 36 hours. Spheroids were stained with Hoechst and images were acquired on a
1348 MuviCyte imaging system (Perkin Elmer, #HH40000000) using a 4x objective. Images were contrast-
1349 enhanced and converted to binary using ImageJ/Fiji and quantified with the automated Spheroid
1350 Dissemination/Invasion counter software (aSDIcs), which quantifies the migration distance from the
1351 center of the spheroid for each detected cell nucleus⁹¹.

1352 ***In vivo* drug testing**

1353 All animal experiments were done under the guidelines of the Swiss federal law on animal protection
1354 and were approved by the cantonal veterinary office (ZH98/2018). CD1 female nu/nu mice (Janvier, Le
1355 Genest-Saint-Isle, France) of 6 to 12 weeks of age were used in all experiments and 100'000 LN-229-
1356 derived- or 150'000 ZH-161-derived cells were implanted⁹². Tumor-bearing mice were treated from
1357 day 5 – day 21 after tumor implantation with intraperitoneally (*i.p.*) administered Vortioxetine daily
1358 10mg/kg, Paliperidone daily 5mg/kg, Apomorphine daily 5mg/kg, Aprepitant daily 20mg/kg,
1359 Brexpiprazole daily 1mg/kg, Chlorpromazine three time per week 10mg/kg, Temozolomide 50mg/kg
1360 for five consecutive days, CCNU 20mg/kg at day 7 and 14 after tumor implantation, or daily DMSO
1361 control. Magnetic resonance imaging (MRI) was performed with a 4.7 T imager (Bruker Biospin,
1362 Ettlingen, Germany) when the first mouse became symptomatic. Coronal T2-weighted images were
1363 acquired using Paravision 6.0 (Bruker BioSpin).

1364

References

- 1365 1. Ostrom, Q. T., Cioffi, G., Waite, K., Kruchko, C. & Barnholtz-Sloan, J. S. CBTRUS Statistical Report:
1366 Primary Brain and Other Central Nervous System Tumors Diagnosed in the United States in
1367 2014-2018. *Neuro. Oncol.* **23**, iii1–iii105 (2021).
- 1368 2. Osswald, M. *et al.* Brain tumour cells interconnect to a functional and resistant network. *Nature*
1369 **528**, 93–98 (2015).
- 1370 3. Venkatesh, H. S. *et al.* Neuronal Activity Promotes Glioma Growth through Neuroligin-3
1371 Secretion. *Cell* **161**, 803–816 (2015).
- 1372 4. Weil, S. *et al.* Tumor microtubules convey resistance to surgical lesions and chemotherapy in
1373 gliomas. *Neuro. Oncol.* **19**, 1316–1326 (2017).
- 1374 5. Venkataramani, V. *et al.* Glutamatergic synaptic input to glioma cells drives brain tumour
1375 progression. *Nature* **573**, 532–538 (2019).
- 1376 6. Venkatesh, H. S. *et al.* Electrical and synaptic integration of glioma into neural circuits. *Nature*
1377 **573**, 539–545 (2019).
- 1378 7. Alcantara Llaguno, S. *et al.* Cell-of-origin susceptibility to glioblastoma formation declines with
1379 neural lineage restriction. *Nat. Neurosci.* **22**, 545–555 (2019).
- 1380 8. Venkataramani, V. *et al.* Glioblastoma hijacks neuronal mechanisms for brain invasion. *Cell* **185**,
1381 2899–2917.e31 (2022).
- 1382 9. Cancer Genome Atlas Research Network. Comprehensive genomic characterization defines
1383 human glioblastoma genes and core pathways. *Nature* **455**, 1061–1068 (2008).
- 1384 10. Brennan, C. W. *et al.* The somatic genomic landscape of glioblastoma. *Cell* **155**, 462–477 (2013).
- 1385 11. Suvà, M. L. *et al.* Reconstructing and reprogramming the tumor-propagating potential of
1386 glioblastoma stem-like cells. *Cell* **157**, 580–594 (2014).
- 1387 12. Neftel, C. *et al.* An Integrative Model of Cellular States, Plasticity, and Genetics for Glioblastoma.
1388 *Cell* **178**, 835–849.e21 (2019).
- 1389 13. Varn, F. S. *et al.* Glioma progression is shaped by genetic evolution and microenvironment
1390 interactions. *Cell* **185**, 2184–2199.e16 (2022).
- 1391 14. Stupp, R. *et al.* Radiotherapy plus concomitant and adjuvant temozolomide for glioblastoma. *N.*
1392 *Engl. J. Med.* **352**, 987–996 (2005).
- 1393 15. Hegi, M. E. *et al.* MGMT gene silencing and benefit from temozolomide in glioblastoma. *N. Engl.*
1394 *J. Med.* **352**, 997–1003 (2005).
- 1395 16. Weller, M. *et al.* EANO guidelines on the diagnosis and treatment of diffuse gliomas of
1396 adulthood. *Nat. Rev. Clin. Oncol.* **18**, 170–186 (2021).
- 1397 17. Singh, S. K. *et al.* Identification of human brain tumour initiating cells. *Nature* **432**, 396–401
1398 (2004).
- 1399 18. Bao, S. *et al.* Glioma stem cells promote radioresistance by preferential activation of the DNA
1400 damage response. *Nature* **444**, 756–760 (2006).
- 1401 19. Chen, J. *et al.* A restricted cell population propagates glioblastoma growth after chemotherapy.
1402 *Nature* **488**, 522–526 (2012).
- 1403 20. Harder, B. G. *et al.* Developments in blood-brain barrier penetrance and drug repurposing for
1404 improved treatment of glioblastoma. *Front. Oncol.* **8**, 462 (2018).
- 1405 21. Le Rhun, E. *et al.* Molecular targeted therapy of glioblastoma. *Cancer Treat. Rev.* **80**, 101896
1406 (2019).
- 1407 22. Gómez-Oliva, R. *et al.* Evolution of Experimental Models in the Study of Glioblastoma: Toward

- 1408 Finding Efficient Treatments. *Front. Oncol.* **10**, 614295 (2020).
- 1409 23. Patel, A. P. *et al.* Single-cell RNA-seq highlights intratumoral heterogeneity in primary
1410 glioblastoma. *Science* **344**, 1396–1401 (2014).
- 1411 24. John Lin, C.-C. *et al.* Identification of diverse astrocyte populations and their malignant analogs.
1412 *Nat. Neurosci.* **20**, 396–405 (2017).
- 1413 25. Lan, X. *et al.* Fate mapping of human glioblastoma reveals an invariant stem cell hierarchy.
1414 *Nature* **549**, 227–232 (2017).
- 1415 26. Lee, J. H. *et al.* Human glioblastoma arises from subventricular zone cells with low-level driver
1416 mutations. *Nature* **560**, 243–247 (2018).
- 1417 27. Couturier, C. P. *et al.* Single-cell RNA-seq reveals that glioblastoma recapitulates a normal
1418 neurodevelopmental hierarchy. *Nat. Commun.* **11**, 3406 (2020).
- 1419 28. Yu, K. *et al.* Surveying brain tumor heterogeneity by single-cell RNA-sequencing of multi-sector
1420 biopsies. *Natl Sci Rev* **7**, 1306–1318 (2020).
- 1421 29. Dolma, S. *et al.* Inhibition of Dopamine Receptor D4 Impedes Autophagic Flux, Proliferation, and
1422 Survival of Glioblastoma Stem Cells. *Cancer Cell* **29**, 859–873 (2016).
- 1423 30. Caragher, S. P. *et al.* Activation of Dopamine Receptor 2 Prompts Transcriptomic and Metabolic
1424 Plasticity in Glioblastoma. *J. Neurosci.* **39**, 1982–1993 (2019).
- 1425 31. Bi, J. *et al.* Targeting glioblastoma signaling and metabolism with a re-purposed brain-penetrant
1426 drug. *Cell Rep.* **37**, 109957 (2021).
- 1427 32. Snijder, B. *et al.* Image-based ex-vivo drug screening for patients with aggressive haematological
1428 malignancies: interim results from a single-arm, open-label, pilot study. *Lancet Haematol* **4**,
1429 e595–e606 (2017).
- 1430 33. Kornauth, C. *et al.* Functional Precision Medicine Provides Clinical Benefit in Advanced
1431 Aggressive Hematologic Cancers and Identifies Exceptional Responders. *Cancer Discov.* **12**, 372–
1432 387 (2022).
- 1433 34. Heinemann, T. *et al.* Deep morphology learning enhances ex vivo drug profiling-based precision
1434 medicine. *Blood Cancer Discov* (2022) doi:10.1158/2643-3230.BCD-21-0219.
- 1435 35. Malta, T. M. *et al.* Machine Learning Identifies Stemness Features Associated with Oncogenic
1436 Dedifferentiation. *Cell* **173**, 338–354.e15 (2018).
- 1437 36. Dahlstrand, J., Collins, V. P. & Lendahl, U. Expression of the Class VI Intermediate Filament
1438 Nestin in Human Central Nervous System Tumors¹. *Cancer Res.* **52**, 5334–5341 (1992).
- 1439 37. Yuan, X. *et al.* Isolation of cancer stem cells from adult glioblastoma multiforme. *Oncogene* **23**,
1440 9392–9400 (2004).
- 1441 38. Zhang, M. *et al.* Nestin and CD133: valuable stem cell-specific markers for determining clinical
1442 outcome of glioma patients. *J. Exp. Clin. Cancer Res.* **27**, 85 (2008).
- 1443 39. Vladimer, G. I. *et al.* Global survey of the immunomodulatory potential of common drugs. *Nat.*
1444 *Chem. Biol.* **13**, 681–690 (2017).
- 1445 40. Conde, J. *et al.* Allosteric Antagonist Modulation of TRPV2 by Piperlongumine Impairs
1446 Glioblastoma Progression. *ACS Cent Sci* **7**, 868–881 (2021).
- 1447 41. Severin, Y. *et al.* Multiplexed high-throughput immune cell imaging reveals molecular health-
1448 associated phenotypes. *bioRxiv* 2021.12.03.471105 (2021) doi:10.1101/2021.12.03.471105.
- 1449 42. Shilts, J. *et al.* A physical wiring diagram for the human immune system. *Nature* (2022)
1450 doi:10.1038/s41586-022-05028-x.
- 1451 43. Kirshner, J. R. *et al.* Elesclomol induces cancer cell apoptosis through oxidative stress. *Mol.*
1452 *Cancer Ther.* **7**, 2319–2327 (2008).
- 1453 44. Guthrie, L. M. *et al.* Elesclomol alleviates Menkes pathology and mortality by escorting Cu to

- 1454 cuproenzymes in mice. *Science* **368**, 620–625 (2020).
- 1455 45. Xie, Q. *et al.* Mitochondrial control by DRP1 in brain tumor initiating cells. *Nat. Neurosci.* **18**,
1456 501–510 (2015).
- 1457 46. Bonnay, F. *et al.* Oxidative Metabolism Drives Immortalization of Neural Stem Cells during
1458 Tumorigenesis. *Cell* **182**, 1490–1507.e19 (2020).
- 1459 47. Garofano, L. *et al.* Pathway-based classification of glioblastoma uncovers a mitochondrial
1460 subtype with therapeutic vulnerabilities. *Nat Cancer* **2**, 141–156 (2021).
- 1461 48. Lombardi, G. *et al.* Regorafenib compared with lomustine in patients with relapsed glioblastoma
1462 (REGOMA): a multicentre, open-label, randomised, controlled, phase 2 trial. *Lancet Oncol.* **20**,
1463 110–119 (2019).
- 1464 49. Wick, W. *et al.* Phase II Study of Radiotherapy and Temozolomide versus Radiochemotherapy
1465 with Temozolomide in Patients with Newly Diagnosed Glioblastoma without MGMT Promoter
1466 Hypermethylation (EORTC 26082). *Clin. Cancer Res.* **22**, 4797–4806 (2016).
- 1467 50. Chinnaiyan, P. *et al.* A randomized phase II study of everolimus in combination with
1468 chemoradiation in newly diagnosed glioblastoma: results of NRG Oncology RTOG 0913. *Neuro.*
1469 *Oncol.* **20**, 666–673 (2018).
- 1470 51. Babak, S. & Mason, W. P. mTOR inhibition in glioblastoma: requiem for a dream? *Neuro-*
1471 *oncology* vol. 20 584–585 (2018).
- 1472 52. Tang, J. *et al.* Drug Target Commons: A Community Effort to Build a Consensus Knowledge Base
1473 for Drug-Target Interactions. *Cell Chem Biol* **25**, 224–229.e2 (2018).
- 1474 53. Sheng, M. & Greenberg, M. E. The regulation and function of c-fos and other immediate early
1475 genes in the nervous system. *Neuron* **4**, 477–485 (1990).
- 1476 54. Yap, E.-L. & Greenberg, M. E. Activity-Regulated Transcription: Bridging the Gap between Neural
1477 Activity and Behavior. *Neuron* **100**, 330–348 (2018).
- 1478 55. Ye, C. *et al.* DRUG-seq for miniaturized high-throughput transcriptome profiling in drug
1479 discovery. *Nat. Commun.* **9**, 4307 (2018).
- 1480 56. Li, J. *et al.* DRUG-seq Provides Unbiased Biological Activity Readouts for Neuroscience Drug
1481 Discovery. *ACS Chem. Biol.* **17**, 1401–1414 (2022).
- 1482 57. Rouault, J. P. *et al.* Identification of BTG2, an antiproliferative p53-dependent component of the
1483 DNA damage cellular response pathway. *Nat. Genet.* **14**, 482–486 (1996).
- 1484 58. Yuniati, L., Scheijen, B., van der Meer, L. T. & van Leeuwen, F. N. Tumor suppressors BTG1 and
1485 BTG2: Beyond growth control. *J. Cell. Physiol.* **234**, 5379–5389 (2019).
- 1486 59. Eferl, R. & Wagner, E. F. AP-1: a double-edged sword in tumorigenesis. *Nat. Rev. Cancer* **3**, 859–
1487 868 (2003).
- 1488 60. Karin, M., Liu, Z. g. & Zandi, E. AP-1 function and regulation. *Curr. Opin. Cell Biol.* **9**, 240–246
1489 (1997).
- 1490 61. Sanyal, S., Sandstrom, D. J., Hoeffler, C. A. & Ramaswami, M. AP-1 functions upstream of CREB to
1491 control synaptic plasticity in Drosophila. *Nature* **416**, 870–874 (2002).
- 1492 62. Carlsson, P. & Mahlapuu, M. Forkhead Transcription Factors: Key Players in Development and
1493 Metabolism. *Dev. Biol.* **250**, 1–23 (2002).
- 1494 63. Ho, K. K., Myatt, S. S. & Lam, E. W.-F. Many forks in the path: cycling with FoxO. *Oncogene* **27**,
1495 2300–2311 (2008).
- 1496 64. Benayoun, B. A., Caburet, S. & Veitia, R. A. Forkhead transcription factors: key players in health
1497 and disease. *Trends Genet.* **27**, 224–232 (2011).
- 1498 65. Sheng, M., Thompson, M. A. & Greenberg, M. E. CREB: a Ca(2+)-regulated transcription factor
1499 phosphorylated by calmodulin-dependent kinases. *Science* **252**, 1427–1430 (1991).

- 1500 66. Whitmarsh, A. J. & Davis, R. J. Transcription factor AP-1 regulation by mitogen-activated protein
1501 kinase signal transduction pathways. *J. Mol. Med.* **74**, 589–607 (1996).
- 1502 67. Park, C. Y. *et al.* Tissue-aware data integration approach for the inference of pathway
1503 interactions in metazoan organisms. *Bioinformatics* **31**, 1093–1101 (2015).
- 1504 68. Grünblatt, E., Mandel, S., Berkuzki, T. & Youdim, M. B. Apomorphine protects against MPTP-
1505 induced neurotoxicity in mice. *Mov. Disord.* **14**, 612–618 (1999).
- 1506 69. Guilloux, J.-P. *et al.* Antidepressant and anxiolytic potential of the multimodal antidepressant
1507 vortioxetine (Lu AA21004) assessed by behavioural and neurogenesis outcomes in mice.
1508 *Neuropharmacology* **73**, 147–159 (2013).
- 1509 70. Maeda, K. *et al.* Brexpiprazole I: in vitro and in vivo characterization of a novel serotonin-
1510 dopamine activity modulator. *J. Pharmacol. Exp. Ther.* **350**, 589–604 (2014).
- 1511 71. Berger, M. *et al.* Hepatoblastoma cells express truncated neurokinin-1 receptor and can be
1512 growth inhibited by aprepitant in vitro and in vivo. *J. Hepatol.* **60**, 985–994 (2014).
- 1513 72. Oliva, C. R., Zhang, W., Langford, C., Suto, M. J. & Griguer, C. E. Repositioning chlorpromazine for
1514 treating chemoresistant glioma through the inhibition of cytochrome c oxidase bearing the
1515 COX4-1 regulatory subunit. *Oncotarget* **8**, 37568–37583 (2017).
- 1516 73. Torrisi, S. A. *et al.* Fluoxetine and Vortioxetine Reverse Depressive-Like Phenotype and Memory
1517 Deficits Induced by A β 1-42 Oligomers in Mice: A Key Role of Transforming Growth Factor- β 1.
1518 *Front. Pharmacol.* **10**, 693 (2019).
- 1519 74. Lee, J.-K., Nam, D.-H. & Lee, J. Repurposing antipsychotics as glioblastoma therapeutics:
1520 Potentials and challenges. *Oncol. Lett.* **11**, 1281–1286 (2016).
- 1521 75. Tan, S. K. *et al.* Drug Repositioning in Glioblastoma: A Pathway Perspective. *Front. Pharmacol.* **9**,
1522 218 (2018).
- 1523 76. Caragher, S. P., Hall, R. R., Ahsan, R. & Ahmed, A. U. Monoamines in glioblastoma: complex
1524 biology with therapeutic potential. *Neuro. Oncol.* **20**, 1014–1025 (2018).
- 1525 77. Lee, J.-K. *et al.* Spatiotemporal genomic architecture informs precision oncology in glioblastoma.
1526 *Nat. Genet.* **49**, 594–599 (2017).
- 1527 78. Lee, J.-K. *et al.* Pharmacogenomic landscape of patient-derived tumor cells informs precision
1528 oncology therapy. *Nat. Genet.* **50**, 1399–1411 (2018).
- 1529 79. MacLeod, G. *et al.* Genome-Wide CRISPR-Cas9 Screens Expose Genetic Vulnerabilities and
1530 Mechanisms of Temozolomide Sensitivity in Glioblastoma Stem Cells. *Cell Rep.* **27**, 971–986.e9
1531 (2019).
- 1532 80. Jacob, F. *et al.* A Patient-Derived Glioblastoma Organoid Model and Biobank Recapitulates Inter-
1533 and Intra-tumoral Heterogeneity. *Cell* **180**, 188–204.e22 (2020).
- 1534 81. Stockslager, M. A. *et al.* Functional drug susceptibility testing using single-cell mass predicts
1535 treatment outcome in patient-derived cancer neurosphere models. *Cell Rep.* **37**, 109788 (2021).
- 1536 82. Shekarian, T. *et al.* Immunotherapy of glioblastoma explants induces interferon- γ responses and
1537 spatial immune cell rearrangements in tumor center, but not periphery. *Sci Adv* **8**, eabn9440
1538 (2022).
- 1539 83. Szklarczyk, D. *et al.* STRING v11: protein-protein association networks with increased coverage,
1540 supporting functional discovery in genome-wide experimental datasets. *Nucleic Acids Res.* **47**,
1541 D607–D613 (2019).
- 1542 84. Schaefer, C. F. *et al.* PID: the Pathway Interaction Database. *Nucleic Acids Res.* **37**, D674–9
1543 (2009).
- 1544 85. Krizhevsky, A., Sutskever, I. & Hinton, G. E. ImageNet classification with deep convolutional
1545 neural networks. in *Proceedings of the 25th International Conference on Neural Information*

- 1546 *Processing Systems - Volume 1* 1097–1105 (Curran Associates Inc., 2012).
- 1547 86. Landrum, M. J. *et al.* ClinVar: improving access to variant interpretations and supporting
1548 evidence. *Nucleic Acids Res.* **46**, D1062–D1067 (2018).
- 1549 87. Trapnell, C. *et al.* The dynamics and regulators of cell fate decisions are revealed by
1550 pseudotemporal ordering of single cells. *Nat. Biotechnol.* **32**, 381–386 (2014).
- 1551 88. Miao, Z., Deng, K., Wang, X. & Zhang, X. DEsingle for detecting three types of differential
1552 expression in single-cell RNA-seq data. *Bioinformatics* **34**, 3223–3224 (2018).
- 1553 89. Love, M. I., Huber, W. & Anders, S. Moderated estimation of fold change and dispersion for
1554 RNA-seq data with DESeq2. *Genome Biol.* **15**, 550 (2014).
- 1555 90. Riss, T. L. *et al.* Cell Viability Assays. in *Assay Guidance Manual* (eds. Markossian, S. *et al.*) (Eli
1556 Lilly & Company and the National Center for Advancing Translational Sciences, 2013).
- 1557 91. Kumar, K. S. *et al.* Computer-assisted quantification of motile and invasive capabilities of cancer
1558 cells. *Sci. Rep.* **5**, 15338 (2015).
- 1559 92. Weiss, T. *et al.* NKG2D-Dependent Antitumor Effects of Chemotherapy and Radiotherapy against
1560 Glioblastoma. *Clin. Cancer Res.* **24**, 882–895 (2018).